國 立 交 通 大 學

光電工程研究所

博 士 論 文

非極性氮化鎵光電元件之磊晶成長

Epitaxial growth of nonpolar GaN based optoelectronic devices

研 究 生: 柯宗憲　　Student: Tsung-Shine Ko

指導教授: 郭浩中 教授　　Advisor: Dr. Hao-Chung Kuo
盧廷昌 教授　　Dr. Tien-Chang Lu

中 華 民 國 九 十 八 年 六 月

非極性氮化鎵光電元件之磊晶成長
Epitaxial growth of nonpolar GaN based optoelectronic devices

研 究 生：柯宗憲　　　　Student：Tsung-Shine Ko

指導教授：郭浩中教授　　Advisor：Dr. Hao-Chung Kuo

　　　　　盧廷昌教授　　　　　　Dr. Tien-Chang Lu

國 立 交 通 大 學 電機資訊學院

光電工程研究所

博 士 論 文

A dissertation

Submitted to Institute of Electro-Optical Engineering

College of Electrical Engineering and Computer Science

National Chiao Tung University

in partial Fulfillment of the Requirements

for the Degree of

Doctor of Philosophy

in

Department of Photonics & Electro-Optical Engineering

June 2009

Hsinchu, Taiwan, Republic of China

中華民國九十八年六月

非極性氮化鎵光電元件之磊晶成長

研究生：柯宗憲　　　　　　　　　　指導教授：郭浩中教授

盧廷昌教授

國立交通大學光電工程研究所

摘要

本論文旨在探討以有機金屬氣相沈積系統來成長非極性a面氮化鎵為主之光電材料與元件，包含了優化成長、減少材料缺陷、主動層氮化鎵銦量子井結構設計，最後完成a平面氮化鎵發光二極體製作與元件特性分析。

在磊晶之優化成長方面，我們利用有機金屬氣相沉積系統於高溫低壓下的成長環境下獲得高品質非極性a平面氮化鎵薄膜，改變成核層氮化鋁厚度與成長氮化鎵時的五三比，亦會影響非極性氮化鎵薄膜之品質。對於非極性氮化鎵之成長機制，我們利用Wulff圖形的概念以及選區成長的方法來分析非極性氮化鎵成長於r面藍寶石基板上的成長行為，此方法可以解釋非極性表面條紋以及坑洞的成因，並可進而預測成長，提供非極性氮化鎵成長之準則。

由於非極性 a 面氮化鎵成長不易，並具有很高的缺陷密度，因此在本論文中我們提出溝槽式磊晶側向成長以及氮化鎵銦/氮化鎵超晶格層的運用，來改善材料品質，由穿遂電子顯微鏡顯的結果，溝槽式磊晶側向成長可使 a 平面氮化鎵薄膜於氮極性方向上之晶格品質有明顯的提升，差排密度由原先的 1×10^{10} cm^{-2} 減少至 3×10^{7} cm^{-2}，而在氮化鎵銦/氮化鎵超晶格層的部份，差排密度可有效地從 3×10^{10} cm^{-2} 降低到 9×10^{9} cm^{-2}。此部份實驗確認達成晶格品質提升之目的與商業化的可行性。

為優化後續的非極性藍光雷射二極體的元件結構，我們改變非極性氮化鎵銦量子井的厚度並分析其光學特性。時間解析光致激發光譜結果指出當厚度逐漸變厚時，量子井產生的激子生命期逐漸增加。而在變溫的光致激發光譜中，我們發現在量子井厚度較薄的樣品具有較大的侷域深度可以有效地補獲激子，而較厚的樣品由於受到成長

溫度較長時間下的影響使得其侷域紊亂程度變得更為嚴重導致發光效率明顯下降。

在製作發光二極體方面，我們運用溝槽式磊晶側向成長之 a 面氮化鎵作為基板，成功地在上面成長了發光二極體結構，發現該結構由於具有兩種不同缺陷密度之區域，因此在改變電流下，發光波長會因為電流流經不同區域而有所不同，在注入電流為 140 mA 時功率為 0.2 mW；另外，在氮化銦鎵與氮化鎵組成的超晶格層部份，電致激發光譜的結果證實此樣品在強度上亦有 3.42 倍的增強，此元件並具有 56.3%的偏振率。

因此，於本論文中我們已完成了非極性氮化鎵材料的成長以及元件製作相關的研究，成果包含了成長條件優化、成長行為以及量子井結構與光學分析，另外，我們亦提出數種可改善材料品質的方法，將在本論文中逐一討論並證明其可行性。我們冀望這一系列的實驗對未來在非極性氮化鎵之光電元件發展而言，提供有用的資訊與助益。

Epitaxial growth of nonpolar GaN based optoelectronic devices

Student : Tsung-Shine Ko Advisor : Dr. Hao-Chung Kuo

Dr. Tien-Chang Lu

Department of Photonics & Institute of Electro-Optical Engineering

National Chiao Tung University

Abstract

In this dissertation, the epitaxial growth of nonpolar a-plane GaN based optoelectronic materials grown using metal organic chemical vapor deposition (MOCVD) have been investigated. Main works include optimum growth, InGaN multiple quantum wells (MQWs) design, reduction of defects and the fabrication of a-plane GaN based optoelectronic devices and analysis of device characteristics.

For optimum growth of a-plane GaN, we confirmed variation of thickness of AlN nucleation layer and V/III ratio of a-plane GaN growth influence crystal quality of a-plane GaN thin film. We also tried to figure out the mechanism of a-plane GaN by using Wulff plot and selective area growth to analyze the growth behavior of a-plane GaN grown on r-plane sapphire, which could be useful to explain the reasons account for stripes and pits exist on a-plane GaN surface and give us a guidance to predict growth of a-plane GaN.

In this dissertation, we used trench epitaxial lateral over growth (TELOG) and InGaN/GaN supperlattices (SLs) to improve crystal quality of a-plane GaN. The threading dislocation (TD) density can be reduced largely from 1×10^{10} cm^{-2} to 3×10^{7} cm^{-2} for the N-face GaN wing. As for SLs part, The TD density in the sample with SLs was reduced from 3×10^{10} cm^{-2} down to ~9×10^{9} cm^{-2}.

For active layer structural design, *a*-plane InGaN/GaN MQWs of different width ranging from 3 nm to 12 nm have been grown. The peak emission intensity of the photoluminescence (PL) reveals a decreasing trend as the well width increases from 3 nm to 12 nm. Low temperature (9 K) time-resolved PL (TRPL) study shows that the sample with 3 nm-thick wells has the best optical property with a fastest exciton decay time of 0.57 ns. More effective capturing of excitons due to larger localization energy E_{loc} and shorter radiative lifetime of localized excitons are observed in thinner well width samples were observed in the temperature dependent PL and TRPL.

In development of nonpolar light-emitting diodes (LEDs), we successfully fabricated a-plane LEDs structure by using TELOG GaN substrate. Due to there are two areas with different defect density in this kind sample, the emission wavelength will be changed when we increased injection current. The power was 0.2 mW at 140 mA injection current. On the other hand, we also fabricated nonpolar LEDs by using InGaN/GaN SLs layer. Electroluminescence intensity of the sample with InGaN/GaN SLs was enhanced by a factor of 3.42 times to that of the conventional sample without InGaN/GaN SLs.

In this dissertation, we have achieved the studies on the growth of a-plane GaN and the fabrication of devices. Whole achievements include optimum growth, MQWs structural design, crystal improvement of material and fabrication of a-plane LEDs. We hope this series of experiments to provide a useful information and support for development of nonpolar optoelectronic devices in future.

Acknowledge

完成這本博士論文的工作，並非我一人所能獨立完成，回首過去五年來的博士班生涯，除了自己的學習與充實，我更要感謝一路陪我走來的師長、朋友們，畢竟沒有這些人的扶持，我不可能完成這本論文、不可能得到這個學位、亦不可能蛻變為現在具觀察力、創新力、以及獨立思考能力的我。

首先我必須感謝我的指導老師們：王興宗教授、郭浩中教授以及盧廷昌教授，在王老師對學術知識追求的渴望、郭老師對研究結果的務實、以及盧老師對實驗過程的嚴謹風格帶領之下，著實讓我在博士班前四年，立下良好的學習基礎，更能展現個人的研究特色。另外，我亦十分感謝美國耶魯大學韓仲教授，千里馬的這一年時間，在他優秀學者風範的耳濡目染與薰陶之下，讓我的研究能力得到另一個提升，並敞開我對學術的視野。

我非常感謝德忠在磊晶知識上無私地傳授與經驗上的分享，讓我得以迅速地在這領域進入狀況，說真的，我欠你好幾頓的！家璞你不止在材料分析上的實驗大力幫忙外，在英文上更是一起互相砥礪、學習的好伙伴，我會努力幫你找對象的。也感謝潤琪在量測上的全力輔助與建設性的討論，雖然妳已經死會了，但我仍然積極地幫妳物色好伴侶。家銘亦是幫忙執行任務的好伙伴，希望你在台大的日子，可以過得充實又愉快。立夫你是我帶過最為憨直的一位學弟，感謝你在我最後兩年的日子，給予我的幫助，一切盡在不言中！俊榮的獨特性與學者氣息，令我深深的著迷，可惜我不是女的！李博、碩均、輝閔，不好意思，我得先走一步了，以後還會遇見你們，和你們在一起的日子，真的很快樂。此外，亦感謝謝文峰老師實驗室的阿政學長、同慶學長、維仁學長、楊松等人在實驗上的幫忙，你們的專業能力、樸實善良，都值得我們效仿。而其它沒有列出的實驗室成員，別以為你們不重要，我真的也很感謝您們，只是礙於篇幅，我只好忍痛將你們留在我心中了！

最後，我感謝我母親支身一人在家鄉的等待！我畢業了！可以回去照顧妳了！我亦感謝我的家人、親戚，所給我的鼓勵與支持！最可愛的小秋美，感謝妳這段日子不離不棄地和我在一起，有妳的扶持，讓我生命變得更為燦爛！謝謝你們！

Contents

Abstract (in Chinese) I
Abstract (in English) III
Acknowledge V
Contents VI
List of figures IX
List of tables XIV

Chapter 1 Introduction 1
1-1 Historical review of nitride based LEDs 1
1-1-1 Wurtzite III-nitride material property 1
1-1-2 Milestones for nitride based LEDs 3
1-1-3 Spontaneous and piezoelectric polarizations 6
1-2 Historical review of nonpolar GaN growth 8
1-2-1 Material characteristics of nonpolar GaN 8
1-2-2 Growth of nonpolar GaN 11
1-2-3 Nonpolar GaN applications 17
1-3 Challenges to grow nonpolar GaN based LEDs 21
1-3-1 Morphology 21
1-3-2 Threading dislocations & Stacking faults 22
1-4 Motivation 24
References 26

Chapter 2 Experimental instruments and physical models 30
2-1 Metal organic chemical vapor deposition, MOCVD 30
2-1-1 MOCVD equipment 30
2-1-2 MOCVD precursors 34
2-1-3 III-Nitride MOCVD growth 35
2-2 Electron microscopes 37
2-2-1 Basic principle of electron microscope 37
2-2-2 Scanning electron microscope 38
2-2-3 Transmission electron microscope 39
2-2-4 Cathodoluminescence 41
2-3 Atomic force microscope 42
2-3-1 Advantages of atomic force microscope 42
2-3-2 Scan modes of atomic force microscope 43
2-4 X-ray diffraction 44
2-4-1 Introduction to X-ray diffraction 45

2-4-2 X-ray diffraction system 46
2-5 Photoluminescence, PL 46
2-5-1 Temperature dependent PL 47
2-5-2 μ-PL 49
2-5-3 Time-resolved PL systems 50
2-6 Electroluminescence, EL 52
2-7 Furnace 53
References 55

Chapter 3 Development and optimization of a-plane GaN growth on r-plane sapphire 56
3-1 Difficulties to grown nonpolar GaN 56
3-2 Experimental procedure 57
3-3 Effects of different growth temperatures and pressures 58
3-4 Roles of V/ III ratio and nucleation layer 61
3-5 Observation of threading dislocation in nonpolar GaN 64
3-6 Summary 65
References 67

Chapter 4 Understanding nonpolar GaN growth 69
4-1 Wulff-plot and motivation 69
4-2 Experimental procedure 70
4-3 Forming facet of nonpolar GaN island 72
4-4 Wulff-plot of nonpolar GaN under different growth conditions 74
4-5 Reasons for pit generation in nonpolar GaN 77
4-6 Summary 80
References 81

Chapter 5 Improvement of crystal quality in nonpolar GaN 84
5-1 Methods to reduce defects of nonpolar GaN 84
5-2 Experimental procedure 85
5-2-1 Trench epitaxial lateral overgrowth technique (TELOG) 85
5-2-2 The use of InGaN/GaN superlattices 86
5-3 Growth behavior of nonpolar GaN using TELOG 87
5-4 Defects reduction of using InGaN/GaN superlattices 89
5-5 Summary 91
References 93

Chapter 6 Optical properties of nonpolar InGaN/GaN multiple quantum wells 94

6-1 Motivation 94
6-2 Sample preparation and optical measurements 95
6-3 PL characteristics of a-plane InGaN/GaN MQWs 97
6-4 Localization features in a-plane InGaN/GaN MQWs 101
6-5 Analysis of localization depth 105
6-6 Three-level localized exciton model 108
6-7 Summary 111
References 112

Chapter 7 Nonpolar optoelectronic devices 115
7-1 Motivation 115
7-2 Sample process and experiments 116
7-3 Effect of TELOG structure on electronic properties 119
7-4 Performance of nonpolar TELOG LEDs 120
7-5 Performance of nonpolar blue LEDs using superlattices 123
7-6 Summary 125
References 127

Chapter 8 Conclusion and future work 129

Publication list 132

List of figures

Chapter 1

Fig. 1-1 Unit cell of wurtzite GaN crystal……………………………………2
Fig. 1-2 The band gaps of nitrides vs. their lattice constant *a*………………3
Fig. 1-3 Band edges of conduction and valence bands……………………..7
Fig. 1-4 The monolayer schematic of atomic distribution in c-plane GaN and a-plane GaN……………………………………………………...9
Fig. 1-5 PL spectra of m-plane GaN under different polarized angle measurements……………………………………………………10
Fig. 1-6 Left image is the structural characterizations of hexagonal GaN grown on r-$LiAlO_2$…………………………………………………11
Fig. 1-7 TEM and AFM images of a-plane GaN grown on sapphire………12
Fig. 1-8 Left is the schematic of radiative emission of m-plane GaN/AlGaN MQWs and PL spectra; Right is the AFM image which shows the surface morphology of m-plane GaN…………………………...12
Fig. 1-9 a-plane GaN stripes along different directions using LEO………..13
Fig. 1-10 AFM images of surface morphology of a-plane GaN grown on (a) nanorods structure and (b) regular GaN…………………………13
Fig. 1-11 SEM cross section image of a-plane GaN grown using SALE technique……………………………………………………………14
Fig. 1-12 Left image investigated crystal quality of a-plane GaN grown using different techniques examined by XRD analysis…………14
Fig. 1-13 Triangle defect type in a-plane GaN………………………………15
Fig. 1-14 TEM images of a-plane GaN grown by HVPE……………………16
Fig. 1-15 The structural design in left figure and the results using r-plane sapphire with different off-cut angles……………………………16
Fig. 1-16 AFM images of a-plane GaN surface (a) without (b) with SiN_x nanomask…………………………………………………………...17
Fig. 1-17 Left schematic is the structure of first a-plane LED; right figure shows the luminescence spectra with different injection currents. ………………………………………………………………………18
Fig. 1-18 Left figure is the designed structure of a-plane blue LED using ELOG technique. Right figure is the spectrum results with different currents……………………………………………………18
Fig. 1-19 Left figure shows the typical structure of LED grown on free standing substrate; right figure is the output power of this device as a function of drive current……………………………………19

Fig. 1-20 Schematic of the LDs with the stripe parallel to c-axis in left figure; L-I characteristics of c- and a-axis stripe LDs in right figure…...20
Fig. 1-21 The number of publications peryear focused on nitrides with polar, nonpolar and semipolar surfaces versus time…………...21
Fig. 1-22 Bright field TEM images of a plan-view sample parallel lines represent stacking faults formed on the basal plane of GaN….23

Chapter 2

Fig. 2-1 (a) Horizontal reactor and (b) vertical reactor in MOCVD system.32
Fig. 2-2 Source bubbling and mass flow controller schematic…………….33
Fig. 2-3 In-situ reflectance measurement during MOCVD growth………..36
Fig. 2-4 The schematic of SEM equipment…………………………………39
Fig. 2-5 The schematic of TEM equipment…………………………………40
Fig. 2-6 Schematic diagram showing the operating principles of the AFM in the contact mode…………………………………………………….43
Fig. 2-7 Schematic of X-ray measurement system…………………………45
Fig. 2-8 Radiative recombination transitions in semiconductor materials. ……………………………………………………………………47
Fig. 2-9 Schematic of temperature-dependent PL setup…………………48
Fig. 2-10 Schematic of μ - PL system……………………………………….50
Fig. 2-11 Schematic of TRPL system………………………………………...51
Fig. 2-12 EL system includes all components………………………………52
Fig. 2-13 Two-zone furnace picture and schematic figure…………………54

Chapter 3

Fig. 3-1 OM images of a-plane GaN surfaces for growth temperatures of 1020~1120 ^{o}C and pressures of 100~300 torr……………………58
Fig. 3-2 Surface profiles of *a*-plane GaN epi-layers for growth temperatures of 1020~1120 ^{o}C and pressures of 100~300 torr. X is the scan direction along [1$\underline{1}$00], and Z is the height direction along [11$\underline{2}$0]. ……………………………………………………………………59
Fig. 3-3 SEM images of a-plane GaN surfaces for growth temperatures of 1020~1120 ^{o}C and pressures of 100~300 torr…………………...60
Fig. 3-4 AFM images of a-plane GaN surfaces for growth of V/III ratio of 600~1200 and on different thickness of nucleation layer………..63
Fig. 3-5 Reciprocal space mapping of *a*-plane GaN for growth temperatures of 1020~1120 ^{o}C and pressures of 100~300 torr..64
Fig. 3-6 Bright field (a) and dark field (b) cross-section TEM images of GaN

epilayer grown under optimal condition with g vector [11$\underline{2}$0]…...65

Chapter 4

Fig. 4-1 [(a) and (c)] SEM top views and [(b) and (d)] perspective views (60° inclined from *a*-axis to the in-plane *m*-axis) of the same *a*-GaN SAG mesa [(a) and (b)] before and [(c) and (d)] after a 10-min regrowth under condition A. The 5 μm scale bar applies to all the figures……………………………………………………………...71
Fig. 4-2 Kinetic Wulff plots of prism planes mapped onto the basal plane for growth conditions (a) A, (b) B, and (c) C. The region below the horizontal axis corresponds to the SiO_2 mask……………………73
Fig. 4-3 Kinetic Wulff plots of the orientations mapped onto a-planes for growth conditions (a) A, (b) B, and (c) C. The inner red trace represents the facets that are in contact with the mask and the outer blue trace the equivalent facets that are 60º rotated around c-axis (the two sets of facets are marked by blue and red lines in Fig. 4-1(b)). The traces below the horizontal axes, especially the position of the {1011} cusps, are hypothetical……………………74
Fig. 4-4 In situ optical reflectance of a-GaN growth on r-Al_2O_3 with a HT-AlN buffer. The growths of a-AlN buffer and a-GaN are marked out by shaded blue area…………………………………...76
Fig. 4-5 SEM (a) top view of m-GaN SAG mesas coalescing along c-axis; (b) perspective view of m-GaN nucleation islands on AlN/m-SiC. The coalescence between inclined {1011} and vertical (0001) (marked by red dash lines) greatly contributes to the striation along a-axis…………………………………………………………..77
Fig. 4-6 SEM (a) top view and (b) perspective view (60o inclined from a-axis to [0001]) of the same a-GaN SAG mesa; (c) SEM top view of planar a-GaN/r-Al_2O_3 surface with many pits resembling the concave void in the SAG mesa, marked out by the red dot lines. ……………………………………………………………………...79
Fig. 4-7 SEM perspective views of (a) a-GaN and (b) m-GaN SAG concave mesas grown out of the same annular openings in one OMVPE run under condition C. The both images are 60° inclined from the growth axis to the in-plane nonpolar axis…………………………80

Chapter 5

Fig. 5-1 Flow chart of a-plane GaN TELOG process………………………86

Fig. 5-2 Cross-sectional SEM of the un-coalesced TELOG a-plane GaN film with 2 μm seed /18 μm trench pattern……………………….87
Fig. 5-3 Cross-sectional TEM g=(0002) and g=(11$\underline{2}$0) two beam bright field images……………………………………………..………….88
Fig. 5-4 Cross-sectional SEM of fully coalesced TELOG a-plane GaN film with 2 μm seed /18 μm trench pattern……………………………89
Fig. 5-5 Cross sectional TEM image of a-plane GaN with SLs…………...90
Fig. 5-6 Arrhenius plots of the normalized integrated PL intensity over the temperature range 90–300 K for (a) Sample.1 and (b) sample.2 …………………………………..………………………………..91

Chapter 6

Fig. 6-1 (a) Room temperature PL spectra of a-plane InGaN/GaN MQWs with well width ranging from 3~12 nm. (b)Normalized PL intensity and energy peak plotted as a function of quantum well width…98
Fig. 6-2 The relation between PL intensity and excitation power density for a-plane InGaN/GaN MQWs with different well widths. Insert images illustrate PL spectra as functions of the excitation power for the four a-plane InGaN/GaN MQWs with different well widths. ………………………………………………………………..……..99
Fig. 6-3 (a) Monochromatic top view CL images on samples of different well widths using optical filters at the corresponding peak emission wavelengths. (b) Top view μ-PL image of the same samples using optical filters at the corresponding peak emissions wavelengths. The detected emission energies were 2.81, 2.67, 2.49 and 2.47 eV for the samples with 3, 6, 9 and 12 nm well widths, respectively…………………………………………………………100
Fig. 6-4 PL spectra as a function of temperature from 20 K to 300 K for a-plane InGaN/GaN MQWs with different well width……….…101
Fig. 6-5 PL peak energy position as a function of temperature for a-plane InGaN/GaN MQWs with different well width…………………….104
Fig. 6-6 (a) TRPL signals of emission peaks in the a-plane InGaN/GaN MQWs with different well width. (b) Relation between ln[ln{I(0)/I(t)}] and ln(t) for the signal in (a)……………………..105
Fig. 6-7 PL decay time as a function of monitored photon energy at 9K (black) and the fitting data for the a-plane InGaN/GaN MQWs with different well width (blue)………………………………………….107
Fig. 6-8 Schematic diagram of the localized exciton system. Excitons are

transferred from free/extended states to the localized states….108
Fig. 6-9 PL lifetime τ_{PL} of a-plane InGaN/GaN MQWs with different well widths as a function of temperature. The localization lifetime τ_{loc} and the nonradiative lifetime at the free/extended states $\tau_{nr,free}$, estimated from the temperature dependent TRPL signal and PL intensity are also plotted. The τ_{PL}, τ_{loc}, and $\tau_{nr,free}$ correspond to the definitions in the three-level localized exciton model shown in Fig.6-8……………………………………………………………110

Chapter 7

Fig. 7-1 Structure of the ultraviolet nonpolar TELOG LED……………….117
Fig. 7-2 Structure of a-plane LED with the insertion of InGaN/GaN superlattices………………………………………….…………118
Fig. 7-3 Cross-sectional SEM image of TELOG a-plane LED with 2 μm seed / 7 μm trench patterns……..…………………………..…..118
Fig. 7-4 (a) Plan-view SEM image, including seed regions and wing regions (b) monochromatic CL image at 373 nm and (c) monochromatic CL image at 443 nm………………………...…………………..119
Fig. 7-5 (a) L-I-V characteristics of the ultraviolet nonpolar LED, (b) Normalized CW electroluminescence spectra…………………..121
Fig. 7-6 Polarization degree of UV spectral range at the operation current of 80 mA……………………………………………………………..123
Fig. 7-7 Room-temperature EL spectra and (b) L-I-V curves for Sample.1 and Sample.2……………………………………………………124
Fig. 7-8 EL intensity of Sample.1 and Sample.2 at different polarization angles at 20 mA injection current……………………………....124

List of tables

Chapter 1

Tab. 1-1 Basic material properties of wurtzite AlN, GaN and InN…………..3
Tab. 1-2 Summary of TEM results related to a-plane GaN using SiN_x nanomask……………………………………………………………17

Chapter 2

Tab. 2-1 Common III-N material sources in MOCVD system…..…………34
Tab. 2-2 Melting temperatures and decomposition N_2 pressures for AlN, GaN and InN……………………………………………………..….34

Chapter 1 Introduction

Technical progress in the field of light-emitting diodes (LEDs) has been breathtaking during the last two decades. The main advantages of LEDs are small, rugged, reliable, bright and efficient. Most of blue LEDs are fabricated using semiconductor III-nitride materials. So far the mainstream progress is using metal organic chemical vapor deposition (MOCVD) to grown III-nitride structures on c-plane sapphire. The growth direction of these samples is along c-axis of hexagonal III-nitride structure. These productions, such like blue LEDs or ultra-violet LEDs, have been commercial in recent decade. Since build-in electric field in c-plane III-nitride devices, the typical efficiency of LEDs is still not enough to substitute current white light sources. On the other hand, unlike conventional c-plane devices, non-polar III-nitride semiconductor materials are free of polarization related electric fields along the growth direction. In theory, the emission efficiency of non-polar devices would be better than that of c-plane devices. In addition, since anisotropy structure, non-polar devices have much potential in optical application. In this chapter, I will introduce the history of III-nitride LEDs, fundamental material properties and nonpolar characteristics step by step. Finally, the current status of nonpolar GaN based materials and devices will be Epitaxy growth method of devices will also be described. Meanwhile, the difficulty and challenge of nonpolar GaN development will also be examined.

1-1 Historical review of nitride based LEDs

1-1-1 Wurtzite III-nitride material property

Most III-V compound semiconductor materials are belonged to zincblende

type crystals [1]. For III-nitride material system, they are commonly grown as wurtzite crystal [2], which exhibits a hexagonal Bravais lattice, as depicted in Fig. 1-1. In crystallography, even the wurtzite structure is closely related to the zinc-blende structure, in fact it is still a member of hexagonal crystal system. Apparently, there three main faces composed in hexagonal structure, blue plane: c face (0001), green plane: m face ($1\underline{1}00$) and red plane: a face ($11\underline{2}0$). Therefore, the wurtzite structure has a hexagonal unit cell and thus two lattice constants, c and a. Tab. 1-1 shows basic material properties of wurtzite AlN, GaN and InN [3].

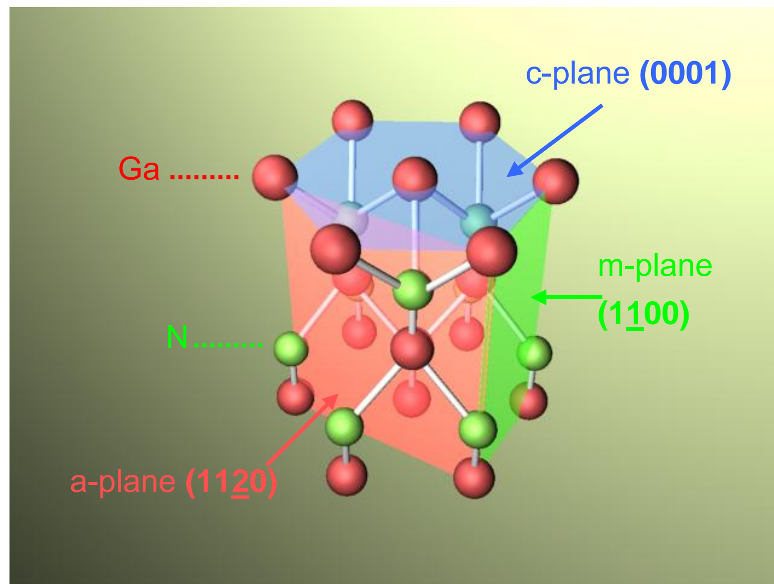

Fig. 1-1 Unit cell of wurtzite GaN crystal.

The wurtzite multi-types of GaN, AlN and InN form a continuous alloy system which has direct band gaps range from 0.7 eV for InN, to 3.4 eV for GaN, to 6.2 eV for AlN. Therefore, the III-nitride materials could be very potential to fabricate optical devices which are active at wavelengths ranging from the infrared ray (1550 nm) to ultraviolet (UV) (200 nm). The band gaps and corresponding wavelengths of nitrides are shown in Fig. 1-2 with respect to their lattice constant a [4].

Tab. 1-1 Basic material properties of wurtzite AlN, GaN and InN.

III-nitride	AlN	GaN	InN
Band gap (eV)	6.2	3.42	0.69
Lattice constant a (Å)	3.112	3.189	3.548
Lattice constant c (Å)	4.982	5.185	5.760
Dielectric constant	8.5	10.4	15.3

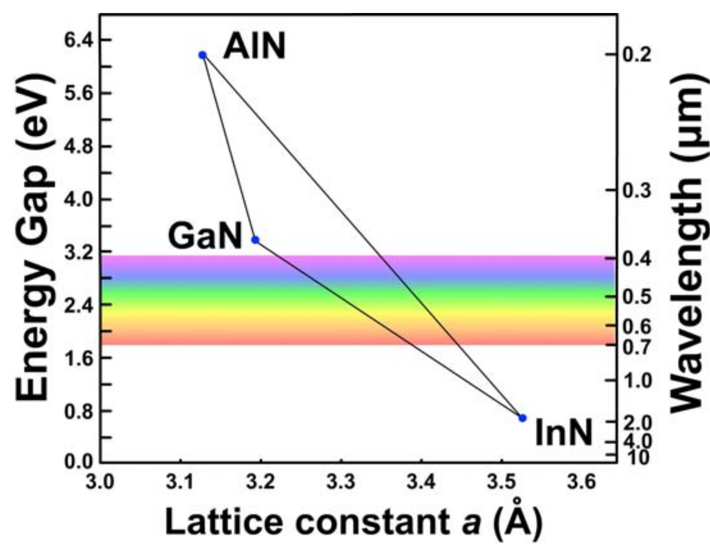

Fig. 1-2 The band gaps of nitrides vs. their lattice constant *a*.

1-1-2 Milestones for nitride based LEDs

In the history of III-nitride materials, around 1940, GaN binary alloy was first synthesized by Juza and Hahn using passing ammonia over hot gallium, and produced small needles and platelets for the purpose of studying its crystal structure and lattice constant [5]. In 1958, small crystals of GaN were produced with the same technique by Grimmeiss and Koelmans. The first result of photoluminescence (PL) spectra for GaN was demonstrated [6]. During the late 1960s, to create a full color image, the display must contain red, green and blue pixels, Maruska and Tietjen fabricated a large layer of GaN

grown on sapphire (Al_2O_3) substrate by using chemical vapor deposition technique was demonstrated [7]. As regarding the fabrication of GaN-based LED devices, the first demonstration was reported by Pankove *et al*. in 1971 [8]. This was the first current-injected GaN light emitter which emitted green and blue light. However, the early works were eventually questionable because of the lack of advanced epitaxial technique and fundamental material problems. To date, sapphire has become the most popular used substrate for the growth of III-nitride materials. This substrate has several advantages such as cheaper than SiC, high hardness, high heat-resistance, and particularly the free of absorption for green, blue, and ultraviolet photons. Despite these advantages, the material structural problem is the main issue when using sapphire as the substrate for nitride growth; as shown in Fig. 1.2, the lattice constant a of GaN is about 3.189 Ǻ with an energy bandgap of 3.39 eV. The interface between GaN and sapphire substrate exists a large lattice mismatch of 15%, causing a very high dislocation density [9, 10]. In addition, sapphire is a dielectric material, both n and p contacts shall be grown on top of the devices, and etching techniques are inevitably required. Therefore, even the sapphire can be the substrate for growing III-nitride materials, the noticeable lattice mismatch and poor crystal quality, obstacle the early development of III-nitride LEDs.

This high dislocation density problem in nitride system was not solved until 1983. Yoshida *et al.* proposed to improve the crystal quality of GaN film using AlN-coated sappire substrate [11]. Consequently, high-quality GaN thin films with smooth surface had been successfully grown by using AlN nucleation buffer layer with MOCVD technique by Akasaki *et al.* [12]. In 1991, S. Nakamura used low-temperature amorphous GaN thin films instead of AlN thin

film as new nucleation layer, and mirror-like GaN thin films were obtained under high-temperature growing [13].

Nevertheless, the high n-type background doping in intrinsic GaN film also causes a incapable issue in fabricating GaN p-n junction LEDs since a p-n junction is necessary for semiconductor devices., It could be easily achieved to obtain n-type GaN with an n-doping level of 1×10^{17} ~ 2×10^{19} cm^{-3} by Si or Se dopant atoms. In contract, for forming p-type GaN layer, even various types of acceptor atoms including Mg and C were tried, it only led to compensated high resistivity material. Until 1989 this bottleneck was first broken through by Akasaki *et al.* using low energy electron beam irradiation treatment [14]. High quality of GaN thin film with a hole concentration of 1×10^{17} and a low resistivity of 12 Ω·cm were obtained. Three years later, the Mg-doped GaN with p-doping level of 3×10^{18} cm^{-3} and a resistivity of 0.2 Ω·cm was grown which is more conductive by Nakamura who used a treatment of thermal annealing in a N_2 ambient [15].

High-brightness GaN-based blue LEDs need high-quality InGaN films as active layers. In 1990s, a blue InGaN/GaN double-heterostructure LED was first time fabricated by Nakamura. By using two-flow MOCVD technique, the substrate was heated up to 1050 ^oC in a stream of hydrogen for thermal cleaning. Then the temperature was lowered down to 510 ^oC for the growth of GaN nucleation layer. Afterward, the substrate was reheated to 1020 ^oC to grow 4-μm n-type GaN film, followed by the 20-nm-thick Si-doped InGaN active layer at 800 ^oC. The temperature was then increased to 1020 ^oC to grow p-type Mg-doped GaN film. The total thickness of structure was about 4.8 μm, and the surface of p-type GaN was partially etched until the n-type layer was exposed. Finally, a Ni–Au metal contact was evaporated onto the p-type GaN

layer and a Ti–Al metal contact was deposited onto the n-type GaN layer. The peak wavelength was 440 nm with a full width at half maximum (FWHM) of 20 nm under injective forward current of 20 mA [7].

The first candela-class blue LEDs were fabricated with the use of Si and Zn codoped InGaN active layer. The InGaN layer with low indium composition was used because of high-indium InGaN layer might degrade luminescence intensity. The thickness of InGaN active layer was 50 nm, and the active layer was sandwiched between two 150-nm-thick $Al_{0.15}Ga_{0.85}N$ cladding layers. The output power and external quantum efficiency at 20 mA were 1.5 mW and 2.7% [16]. Subsequently, the InGaN/InGaN multiple quantum wells (MQWs) structures and several novel designs were employed in GaN-based LEDs. The first commercial GaN-based LEDs were sold by Nichia Chemical Company in 1990s. To date, it is less than fifteen years that high-brightness GaN-based LEDs have been used all over the world, for example, in the applications of full-color displays, traffic signals, other promising areas of high-definition DVD optical storage, chemical processes, and medical applications [17–19].

III-nitride materials are very special. They are the best candidate for short wavelength emission due to their wide and direct energy bandgap. Unlike the arsine or phosphide materials, so far there is no any suitable substrate for nitride growth. In addition, they are in the hexagonal (wurtzite) crystal system. Therefore, the polarization effect in nitride materials has been found much stronger than other III-V compounds [20]. In next section, the material properties of wurtzite GaN and its relevant alloys are discussed.

1-1-3 Spontaneous and piezoelectric polarizations

There are two main reasons caused built-in electric fields in

semiconductors, one is spontaneous polarization P_{sp} and the other one is strain-induced polarization P_{piezo}. Comparing to other semiconductor materials, *c*-face nitride-based materials have much stronger polarization effects [20]. Polarization effect results in separation of wave functions of electrons and holes in the quantum well, as indicated in Fig. 1.3. The transition energy is reduced by the built-in field, leading to a red-shift of the emission wavelength. The thicker the quantum well thickness, the more separated electrons and holes, and the less overlap of electron and hole carrier density distributions, which leads to a smaller recombination rate and lower luminescence efficiency.

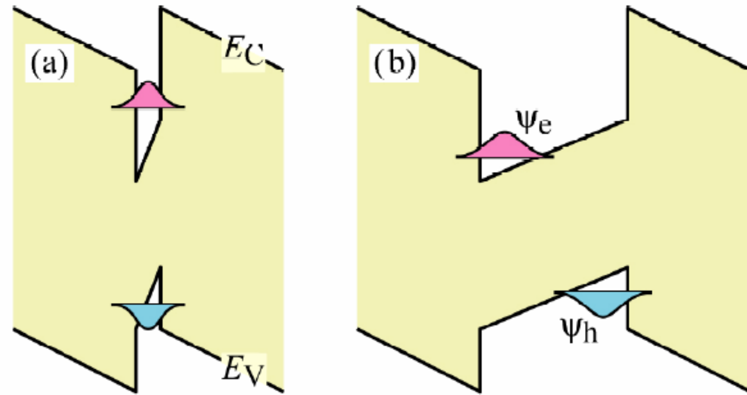

Fig. 1-3 Band edges of conduction and valence bands.

A way to estimate the interface charge density has been developed by Fiorentini *et al.* [21]. The spontaneous polarization of nitride alloys can be expressed by:

$$\begin{aligned}
P_{sp}(Al_xGa_{1-x}N) &= -0.09\cdot x - 0.034\cdot(1-x) + 0.019\cdot x\cdot(1-x) \\
P_{sp}(In_xGa_{1-x}N) &= -0.042\cdot x - 0.034\cdot(1-x) + 0.038\cdot x\cdot(1-x) \\
P_{sp}(Al_xIn_{1-x}N) &= -0.090\cdot x - 0.042\cdot(1-x) + 0.071\cdot x\cdot(1-x)
\end{aligned} \tag{1-1}$$

The piezo-electric polarization can be calculated by

$$
\begin{aligned}
P_{pz}(AlN) &= -1.808\cdot\varepsilon + 5.624\cdot\varepsilon^2 \qquad for \quad \varepsilon < 0 \\
P_{pz}(AlN) &= -1.808\cdot\varepsilon - 7.888\cdot\varepsilon^2 \qquad for \quad \varepsilon > 0 \\
P_{pz}(GaN) &= -0.918\cdot\varepsilon + 9.541\cdot\varepsilon^2 \\
P_{pz}(InN) &= -1.373\cdot\varepsilon + 7.559\cdot\varepsilon^2
\end{aligned} \tag{1-2}
$$

where ε is the in-plane strain of the binary compound considered. Linear interpolation formula is used for the calculation of ternary and quaternary nitride alloys. The total built-in polarization is the sum of spontaneous and piezo-electric polarizations.

1-2 Historical review of nonpolar GaN growth

1-2-1 Material characteristics of nonpolar GaN

Quantum confined Stark effect (QCSE) typically exists in MQWs structure especially in III-nitride system which causes build-in electric filed and degrades excitons recombination rate [22]. To eliminate QCSE, the nonpolar crystal orientations including a-axis and m-axis have been developed. The monolayer schematic of atomic distribution in c-plane GaN and nonpolar GaN are shown in Fig. 1-4 respectively. Hence, polarization discontinuities exist along the growth direction and create fixed sheet charges at surfaces and interfaces in nonpolar structure. The total polarization of III-nitride film consists of spontaneous and piezoelectric polarization contributions. These resulting internal electric fields would bend the potential band and spatially separate electron and hole wavefunctions in potential wells. According to the schematic of Fig. 1-3, this phenomenon would reduce carrier recombination、red-shift emission and decreased internal quantum efficiency. These effects are manifestations of the QCSE and have been thoroughly analyzed for GaN/(Al,Ga)N quantum wells.

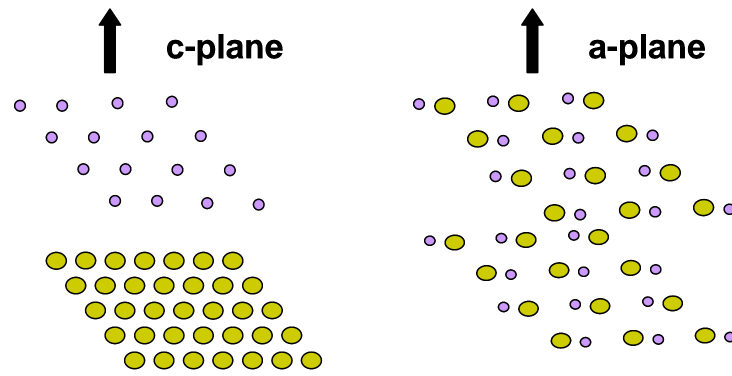

Fig. 1-4 The monolayer schematic of atomic distribution in c-plane GaN and a-plane GaN.

When commercial LEDs grown on c-plane sapphire had got to be mature gradually in market, Domen *et al.* used molecular beam epitaxy to grow m-plane GaN on SiC [23]. The optical properties and polarization effect were first revealed shown in Fig. 1-5. They found m-plane GaN could emit polarized light emission due to different amount of excitons recombined between different energy levels.

In 2000, Walterelt *et al.* grew m-plane GaN/ AlGaN MQWs structure on r-$LiAlO_2$ substrate [24]. The relationship between GaN and $LiAlO_2$ is illustrated in left of Fig. 1-6. They used time-resolved photoluminescence (TRPL) to estimate the life time of excitions existed in nonpolar MQWs structure. The life time of excitons in m-plane MQWs was averagely much decreased to 0.45 nm which is much shorter than 5.8 ns of c-plane MQWs. Therefore, they expected this kind of material could be used for advance white light source.

Most groups focused on nonpolar III-nitride concentrated their effort on growth condition, structural characteristics and polarization effect. However, the first time to demonstrate no build-in electric field in nonpolar structure is in 2002 which was carried out by Kuokstis *et al.* using power dependent PL to confirm and observe exist of internal electric field [25]. Since c-plane MQWs

possess internal electric field, the plenty injected carriers would produce an opposite electric field in well and thus cause a blue-shift PL emission due to screen effect, whereas screen effect didn't happen in nonpolar MQWs.

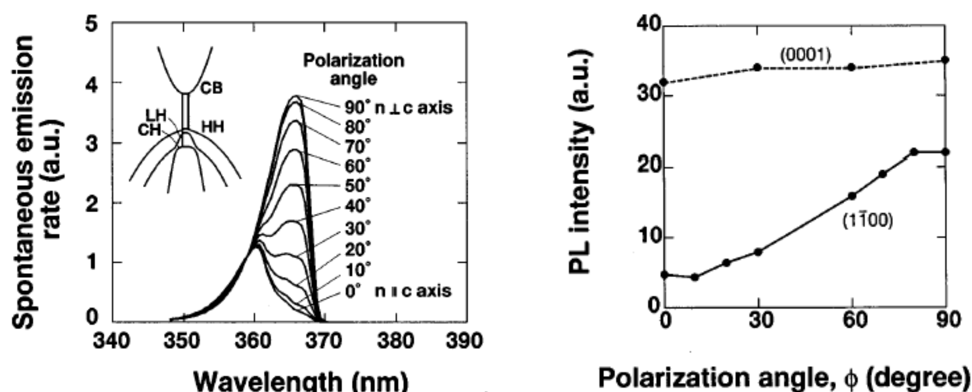

Fig. 1-5 PL spectra of m-plane GaN under different polarized angle measurements. (Appl. Phys. Lett., 71, 1996, 199)

In addition, since the growth direction of either m or a-plane GaN is perpendicular to that of traditional c-plane GaN, the hetero-epitaxial growth of nonpolar GaN always suffers biaxial stress comes from different crystal orientations. For example, the epitaxial relationships between a-plane GaN and r-plane sapphire are found to be $[1\underline{1}00]_{GaN}||[11\underline{2}0]_{sapphire}$ and $[0001]_{GaN}||[\underline{1}101]_{sapphire}$, respectively [26, 27]. Therefore, most groups believe this complicated relationship results in difficulty of nonpolar GaN growth so that the key point to develop nonpolar nitride based devices is the improvement of nonpolar GaN crystal quality.

To sum up all above descriptions, nonpolar GaN has following advantages including: free of internal electric field, high degree of polarization and expected high performance of optoelectronic devices. On the other hand, the asymmetrical strain comes from biaxial stress will be a critical issue which would make epitaxy growth difficult. Next section the growth of nonpolar GaN

will be discussed. The relevant characteristics of nonpoplar GaN in different growth approaches will also described.

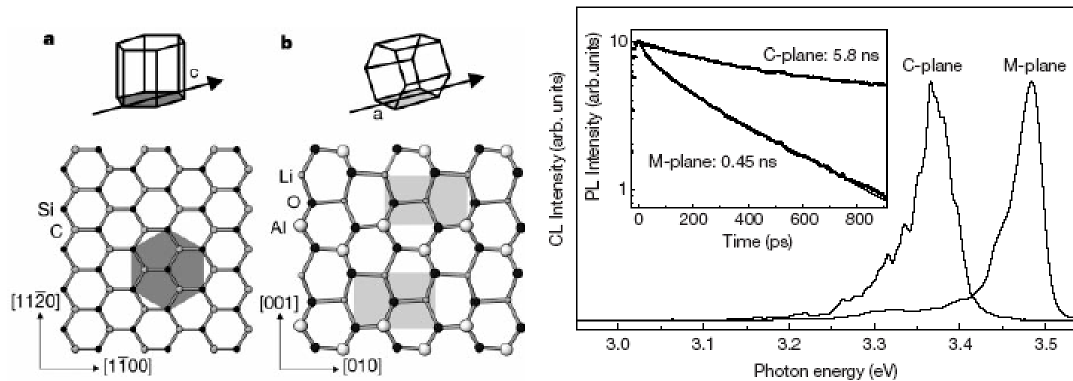

Fig. 1-6 Left image is the structural characterizations of hexagonal GaN grown on r-$LiAlO_2$.

1-2-2 Growth of nonpolar GaN

There are many techniques to grow nonpolar GaN including MOCVD, MBE and halide vapor phase epitaxy (HVPE) which are well-known and common techniques. Craven *et al.* at University of California in Santa Barbara (UCSB) studied the material properties of a-plane GaN on r-plane sapphire grown using MOCVD [28]. This debut revealed the threading dislocations (TDs) density is about $2.6\times10^{10}cm^{-2}$ which is much higher than the order of 10^7 ~10^8 cm^{-2} exist in c-plane GaN/sapphire system. In addition, the plenty stacking faults (SFs) density were also found. Surface morphology of a-plane GaN was also rough observed by atomic forced microscopy (AFM). As Fig. 1-7 left transmission electron microscopy (TEM) image and right AFM images, they suspected that plenty TDs penetrated surface and then produced pits. Since defects have the ability to trap carriers which generate radiative emission, a-plane GaN thin film can't obtain excellent optical efficiency even though nonpolar MQWs structure has better recombination rate of excitons than

c-plane MQWs has in theory.

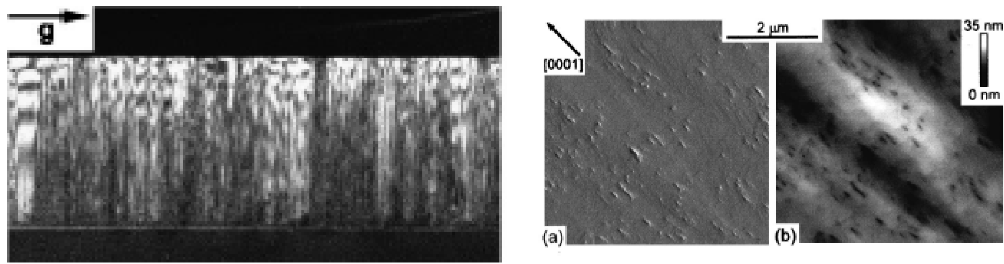

Fig. 1-7 TEM and AFM images of a-plane GaN grown on sapphire. (Appl. Phys. Lett., 81, 469, 2002)

Rau *et al.* grew m-plane GaN/ AlGaN MQWs by using MBE [29]. They confirmed polarization characteristics of nonpolar MQWs structure which revealed the strongest intensity could be obtained when electric field is perpendicular to c-axis of unit hexagonal cell. They also observed that surface morphology has tiny stripes, which is another main feature of nonpolar nitride materials [30]. Their partial results are shown in Fig. 1-8.

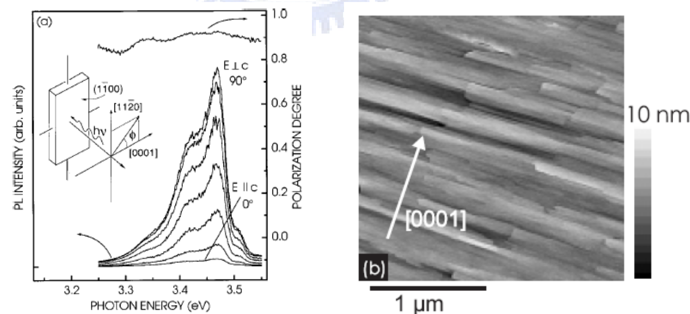

Fig. 1-8 Left is the schematic of radiative emission of m-plane GaN/AlGaN MQWs and PL spectra; Right is the AFM image which shows the surface morphology of m-plane GaN. (Appl. Phys. Lett., 77, 3343, 2000/ J. Crys. Grow. 227-228, 437, 2001)

Craven *et al.* used lateral over growth (LEO) method which was used for improvement of c-plane GaN crystal quality to reduce TDs density in a-plane

GaN [31]. SiO_2 layer of 200 nm was deposited on GaN, afterward, they defined the stripe pattern with different directions using lithography technique. The GaN stripes were grown like the image of Fig. 1-9. The TDs density in each stripe was reduced especially in $(1\bar{1}00)$ direction. Therefore, LEO method is one of approaches to improve crystal quality of a-plane GaN. In 2003, this group proposed using nanorods structure as template to improve a-GaN crystal quality [32]. They found the as-grown GaN has better crystal quality using 50 um height nanorods. Fig. 1-10 shows the AFM images with/ without using this technique. Apparently, the typical stripe feature was still shown up but the better surface morphology was really obtained using nanorods technique.

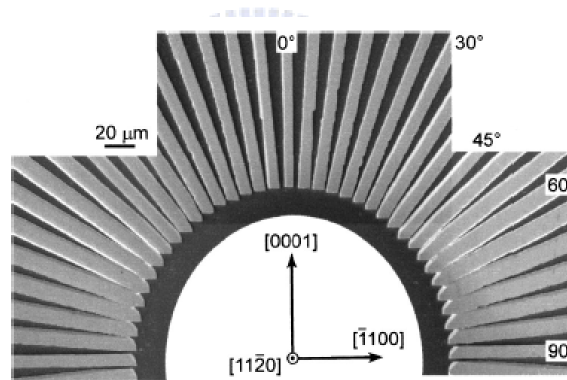

Fig. 1-9. a-plane GaN stripes along different directions using LEO. (Appl. Phys. Lett., 81, 1201, 2002.)

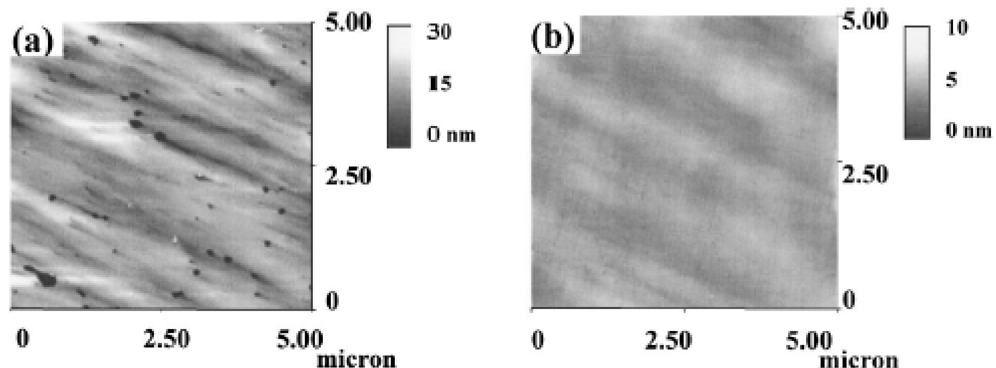

Fig. 1-10. AFM images of surface morphology of a-plane GaN grown on (a) nanorods structure and (b) regular GaN. (Appl. Phys. Lett., 83, 2599, 2003)

In addition to using nanorods structure as catalyst for LEO technique, Chen *et al.* also developed selective area lateral epitaxy approach (SALE) [33]. Using GaN with high depth-width ratio etched by lithography, following grown by SiO_2 thin layer of 300 nm for passivation. Finally they placed this sample into MOCVD reactor for further growth. As the results of scanning electronic microscope (SEM), Fig. 1-11, SALE technique reduced plenty TDs down to about $10^7 cm^{-2}$. X-ray diffraction (XRD) shows the ability of improvement is better to compare to epitaxial lateral overgrowth (ELOG). AFM image also revealed this kind GaN has mirror-like surface. The relevant results are also included in Fig. 1-12.

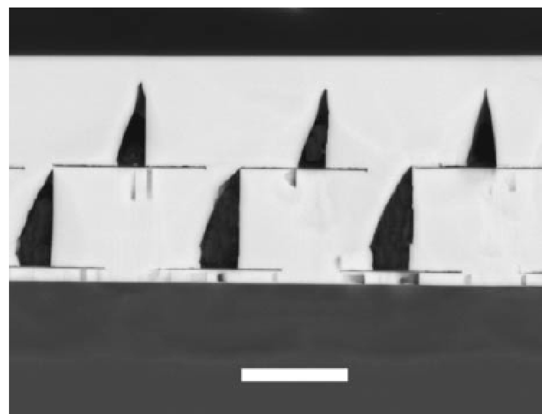

Fig. 1-11. SEM cross section image of a-plane GaN grown using SALE technique. (Jpn. J. Appl. Phys., 42, L818, 2003)

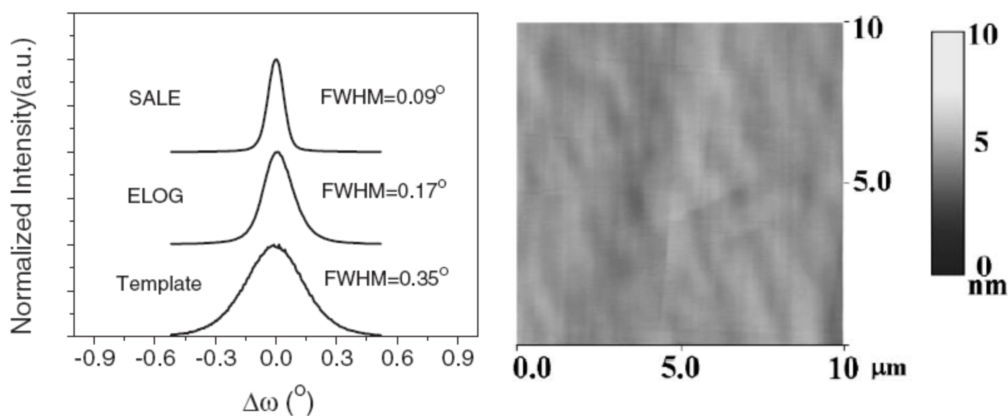

Fig. 1-12. Left image investigated crystal quality of a-plane GaN grown using different techniques examined by XRD analysis. (Jpn. J. Appl. Phys. 42, L818,

2003)

Wu *et al.* published one paper in Journal of Applied Physics which investigated the growth of a-plane GaN on r-plane sapphire in 2003 [34]. They took many methods related to analyses of material property to examine the difficulty of growth of a-plane GaN. They observed the different growth rates along m-axis and c-axis. In addition, the growth rate of Ga-polar is about four times to that of N-polar. Therefore, it is hard to get smooth surface and well crystallization of a-plane GaN. The typical V-defect occurred in c-plane GaN which is turned into another feature called <-defect composed of two tilt $\{10\bar{1}1\}$ as Fig. 1-13 shown. In the same year, 50 um thick GaN film was demonstrated and grown by using HVPE [35]. However, the above problems still can't be ruled out after further TEM observation. TDs density is about $2\times10^{10}\mathrm{cm}^{-2}$. The TEM images are shown in Fig. 1-14.

Since nonpolar unique material properties, to develop and grow materials and devices relating to a-plane GaN are very difficult. To use ELOG technique would be complicated and cost-consuming. So far a lot of groups are engaging in develop several ways to improve crystal quality of nonpolar GaN. Akasaki *et*

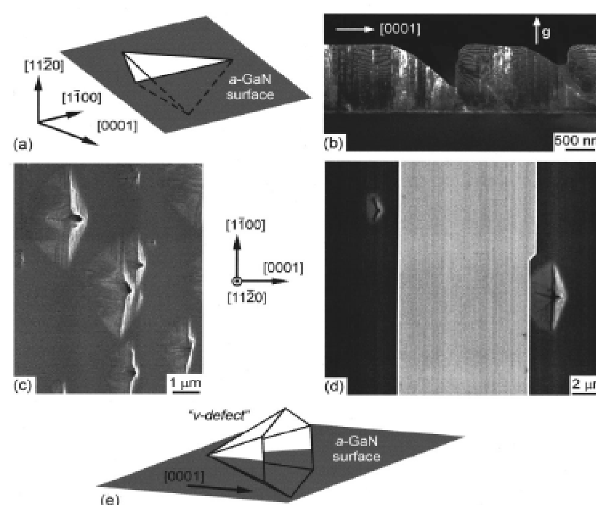

Fig. 1-13. Triangle defect type in a-plane GaN. (J. Appl. Phys., 94, 942, 2003)

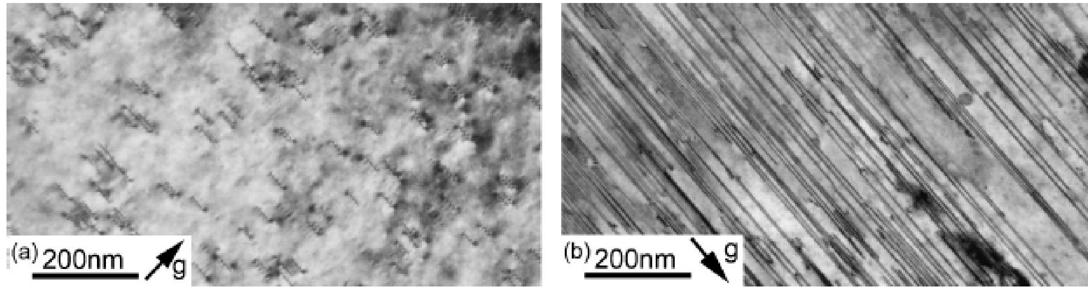

Fig. 1-14. TEM images of a-plane GaN grown by HVPE. (Appl. Phys. Lett., 83, 1554, 2003)

al. try to using double buffer layers to alleviate the problem of lattice mismatch between a-plane GaN and r-plane sapphire, the structure is shown in Fig. 1-15 [36]. In addition, they tried to grow a-plane GaN on off-cut r-plane sapphire. The results revealed the best surface obtained when using 0.5 degree off-cut r-plane sapphire. The TDs density was reduced down to $5.5\times10^{9}cm^{-2}$, the SFs densitywas lowed to $2\times10^{5}cm^{-1}$. For growth condition part, Ni *et al.* found low V-III ratio environment is benefit for growth of a-plane GaN [37].

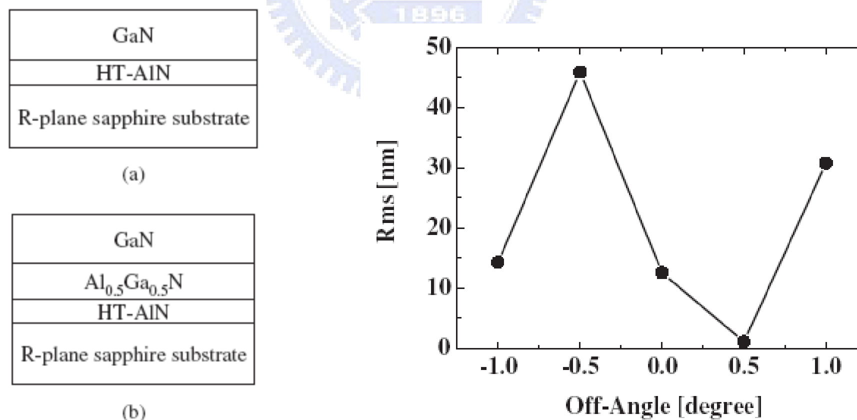

Fig. 1-15 The structural design in left figure and the results using r-plane sapphire with different off-cut angles. (Jpn. J. Appl. Phys. 44, 7418, 2005)

Recently, DenBaars *et al.* proposed using SiN_x layer as nanomask to block TDs [38]. Their experiments demonstrated TDs density was reduced to $9\times10^{9}cm^{-2}$ and SFs density was reduced to $3\times10^{5}\,cm^{-1}$, respectively. Fig. 1-16

shows their AFM results. The detailed observation results are shown in Tab. 1-2.

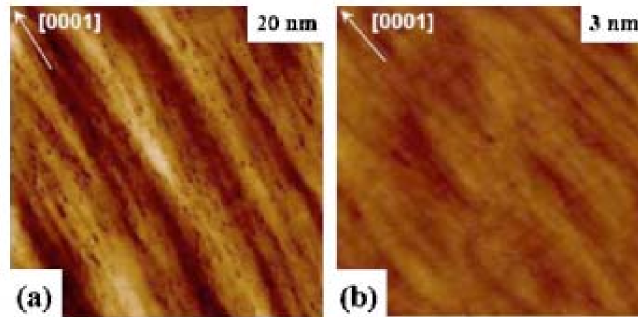

Fig. 1-16. AFM images of a-plane GaN surface (a) without (b) with SiN_x nanomask. (Appl. Phys. Lett., 89, 041903, 2006)

Tab. 1-2. Summary of TEM results related to a-plane GaN using SiN_x nanomask. (Appl. Phys. Lett., 89, 041903, 2006)

SiN_x deposition time (s)	0	120	150
TD Density (cm^{-2})	6×10^{10}–8×10^{10}	1×10^{10}–3×10^{10}	9×10^{9}
SF density (cm^{-1})	6×10^{5}–8×10^{5}	4×10^{5}	3×10^{5}

1-2-3 Nonpolar GaN applications

In theory, nonpolar optoelectronic devices should have excellent performance and have higher internal quantum efficiency than conventional c-plane devices have. However, that a bunch of defects exist in nonpolar nitride materials results in poor light extraction efficiency of optoelectronic devices. In spite of that, the possibility to fabricate a high efficient optoelectronic device is very attractive to many scientists over the world. Under this expectation, many groups have developed nonpolar GaN based optoelectronic devices including mainly nonpolar LEDs and laser diodes (LDs).

First nonpolar LED chip was fabricated in 2004 by Chitnis *et al.* [39]. In order to avoid production of plenty defects in a-plane GaN structure lead to low

performance of LED so that they grew a pretty thick n-type GaN layer of 30 μm. The structure design and spectra results are shown in Fig. 1-17. The spectrum results revealed a unusual blue-shift peak with increasing injection current. They attributed band filling and screen effect [40].

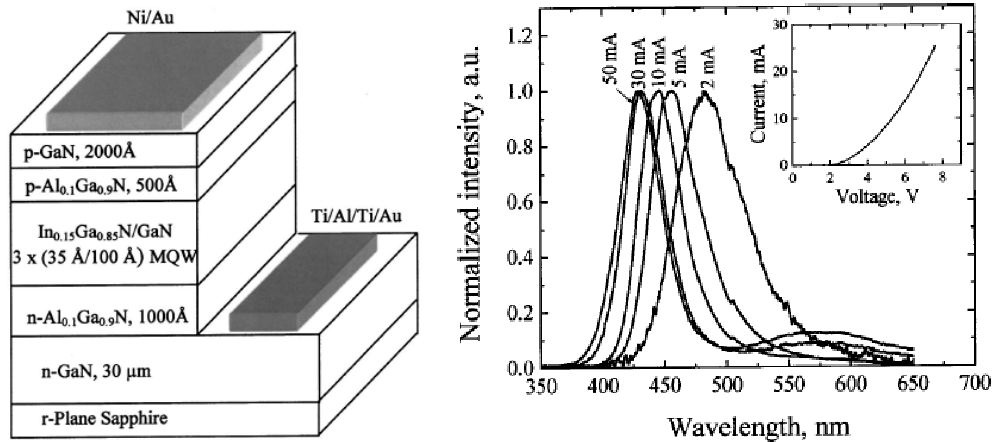

Fig. 1-17. Left schematic is the structure of first a-plane LED; right figure shows the luminescence spectra with different injection currents. (Appl. Phys. Lett., 84, 3663, 2004)

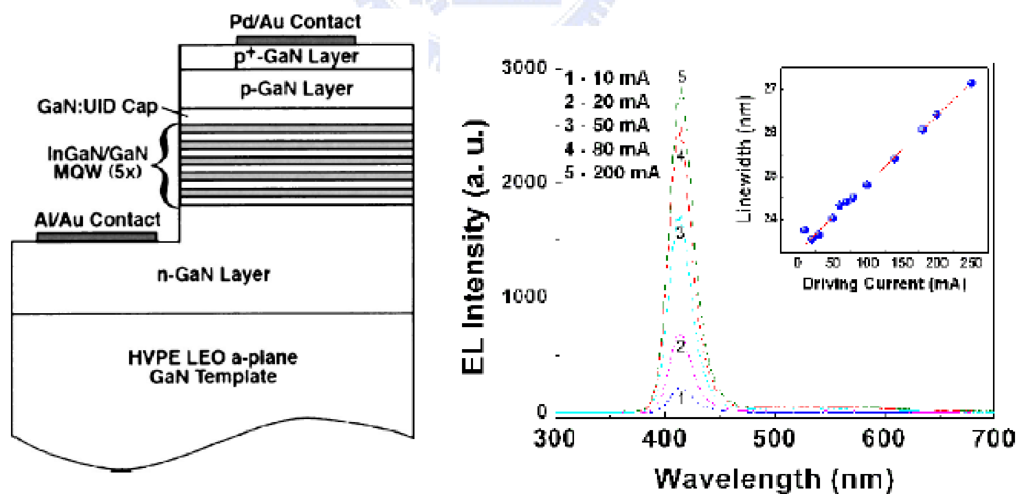

Fig. 1-18. Left figure is the designed structure of a-plane blue LED using ELOG technique. Right figure is the spectrum results with different currents. (Appl. Phys. Lett., 85, 5143, 2004)

Chakraborty *et al.* utilized ELOG substrate as a template for a-plane blue

LED which reduced much defects, the structure of LED and it's performance are shown in Fig. 1-18 [40]. The highest power was about 240 μW at 20 mA, the external quantum efficiency (EQE) is about 0.4 %. Furthermore, the power was 1.5 mW when 250 mA current was injected. The forward voltage was about 3.3 V and series resistance was about 7.8Ω. In addition, the emission didn't shift under different injection currents.

Because of much defects generation from heterostructure interface between GaN and sapphire, many groups started to select free standing a-plane GaN as substrate to resolve this problem. Chakraborty *et al.* also successfully grew m-plane LEDs with typical structure on free standing m-plane GaN substrate in 2005 [41]. The procedure of using directly free standing substrate is totally easier than using ELOG technique. On that time, the power of LED can reach 2.95 mW at 300 mA and the turn on voltage is about 3~4 V which is similar to the previous result mentioned using ELOG technique [40]. In addition, The EQE can reach 40 %. The structure and performance of this LED are shown in Fig. 1-19.

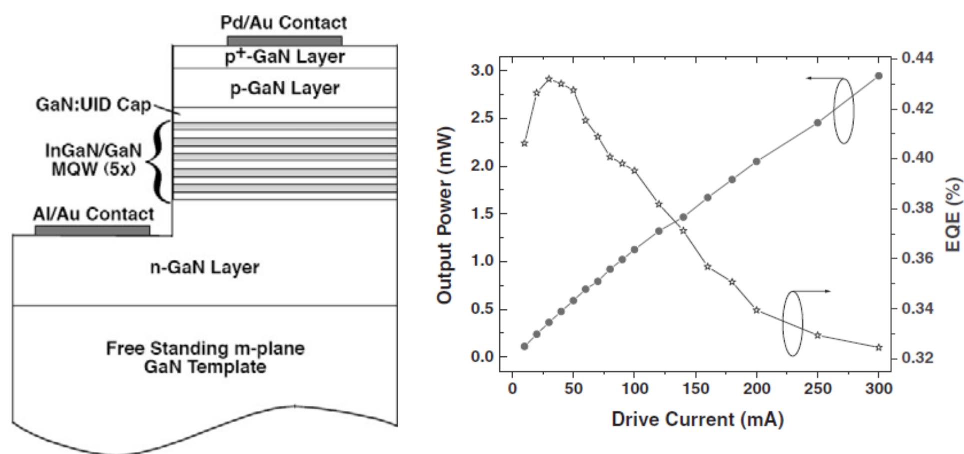

Fig. 1-19 Left figure shows the typical structure of LED grown on free standing substrate; right figure is the output power of this device as a function of drive current. (Jpn. J. Appl. Phys. 44, L173, 2005)

The first continuous-wave operation of nonpolar LDs with lasing peak approximately 400 nm was fabricated and grown on m-plane free standing GaN by Okamoto *et al.* in 2007 [42]. The threshold current was 36 mA which is comparable to that of conventional c-plane LDs. They fabricated different LDs along c-axis and m-axis, the results of Fig. 1-20 pointed out that c-axis stripe LDs exhibited lower threshold current density since the lowest energy transition is allowed. Fig. 1-20 also revealed the regular LDs structure design of nonpolar LDs.

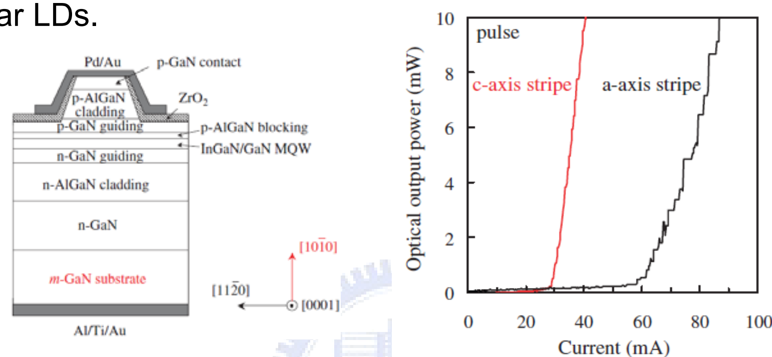

Fig. 1-20 Schematic of the LDs with the stripe parallel to c-axis in left figure; L-I characteristics of c- and a-axis stripe LDs in right figure. (Jpn. J. Appl. Phys. 46, L173, 2005)

In the same year, Feezell *et al.* proposed AlGaN-cladding free structure of nonpolar LDs and further demonstrated this possibility [43]. The pulsed lasing mode can be operated with threshold voltages and current densities of 6.7 V and 3.7 kA/ cm^2, respectively. The same group also demonstrated a high power and external efficiency m-plane blue LEDs grown on bulk m-plane GaN substrates using MOCVD [44]. The output power and EQE of packaged 300 X 300 μm2 was 23.7 mW and 38.9 % at 20 mA, respectively.

To sum up above description, during the last few years, and extensive research activity, related to growth and characterization of the nonpolar nitride material system has studied worldwide. Fig. 1-21 depicts the publication record in the scientific journals indicating the strong increase of interest in

nonpolar nitride research. Despite high-efficiency nonpolar LEDs and LDs have been demonstrated using free standing nonpolar GaN substrate, so far it is hard to get a high quality nonpolar free standing GaN substrate so that this development still can't make a progress in commercial market and other applications. Using GaN substrate is very expensive which add the difficulty to fabricate nonpolar optoelectronic devices. Therefore, to seek a good epitaxial technique and figure out the mechanism of nonpolar GaN growth are necessary for nonpolar development road. A better understanding of the specific features, properties and challenges in both growth and characterization of this material system is also required.

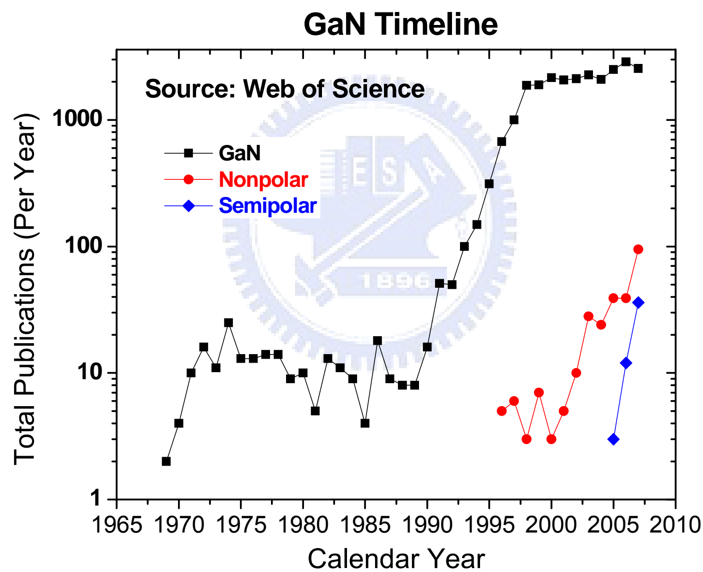

Fig. 1-21 The number of publications peryear focused on nitrides with polar, nonpolar and semipolar surfaces versus time.

1-3 Challenges to grow nonpolar GaN based LEDs

1-3-1 Morphology

The most commonly observed features of thin nonpolar nitride layer grown by both MOCVD and MBE techniques is striated. It is also called slate morphology, dominated by ridges with orientations, that appeared to be along

a-axis in the m-plane GaN films grown on (100) $LiAlO_2$ [45, 46], and along the c-axis in the a-plane GaN films grown on r-plane sapphire [47]. Many studies of the substrate morphology revealed that the stripe pattern follow the corresponding ones of the substrates and it appears that the morphologies of the nonpolar nitrides replicate the substrate morphology.

Conventional c-plane GaN grown by HVPE has hillock-type feature on surface revealed by SEM. Unlike c-plane GaN, the morphology of the thick nonpolar a-plane GaN films is stripe-shaped on a large scale with no perfect stripe orientation. The morphology of a-plane GaN layers was often reported as decorated by triangle pits. They were observed in films grown by different techniques which have been regarded as a typical surface defects under nonoptimized growth condition. The morphology was shown in Fig. 1-13. Based on previous description, Wu *et al.* revealed that the surface pits are indeed parts of three dimensional hexagonal pyramids lying in the growth plane with the tips pointing to the c-axis [34]. Therefore, the facets opposite to the tips are vertical, coinciding with the c-plane and forming an N-face wall. It is more like well-known V-type defects in c-plane GaN. This specific features of the morphology of the nonpolar heteroepitaxial films are directly related to the microstructure, such like both point and structural defects. These problems related to surface will obstacle the further structural growth of MQWs or LEDs.

1-3-2 Threading dislocations & Stacking faults

The heteroepitaxially growth of nitrides have always encountered a huge defect density. In fact, the biggest problem for crystal quality development of the nonpolar nitrides is their microstructure. Both TDs and SFs were found in nonpolar thin film. The TDs and SFs are deteimental for the lifetime of such

devices because they act as current shortcut pathways. In several reviews on the microstructure of nonpolar nitride films grown either on r-plane sapphire, a-plane SiC or $LiAlO_2$ substrates, the TDs are reported to have densities in the range of 10^{10} cm^{-2} and SFs in the range of 10^5 cm^{-1}. Different types of SFs have been revealed in the nonpolar GaN films by TEM [48]. The dominating defects were basal plane SFs, being bonded by two partial dislocations which are in accordance with the theory, which is shown in Fig. 1-22. Since the TDs and SFs originate at the interface between the substrate and film, the character of the misfit dislocations in the a-plane GaN have been evaluated by conducting detailed studies of the atomistic structure of the interface. The SFs induce built-in electric field along c-axis, with a magnitude roughly proportional to the density of SFs [49], causing in-plane carrier separation and junction leakage current [41], offsetting the benefits of nonpolar growth. Therefore, a further fully knowledge of these properties is of critical importance to understand the defect forming mechanisms in the early stages of the nonpolar GaN growth to be able to control, reduce and avoid their formation.

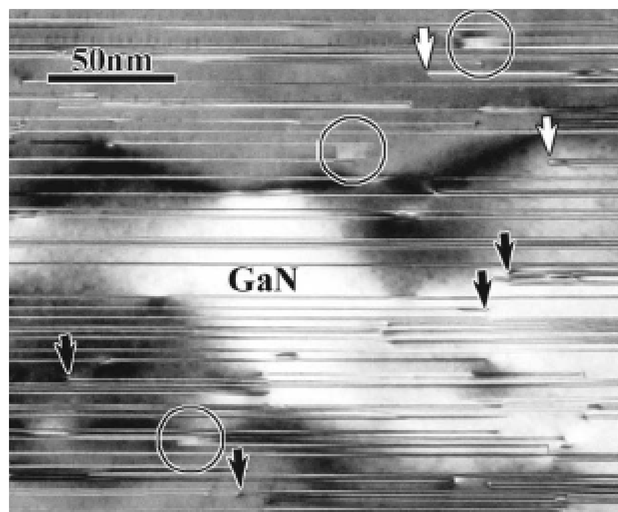

Fig. 1-22 Bright field TEM images of a plan-view sample parallel lines represent SFs formed on the basal plane of GaN. (Phys. Rev. B 71, 235334 (2005))

1-4 Motivation

Because above description about the difficulties of heteroepitaxy of nonpolar GaN either on r-plane sapphire or r-$AlLiO_2$, herein we concentrated our effort on the growth of high quality a-plane GaN with free pits on r-plane sapphire in the earlier stage of this work. The optimum growth of a-plane GaN grown on sapphire by MOCVD was investigated. The suitable growth condition for a-plane GaN was also confirmed, including growth temperature, pressure, and V/III ratio. In addition, we try to use Wulff-plot concept to figure out the growth mechanism and the pits origin of a-plane GaN by using selective area growth method. This relevant works will be discussed in Chapter 3 and 4.

In order to reduce a plenty defects exist in a-plane GaN layer, we proposed two reliable and useful methods. First one is trench epitaxial lateral overgrowth (TELOG) and the other one is the use of InGaN/GaN superlattices (SLs). Both of two methods are low cost and time-saving in comparison to some ways like using free standing nonpolar GaN substrate or ELOG. We investigated the effect of using these two approaches on the improvements of crystal quality and other fundamental material properties. The detailed report will be summed up in Chapter 5.

Before fabrication of nonpolar LEDs, we still need to examine the optimum structure of MQWs by adjusting different well width even though electric field free in nonpolar direction. The a-plane InGaN/GaN MQWs with different well widths were grown by MOCVD. By using CL and TRPL analysis, we can conclude the influence of MQWs with different well widths on carrier dynamic, recombination rate and localization degree in a-plane MQWs structure. The suitable condition for emission efficiency will be revealed and applied in further fabrication of a-plane LEDs.

Eventually, we utilized and applied previous knowledge and experimental results to grow high quality a-plane GaN template for further LEDs structure. The design of InGaN/GaN MQWs structure reported in previous work is adopted. Basic electrical and optical properties of a-plane LEDs were carried out and other relevant phenomenon were also observed and explained in Chapter 7. A series of experiments demonstrate that nonpolar LEDs is potential and capable of application of solid state lighting in future.

Reference

[1] M. J. Paisley, 2. Sitar, J. B. Posthil, and R. F. Davis, J. Vac. Sci. Tech. B 7, 701 (1989).

[2] J. I. Pankove, S. Bloom, and G. Harbeke, RCA Rev. 36, 163 (1975).

[3] H. Morkoç, “Nitride Semiconductors and Devices”, Springer, 1998, Virginia.

[4] E. Fred Schubert, “Light-Emitting Diodes”, Cambridge, 2006, New York. USA.

[5] R. Juza, H. Hahn, Z. Anorg. Chem. 239, 285 (1938).

[6] H. G. Grimmeiss, H. Koelmans, Zeitschrift Naturforschung Teil A 14, 264 (1959).

[7] G. B. Stringfellow, and M. G. Craford, “High Brightness Light Emitting Diodes: Semiconductors and Semimetals Volume 48,” Academic Press, San Diego, California, USA (1997).

[8] J. I. Pankove, E. A. Miller, J. E. Berkeyheiser, J. Luminescence 5, 84, (1972).

[9] S. D. Lester, F. A. Ponce, M. G. Craford, and D. A. Steigerwald, Appl. Phys. Lett. 66, 1249, (1995).

[10] S. Chichibu, T. Azuhata, T. Sota, and S. Nakamura, Appl. Phys. Lett. 69, 4188, (1996).

[11] S. Yoshida, S. Misawa, and S. Gonda, Appl. Phys. Lett. 42, 427, (1983).

[12] H. Amano, N. Sawaki, I. Akasaki, Y. Toyoda, Appl. Phys. Lett. 48, 353, 1986.

[13] S. Nakamura, Y. Harada, and M. Seno, Appl. Phys. Lett. 58, 2021, (1991).

[14] H. Amano, M. Kito, K. Hiramatsu, and I. Akasaki, Jpn. J. Appl. Phys. 28, L2112, (1989).

[15] S. Nakamura, T. Mukai, M. Senoh, and N. Iwasa, Jpn. J. Appl. Phys. 31, L139, (1992).

[16] S. Nakamura, IEEE J. Sel. Top. Quantum. Electron. 4, 483, (1998).

[17] J. Piprek, "Nitride Semiconductor Devices," WILEY-VCH Verlag GmbH & Co. KgaA, Weinheim (2007).

[18] G. O. Mueller and R. Mueller-Mach, "Set The Pace in White Space–White LEDs for illumination and Backlighting," Proceedings of Intertech Phosphor Global Summit, San Diago, 2005.

[19] M. Kurata, "Numerical Analysis for Semiconductor Devices," D.C. Health & Company, Lexington Massachusetts, 1982.

[20] F. Bernardini, V. Fiorentini, and D. Vanderbilt, Phys. Rev. B, 56, R10024, (1997).

[21] V. Fiorentini, F. Bernardini, and O. Ambacher, Appl. Phys. Lett. 80, 1204, (2002).

[22] D. A. B. Miller, D. S. Chemla, T. C. Damen, A. C. Gossard, W. Wiegmann, T. H. Wood and C. A. Burrus, Phys. Rev. Lett. 53, 2173 (1984).

[23] K. Domen, K. Horino, A. Kuramata, T. Tanahashi, Appl. Phys. Lett. 71, 1996, (1997).

[24] P. Waltereit, O. Brandt, A. Trampert, H. T. Grahn, J. Menniger, M. Ramsteiner, M. Reiche, K. H. Ploog, Nature 406, 865, (2000).

[25] E. Kuokstis, C. Q. Chen, M. E. Gaevski, W. H. Sun, J. W. Yang, G. Simin, M. Asif Khan, H. P. Maruska, D. W. Hill, M. C. Chou, J. J. Gallagher, B. Chai, Appl. Phys. Lett. 81, 4130, (2002).

[26] T. Sasaki and S. Zembutsu, J. Appl. Phys. 61, 2533 (1987).

[27] T. Shibata, K. Asai, Y. Nakamura, M. Tanaka, K. Kaigawa, J. Shibata, and H. Sakai, J. Cryst. Growth 229, 63 (2001).

[28] M. D. Craven, S. H. Lim. F. Wu, J. S. Speck, S. P. DenBaars, Appl. Phys. Lett.,81, 469, (2002).

[29] B. Rau, P. Waltereit, O. Brandt, M. Ramsteiner, K. H. Ploog, J. Puls, F. Henneberger, Appl. Phys. Lett. 77, 3343, (2000).

[30] P. Waltereit, O. Brandt, M. Ramsteiner, A. Trampert, H. T. Grahn, J. Menniger, M. Reiche, K. H. Ploog, J. Crys. Grow. 227, 437, (2001).

[31] M. D. Craven, S. H. Lim, F. Wu, J. S. Speck, S. P. DenBaars, Appl. Phys. Lett. 81, 1201, (2002).

[32] W. H. Sun, J. W. Yang, C. Q. Chen, J. P. Zhang, M. E. Gaevski, E. Kuokstis, V. Adivarahan, H. M. Wang, Z. Gong, M. Su, M. Ssif Khan, Appl. Phys. Lett. 83, 2599, (2003).

[33] C. Chen, J. Zhang, J. Yang, V. Adivarahan, S. Rai, S. Wu, H. Wang, W. Sun, M. Su, Z. Gong, E. Kuokstis, M. Gaevski, M. Asif Khan, Jpn. J. Appl. Phys. 42, L818, (2003).

[34] Feng Wu, M. D. Craven, S. H. Lim, J. S. Speck, J. Appl. Phys. 94, 942, (2003).

[35] B. A. Haskell, F. Wu, S. Matsuda, M. D. Craven, P. T. Fini, S. P. DenBaars, J. S. Speck, S. Nakamura, Appl. Phys. Lett. 83, 1554, (2003).

[36] M. Imura, A, Hoshino, K. Nakano, M. Tsuda, M. Iwaya, S. Kamiyama, H. Amano, I. Akasaki, Jpn. J. Appl. Phys. 44, 7418, (2005).

[37] X. Ni, Y. Fu, Y. T. Moon, N. Biyikli, H. Morkoç, J. Crys. Grow. 290, 166, (2006).

[38] A. Chakraborty, K. C. Kim, F. Wu, J. S. Speck, S. P. DenBaars, U. K. Mishra, Appl. Phys. Lett. 89, 041903, (2006).

[39] A. Chitnis, C. Chen, V. Adivarahan, M. Shatalov, E. Kuokstis, V. Mandavilli, J. Yang, M. A. Khan, Appl. Phys. Lett. 84, 3663, (2004).

[40] A. Chakraborty, B. A. Haskell, S. Keller, J. S. Speck, S. P. DenBaars, S. Nakamura, U. K. Mishra, Appl. Phys. Lett. 85, 5143, (2004).

[41] A. Chakraborty, B. A. Haskell, S. Keller, J. S. Speck, S. P. DenBaars, S. Nakamura, U. K. Mishra, Jpn. J. Appl. Phys. 44, L173, (2005).

[42] K. Okamoto, H. Ohta, S. F. Chichibu, J. Ichihara, H. Takasu, Jpn. J. Appl. Phys. 46, L173, (2007).

[43] D. F. Feezell, M. C. Schmidt, R. M. Farrell, K. C. Kim, M. Saito, K. Fujito, D. A. Cohen, J. S. Speck, S. P. DenBaars, S. Nakamura, Jpn. J. Appl. Phys. 46, L284, (2007).

[44] M. C. Schimidt, K. C. Kim, H. Sato, N. Fellows, H. Masui, S. Nakamura, S. P. DenBaars, J. S. Speck, Jpn. J. Appl. Phys. 46, L126, (2007).

[45] B. A. Haskell, A. Chakraborty, F. Wu, Journal of Electronic Materials 34, 357 (2005).

[46] Y. J. Sun, O. Brandt, K. H. Ploog, J. Vac. Sci. Tech. B 21, 1350 (2003)

[47] H. Wang, C. Chen, Z. Gong, J. Zhang, M. Gaevski, M. Su, J. Yang, M. Asif Khan, Appl. Phys. Lett. 84, 499 (2004).

[48] D. N. Zakharov, Z. L. Weber, Phys. Rev. B 71, 235334 (2005).

[49] G. D. Metcalfe, H. Shen, M. Wraback, A. Hirai, F. Wu, and J. S. Speck, Appl. Phys. Lett. 92, 241106 (2008).

Chapter 2 Experimental instruments and physical models

MOCVD, XRD, all kinds of electronic microscopy and spectra, were widely used for this thesis works, the detailed description of the instruments will be introduced in this chapter. For an excellent epitaxial grower, to understand basic theory and principle of machine is the most important because it could dominate whether crystal quality is perfect or not. In addition, the analyses of material properties are worth being carried out in order to obtain whole material information which can help us evaluate applications. Therefore, the content of this chapter we will mentioned involves system schematic, operation principles and fundamental knowledge.

2-1 Metal organic chemical vapor deposition, MOCVD

MOCVD is currently the most widely used technology for nitride compound semiconductor thin film growth. Actually, most of all optoelectronic commercial device structures are fabricated using MOCVD. Its potentials have been proven by producing high quality epitaxial layers with excellent surface morphology and a precise control over layer thickness and uniformity. Some epitaxial crystal growth technology for an impressive array of commercial devices are also carried out by MOCVD, such like lasers, LEDs, photocathodes, heterostructure bipolar transistors, photodetectors, and solar cells [1-3].

2-1-1 MOCVD equipment

MOCVD growth is facilitated by introducing group III precursors and NH_3 with carrier gases into a reactor under appropriate growth temperature and growth processes. In general, a typical MOCVD system consists of four major parts; growth reactor, gas delivery system, heating system, and exhaust system.

I. Main reactor chamber

The reactor system for carrying out CVD processes must provide several basic functions to all types of systems. Most reactants and diluent gases were allowed to move to the reaction site and absorb activation energy while maintaining a specific system pressure and temperature. Moreover, the reactor also allows the chemical reactions for epitaxial film growth optimally and to exhaust out the by-product gases and vapors. These functions must be operated with adequate control, maximal effectiveness, and complete safety.

The reaction chamber is more like the heart of human which is connected the vessel, all kinds of source gases are mixed and introduced into a heated zone where an appropriate substrate is placed, and then the basic pyrolysis reactions described above take place. There are two basic MOCVD reaction chamber geometries commonly used for epitaxial III-nitride growth [4, 5]. One is vertical reactor chamber, the other is horizontal one, which are mainly fabricated by famous companies Veeco and Aixtron [6, 7]. For both designs, cold-wall systems are attached which contain a relatively small diameter inlet into some form of transition region and make use of an indirectly heated (filament or radio-frequency induction heated) silicon carbide-coated graphite susceptor. In this thesis, I used Veeco D75 MOCVD with vertical reactor at NCTU, the relevant results will be discussed in further chapter 3, 5, 6 and 7 except for partial content of chapter 5. Aixtron 200 MOCVD was used at Yale

to carry out growth behavior of nonpolar GaN, which will be mentioned in whole chapter 4 and partial chapter 5. Therefore, this understanding in terms of growth behavior of nonplar GaN still will not conflict with other results.

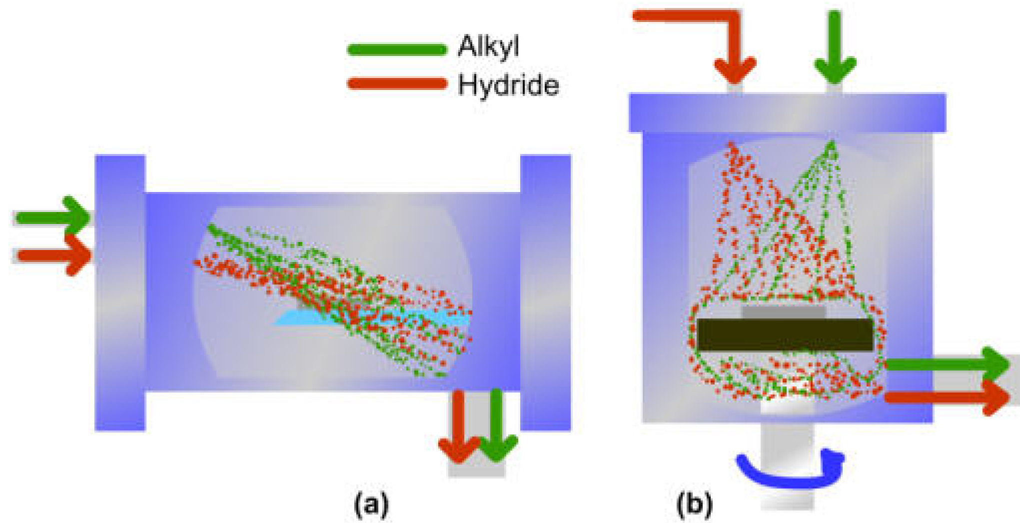

Fig. 2-1 (a) Horizontal reactor and (b) vertical reactor in MOCVD system.

In the horizontal reaction chamber is shown in Fig. 2-1(a), the precursors and gases enter from the small inlet to the left and expand to an approximately laminar flow across the heated susceptor. Whole 2 inch wafer or small pieces can be accommodated along the length of the susceptor, or be placed side by side if the susceptor area is large enough. Hydrogen flow from the bottom side can flow in the special designed pattern on the down side of puck and lead to rotation of puck. In contrast, in the vertical reaction chamber shown in Fig. 2-1 (b), the process gases enter at the top and are deflected by a baffle before moving downward through a cold transition region and approaching normal to the heated susceptor. The gas flow is forced to the sides by the susceptor with a velocity profile dependent on geometry and affected by the thermal profile in the system. Uniformity could be improved by rotating the susceptor. Exhaust gases escape through the base of the reaction chamber. 2 inch water is allowable for growth but small pieces can not be loaded on susceptor due to

high rotation speed of around 900 rpm.

II. Gas delivery system

The gas delivery system consists of all the valves, mass flow controllers, regulators, and equipment for transporting sources for further growth in the reactor chamber. Therefore, it is important to control the gas flows, mixtures, and gas distribution into the chamber as well as to keep gas plumbing clean and leakage-free.

III. Load lock chamber and others

The substrate is placed on a wafer carrier in reactor under a relative low pressure to outside environment. Therefore, one buffer zone is necessary which supply a pressure-control space for loading samples. For example, load lock chamber in Veeco system and glove box in Aixtron system. In addition, we need to ensure the Safety of use MOCVD which is the most important issue because of various toxic gases used as sources. Process gases should be piped in leak-free plumbing with nitrogen or vacuum in the outer tube. Waste gases should be processed with filters, combustion discharge, oxidation, wet chemical scrubber, or a combination of these methods. Automatic shutdown of source gases and a switch to inert purge gases should take place in the event of power failure when inadequate backup power is available.

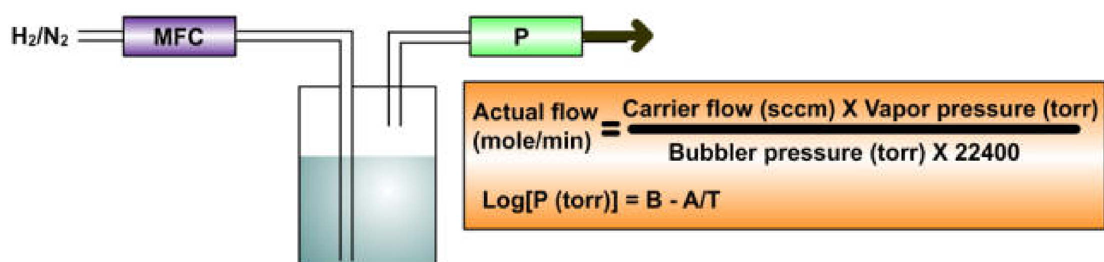

Fig. 2-2 Source bubbling and mass flow controller schematic.

Moreover, Fig. 2-2 shows a schematic of source bubbling and metal

organic (MO) sources in Tab. 2-1, which are commonly utilized to grow III-nitride materials using MOCVD.

Tab. 2-1 Common III-N material sources in MOCVD system.

Compound		P at 298 K (torr) Log P = B – A/T	A	B	Melt point (^oC)
$(CH_3)_3$ Al	TMAl	14.2	2780	10.48	15
$(CH_3)_3$ Ga	TMGa	238	1825	8.50	-15.8
$(CH_3)_3$ In	TMIn	4.79	2530	9.19	-82.5
$(C_5H_5)_2$ Mg	Cp_2Mg	0.05	3556	10.56	175

Tab. 2-2 Melting temperatures and decomposition N_2 pressures for AlN, GaN and InN.

III-nitride	T_{melt} (^oC)	E_{bond} (eV)	P_{dec} (torr)
AlN	~ 3500	11.52	2E6
GaN	~ 2800	9.12	3.4E7
InN	~ 2200	7.72	4.5E7

2-1-2 MOCVD precursors

As seen in tab. 2-2, trimethyl and triethyl molecules are widely used for the group III precursors. TrimethylGallium (TMGa), trimethylaluminium (TMAl), and trimethylindium (TMIn) are commonly used. They have high vapor pressure at room temperature. Most sources have high vapor pressure and are delivered using carrier gases. These sources should be easily synthesized and purified and have reasonable vapor pressures. Hence, these are

transferred to the reactor with carrier gases. Ammonia (NH_3) is usually used as the nitrogen source. The gas phase of NH_3 has strong bond energy and a very high thermal stability, therefore, a relatively high temperature is needed to decompose NH_3. On the other hand, NH_3 prevents the deposited film from decomposing under this high temperature. In addition, hydrogen is commonly used as a carrier gas for MOCVD. Sometimes, nitrogen could be substituted for hydrogen. But the nitrogen as the carrier gas should be high clean and treated with purification by an appropriate point of use purifier.

2-1-3 III-Nitride MOCVD growth

An in-situ normal incidence reflectometry is usually attached in MOCVD machine which is capable of monitoring the growth processes in real time. The overall reflectivity can determine growth rate and growth status results from overlapping the reflectance of light from different interfaces. During the growth, the interference conditions change, causing the sample reflectivity to oscillate with a frequency determined by the growth rate, the incident wavelength, and refractive index of the layers. Fig. 2-3 shows the in-situ measurement data during GaN growth. It is clear to see a normal GaN growth process has a two-step process which is a low temperature buffer followed by high temperature GaN growth.

I. Pre-baking substrate: chamber temperature ramps up to 1100 ºC and the substrate is heated around 10 minutes under hydrogen ambient. The substrate is clean and has a good surface quality after this process. NH_3 could be introduced which leads to a nitridation of the substrate surface for the addition growth application such like N-polar GaN growth [8].

II. Low temperature GaN growth: after the pre-baking, the temperature ramps down to 550 ºC. A GaN or AlN nucleation layer is deposited on the substrate for a couple of minutes. The purpose of nucleation layer is to reduce the residual stress from lattice mismatch between GaN and sapphire and avoid producing many intrinsic defects. Nucleation layer thickness is an important factor affecting GaN layer quality. The thickness is generally between 20 ~ 40nm.

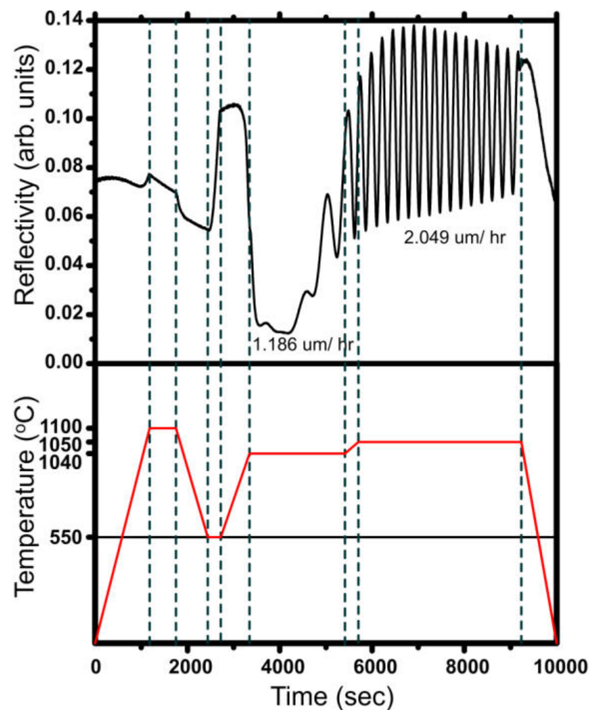

Fig. 2-3 In-situ reflectance measurement during MOCVD growth.

III. Thermal activation of the nucleation layer: the nucleation layer's crystal quality is poor due to low temperature growth. The nucleation layer is recrystallized while ramping the temperature to 1050 ºC under NH_3 ambient. These two processes result in strain relief caused by lattice mismatch from the substrate and high density of nucleation which facilitate to further GaN growth.

IV. Rough GaN growth: before the main GaN layer growth, a rough GaN

with low growth rate is grown at 1040 ºC. The growth rate is lower than that of main GaN growth. This process improves the main GaN crystal quality.

V. GaN growth: the main GaN layer is also grown at around 1050 ºC. The general growth rate in MOCVD growth is about 2 μm/ hour which could be adjusted mainly by TMGa flow rate, growth temperature and V/III molar ratio.

2-2 Electron microscopes

Generally, a modern optical microscope has a magnification of about 1000x and enables the eye to resolve objects separated by 0.0002 mm. Not only to improve quality of the lenses can get better resolution but also to reduce the wavelength of the light used for illumination. It was impossible to resolve points in the object which were closer together especially in only few hundred nanometers. In the 1920s it was discovered that accelerated electrons behave in vacuum just like light. The electrons travel in straight lines and have a wavelength which is about 0.1 million times smaller than that of light so that electronic microscope can have excellent resolution power. In this section, the basic principle of some kinds of electronic microscopy will be introduced. The fundamental equipments, for example, cathodoluminescence (CL) will also described in this section.

2-2-1 Basic principle of electron microscope

Electron microscopes have greater resolving power than optical microscopes and can obtain higher magnifications. Some electron microscopes can magnify sample up to 1 million times, whereas the best

optical microscopes could be limited to magnifications of 2000 times. The resolution limitations of both electron and light microscopes were imposed by their wavelength. The greater resolution and magnification of the electron microscope is because an electron has much shorter wavelength than photon has, named de Broglie wavelength. The first de Broglie equation relates the wavelength λ to the electron momentum P could be expressed as below [9]:

$$\lambda = \frac{h}{P} \tag{2-1}$$

where h is Planck's constant.

Electrostatic and electromagnetic lenses are used to form the image by adjusting the electron beam to focus sample by a specific plane, which is pretty close to how a optical microscope uses glass lenses to focus light on a sample to generate an image.

2-2-2 Scanning electron microscope

Multiple electron types generated from the sample surface as the sample is bombarded by high energy electrons include secondary electrons, backscattered electrons, Auger electrons and transmitted electrons [10]. The main source of SEM images comes from the measurement secondary electrons. All the components of a SEM are usually placed in one carrier which is shown in Fig. 2-4. The right part is the electron optical column mounted on top of the sample chamber. Below this is the vacuum system in the cabinet. The left part is the display monitor, plus the computer components which are for controlling the microscope and the camera. At the top of the column, the electron gun produces electron beam to focus into a fine spot less than 4~6 nm in diameter on the specimen. This beam is scanned in a rectangular shape

over the specimen. Except for other interactions at the specimen, secondary electrons are produced and these are detected by a detector. The amplitude of the secondary electron signal varies with time dependent on the topography of the specimen surface. The signal is amplified and used to generate the electron beam in a cathode ray tube (CRT) to vary in action. Both the beam in the microscope and the one in the CRT are scanned at the same rate. There could be each point on the CRT screen and a corresponding point on the specimen. Therefore, a picture is built up. The ratio of the size of the screen of the CRT to the size of the area scanned on the specimen is determined as the magnification. Whole image will be generated by photographing the monitor screen, storing a digital image and making video prints.

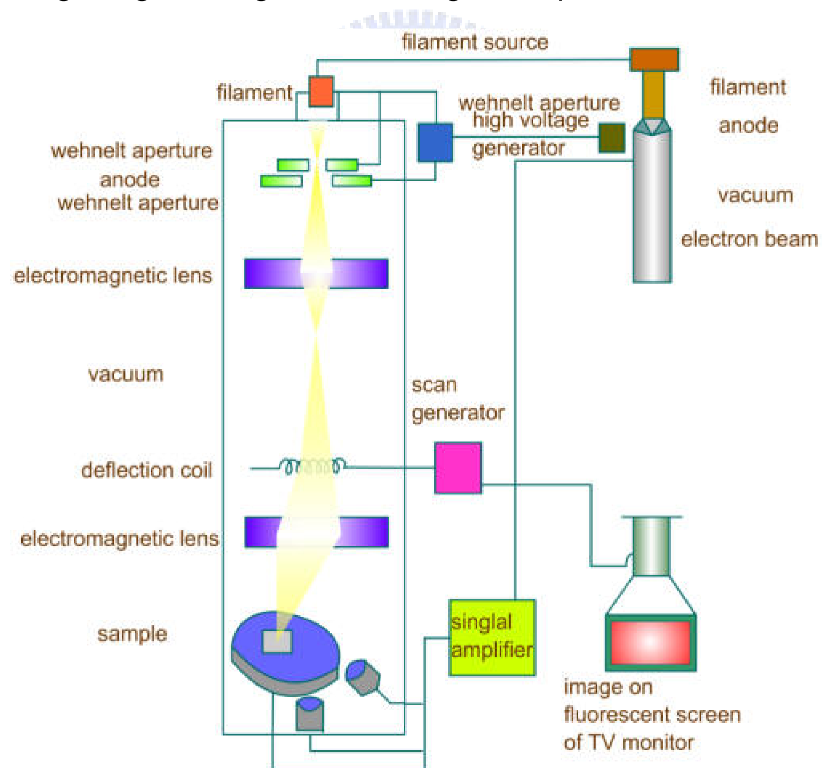

Fig. 2-4 The schematic of SEM equipment.

2-2-3 Transmission electron microscope

In comparison to a light microscope, the wavelength of illumination

produced by an energized beam of electrons in TEM increases greatly the resolving capabilities. Therefore, the main application of this technique is to examine the specimen structure, composition or properties within nanometer range so that TEM is significantly involved in numerous fields such as chemistry, electronics, biological components and materials science.

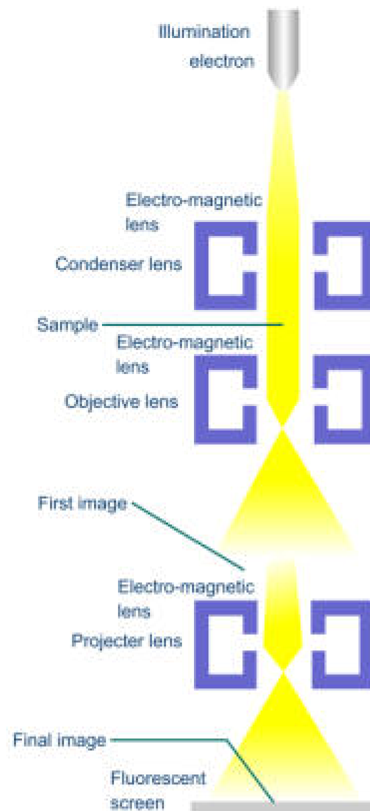

Fig. 2-5 The schematic of TEM equipment.

The basic structure of TEM is shown in Fig. 2-5. Three essential types of lenses are used to form the final image in the TEM and they are condenser, objective, and projector lenses. The function of the condenser lens is to focus the beam of electrons coming from the filament onto the sample to give a uniformly illuminated sample. The objective lens system is the main part of the TEM. In addition, the TEM can build a differential-contrast image. Those electrons that pass through the sample while those that are stopped or

deflected by dense atoms in the specimen where will go on to form the low contrast image. Therefore, in this way a black and white image is formed. Some electrons pass close to a heavy atom and are thus only slightly deflected. These electrons eventually make their way down the column and contribute to the image. An aperture in the objective lens is used in order to eliminate these scattered electrons from the image that will stop all those electrons that have deviated from the optical path. To use the smaller aperture can stop the more of these electrons to scatter and our image contrast will become better. Finally, these electrons finally project onto the phosphor screen or photographic emulsion. Objective, projector and intermediate lens are used and further define total magnification. Eventually, the image is then projected onto either the fluorescent screen or onto the photographic film.

2-2-4 Cathodoluminescence

CL is a very useful technique for studying the optical properties of semiconductor structures. Spatially resolved CL is usually attached in SEM and performed using the focused electron beam. The main capability of CL is to vary the acceleration voltage of the SEM to obtain emission from the sample in the z-axis direction. In combination with the normal x-y (in-plane) resolution, it is possible to generate two-dimensional maps of the emission.

There is a parabolic mirror placed above the stage in the CL system, and the sample is in its focal plane. The resulting parallel light beam is transmitted through an optical window in the chamber wall and focused onto the entrance slit of a monochromator. Following the emission will be detected by photo detector.

2-3 Atomic force microscope

AFM can scans surface image and measure some properties of material, chemical, and biological surfaces. AFM images are obtained by scanning a sharp probe across a surface while monitoring and compiling the tip–sample interactions. AFM is one primary type of scan probe microscope, the other one is scanning tunneling microscopy (STM). STM was first developed in 1982 at IBM in Zurich by Binnig, *et al.* [11]. The invention of the STM has had a great impact on the technical development by providing a new and unique tool to advance fundamental science and technology. But only good electrical conductors are candidates for this technique even though the ability of the STM has high atomic resolution. Until invention of atomic force microscope generated by Binnig, Quate, and Gerber [12], this problem has been overcome since the detection of atomic is capable of a wide range of insulating surfaces that include biological samples, ceramic materials, and polymers.

2-3-1 Advantages of atomic force microscope

AFM provides a number of advantages over conventional microscopy techniques. Enabling the presentation of three-dimensional images of a sample surface while AFM scan the sample and make measurements in three dimensions, x, y, and z. This provides a great advantage over any microscope available previously. High resolution in the x-y plane ranges from 0.1 to 1.0 nm and in the z direction 0.01 nm can be obtained for excessive good samples. AFM requires neither a vacuum environment nor any special sample preparation, and they can be used for all kind samples even in liquid environment.

2-3-2 Scan modes of atomic force microscope

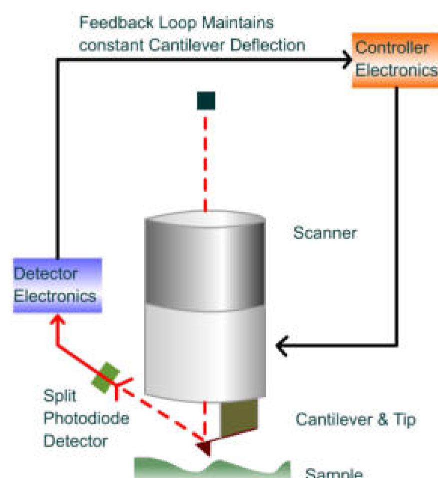

Fig. 2-6 Schematic diagram showing the operating principles of the AFM in the contact mode.

There are two main approaches to obtain AFM images. One is contact mode and the other one is tapping mode. The schematic of the contact mode AFM is shown in Fig. 2-6. The AFM tip is first attached manually close to the sample surface, and then the scanner makes a final adjustment between tip and sample based on a set point determined by the user. The tip is in contact with the sample surface through any adsorbed gas layer, is then scanned across the sample under the action of a piezoelectric actuator, either by moving the sample or the tip relative to the other depend on different AFM machine. A laser beam locateded at the back of the cantilever–tip reflects off the cantilever surface to a photodiode, which detects the small cantilever deflections. Fig. 2-6 also shows a feedback loop, maintains constant tip–sample separation by moving the scanner in the z direction to maintain the set point deflection. This feedback loop is necessary otherwise the tip would hit the sample surface with even small topographic features.

By maintaining a constant tip-sample separation and using Hooke's Law (F = -kx where F is force, k is the spring constant, and x is the cantilever deflection), the force between the tip and the sample is calculated. Eventually, the distance the scanner moves in the z direction is stored in the computer relative to spatial variation in the x-y plane to generate the topographic image of the sample surface.

However, contact mode still suffers from a number of drawbacks that limit its use on a number of sample types. First, the constant downward force on the tip often damages sample surface. In addition, many samples include nano particles or biological samples like DNA and cells, need to be placed on a substrate for imaging purposes. Therefore, for most cases, the sample is often destroyed in contact mode. These problems have been addressed through the development of TappingMode AFM. In the TappingMode, the AFM tip–cantilever assembly oscillates at the sample surface while the tip is scanned, afterward, the tip taps the sample surface softly and only touches the sample at the bottom of each oscillation. This can prevent damage to sample surface and tip. A constant distance between tip and sample is maintained until the scan is completed by using constant oscillation amplitude.

2-4 X-ray diffraction

XRD is used to determine the phase content in many minerals and materials. Since Hull wrote a paper titled, "A New Method of Chemical Analysis" In 1919 [13], the same substance always gives the same pattern this discover has been demonstrated. Therefore, each material has individual crystal phase content corresponding to lattice constant. XRD pattern of a pure substance is like a fingerprint of the material. XRD method is thus ideally

suited for characterization and identification of polycrystalline phases.

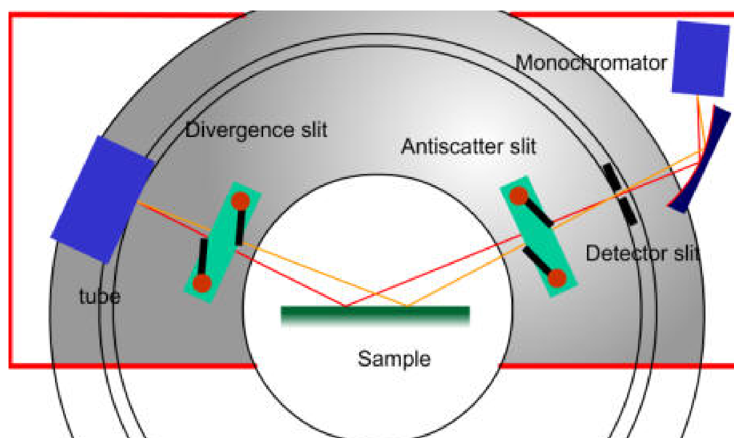

Fig. 2-7 Schematic of X-ray measurement system.

2-4-1 Introduction to X-ray diffraction

X-rays are electromagnetic radiation with typical photon energies in the range of 100 eV - 100 keV. Only short wavelength x-rays (hard x-rays) in the range of a few angstroms to 0.1 angstrom (1 keV - 120 keV) are used for diffraction applications. Because the wavelength of x-rays is as short as the size of atoms, they are ideally suited for probing the structural arrangement of atoms and molecules in all kind of materials. The energetic x-rays can penetrate into the materials and provide crystal information about the bulk structure.

X-rays are generated generally by either x-ray tubes or synchrotron radiation. In a regular x-ray tube, when a focused electron beam accelerated across a high voltage field bombards a stationary or rotating solid target and then x-rays are generated. As electrons collide with atoms in the target and slow down, a continuous spectrum of x-rays are emitted. When a free electron fills the shell, a x-ray photon with energy characteristic of the target material is emitted. Cu and Mo are common targets used in x-ray tubes, 8 keV and 14

keV x-rays with corresponding wavelengths of 1.54 Å and 0.8 Å are available, respectively.

2-4-2 X-ray diffraction system

Typical XRD equipment consists of three main parts which are X-ray tube, detector and diffractometer slit system. The schematic of XRD is shown in Fig. 2-7. There is one attached X-ray tube on one machine arm which emits x-ray of 1.5 Å from Cu Kα radiation. The collected emission can be detected after these signal passes through monochromator attached on the other side machine arm. Three kinds of slits, divergence slits, antiscatter silts and detector slits, are commonly used to improve the space resolution of X-ray during measurement.

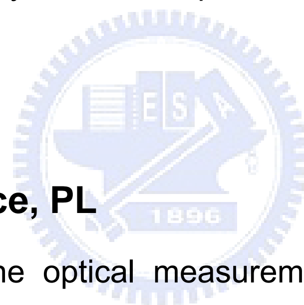

2-5 Photoluminescence, PL

PL spectroscopy is the optical measurement method to examine the quality and optical characteristics of material, it has the advantage of an un – contact and nondestructive. PL is the emission of light from a material under optical excitation. To excite the material to induce the emission, the energy of the excited light source should be higher than the band gap energy of the material. When the excited light is absorbed by material, electrons in the valence band would get the energy to jump into the conduction band then relatively produce a hole in the valence band. When an excited electron in an excited state returns to initial state, to comply with the energy conservation law, it will emit a photo whose energy is equal to the energy difference between the excited state and the initial state. In this section, the extend topics related to PL will be introduced which include temperature dependent PL, micro-PL (μ-PL)

and TRPL. The detailed description of optical mechanism will be also reported in this section.

2-5-1 Temperature dependent PL

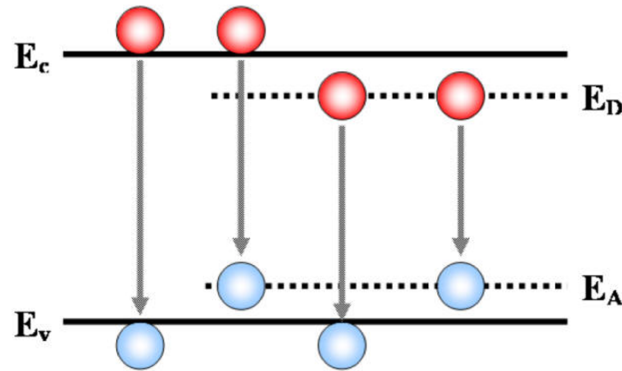

Fig. 2-8 Radiative recombination transitions in semiconductor materials.

If there are some defect energy level existed in energy band gap of semiconductor, they also could contribute to radiative recombination process. Therefore we could observe the multiple emission peaks in the PL spectra, and the intensity of the emission peaks is related to the contribution of the individual radiative recombination process. In general, there are four possible radiative recombination transitions in semiconductor (shown in Fig. 2-8). By analyzing the spectra of material, we can direct inspect the purity of material.

On the other hand, temperature dependent PL is a useful method to extract the thermal activation energy of optical transition. The temperature dependent PL intensity is general expressed as:

$$I(T) = \frac{I(0)}{1 + A\exp(\frac{-E_A}{kT}) + B\exp(\frac{-E_B}{kT}) + ...} \qquad (2\text{-}2)$$

where A, B is the coefficient related to defect density, and E_A, E_B is the activation energy. The activation energy is the physical value that means the

transition energy barrier from radiative recombination to nonradiative reocombination, which can represent the exciton binding energy, localized energy, band offset of QW, energy difference between defect energy level to conduction band or valence band and …etc.

By plotting the Arrhenius plot for PL intensity, we can extract the activation energy to analyze the origin of radiative recombination. Moreover, temperature dependent emission energy and FWHM is also used to analyze the exciton localization effect in InGaN.

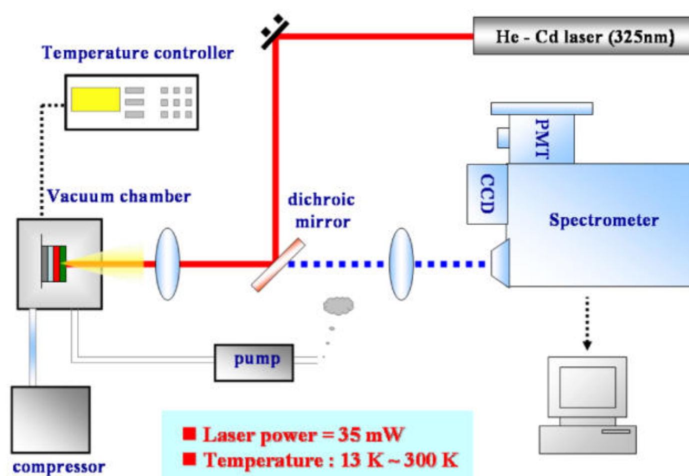

Fig. 2-9 Schematic of temperature-dependent PL setup.

The setup of our PL system is shown in Fig. 2-9. The pumping light source was a multi-mode and non-polarized Helium-Cadmium laser operated on 325 nm with 20 mW. After reflected by three mirrors, the laser light was focus by a lens which focal length was 5cm, to 0.1mm in diameter and the luminescence signal was collected by the same lens. The sample can be placed in a isolated chamber for temperature-dependent PL measurement. The cooling system is Helium compressor and the temperature is controlled by a temperature controller. The probed light was dispersed by 0.32 monochromator (Jobin-Yvon Triax-320) equipped with 1800, 1200, and 300 grooves/mm

grating and which maximum width of the entrance slits was 1mm. The resolution was controlled in 1nm by selecting 300 grooves/mm grating and slit of 0.1mm. We use long pass filter to avoid the laser coupling with the PL spectrum.

2-5-2 μ-PL

Due to the progress of epitaxy technology and the understanding of quantum mechanics, low - dimension nanostructure such as nanorod, QDs has attracted much attention. Therefore, the measuring tool to probe such noanostructure is necessary. In general, the focused laser spot size of PL system is about 100 μm, it is not small enough to probe the properties of individual nanostructure such as nanorod or QDs, therefore, the μ - PL system has been developed. The μ - PL system uses optical objective to replace optical lens to focus laser light, with the minimum laser spot of 1 μm. By this system we can observe the optical properties of nanostructure, obtain higher excitation power density and scan the emission pattern of sample.

Fig. 2-10 shows the setup of μ - PL system. The sample is excited by a He - Cd laser operating on 325 nm with 40 mW. First the beam of laser light is expanded by beam expander, and then focused into a spot with 1 μm in diameter on sample by 15x objective. The PL is collected in a fiber with 100 μm in the diameter and detected by a photo multiplier tube (PMT) or charge coupled display (CCD). Furthermore, μ - PL spectra is dispersed by a 320 nm monochromator (Jobin – Yvon Triax 320). The wavelength resolution is about 1 nm by using 300 grooves/mm grating and the slit of 0.1 mm. And position of sample can be controlled by piezo stage PZT to scan the luminescence image of sample.

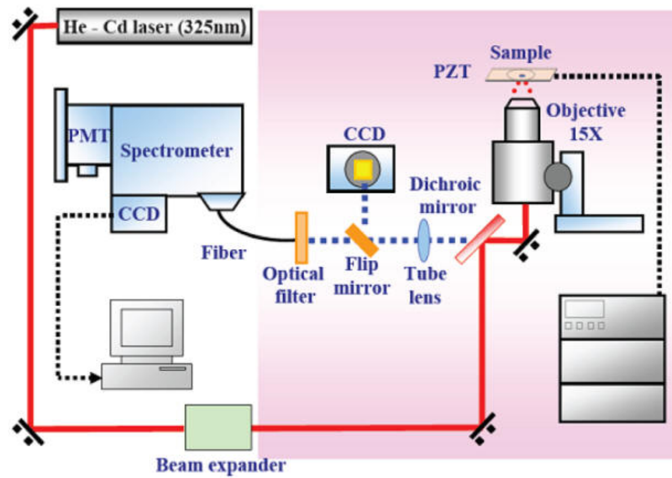

Fig. 2-10 Schematic of μ - PL system.

2-5-3 Time-resolved PL

TRPL is an indispensable technique to study the dynamical process of photoexcited carriers such as relaxation, radiative, nonradiative, and localization processes. The transient luminescence intensity obtained by the data of TRPL is generally expressed by the following equation as a function of time after excitation:

$$I(t) = I(0)\exp(-\frac{t}{\tau}) \tag{2-3}$$

where τ is the effective carrier lifetime, and can be extracted by fitting the experimental data by above equation. Moreover, the effective carrier lifetime can be expressed as below:

$$\frac{1}{\tau} = \frac{1}{\tau_r} + \frac{1}{\tau_{nr}} + \frac{1}{\tau_{trans}} \tag{2-4}$$

where τ_r, τ_{nr}, and τ_{trans} are the radiative recombination lifetime, nonradiative reocombination lifetime, and transfer time toward lower - lying energy levels. If radiative recombination occurs at the bottom of energy levels, the term of the transfer time can be neglected so that the equation is simplified as shown below:

$$\frac{1}{\tau(T)} = \frac{1}{\tau_r(T)} + \frac{1}{\tau_{nr}(T)} \tag{2-5}$$

On the other hand, the internal quantum efficiency can be written in terms of τ_r and τ_{nr}, where

$$\eta_{int}(T) = \frac{\tau_{nr}(T)}{\tau_r(T) + \tau_{nr}(T)} \tag{2-6}$$

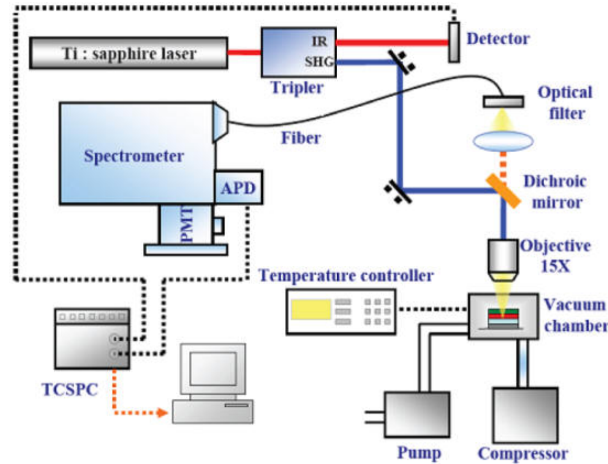

Fig. 2-11 Schematic of TRPL system.

Therefore, if we perform temperature dependent PL, and assume the internal quantum efficiency at the lowest temperature equals to 1, by equation 2-4 and 2-5 we can extract the radiative lifetime and nonradiative lifetime as a function of temperature. And by analyzing the relation between radiative lifetime and temperature, the dimensionality of nanostructure can be characterized.

Fig. 2-11 shows the experimental setup of the temperature dependent TRPL. Pulsed photo - excitation for the TRPL is provided by the frequency doubled (2w) or frequency tripled (3w) beams of a mode-locked Ti : sapphire laser (w) which is pumped by Ar+ laser. The wavelength of Ti : sapphire laser can be tuned from 700 nm to 1100 nm, the pulse width is 200 fs. The repetition rate of the laser is 76 MHz whose time interval is 12.5 ns. To direct examine

the optical properties of InGaN/GaN MQW LEDs and avoid the absorption of GaN film, the pumping light source was a frequency doubled Ti : sapphire laser operated on 385 nm with 2 mW. The luminescence decay was measured with time correlated single photon counting (TCSPC) system in conjunction with monochromator using gratings whose grooves are 2400 grooves/mm. Time-resolution for the detection is about 4 ps. For temperature dependent experiment, the samples were mounted in a closed - cycle He cryostate, pump was used to draw out air in cryostate to obtain high vacuum (~ 10^{-3} torr), and temperature controller controlled the temperature from 15 K to 300 K.

2-6 Electroluminescence, EL

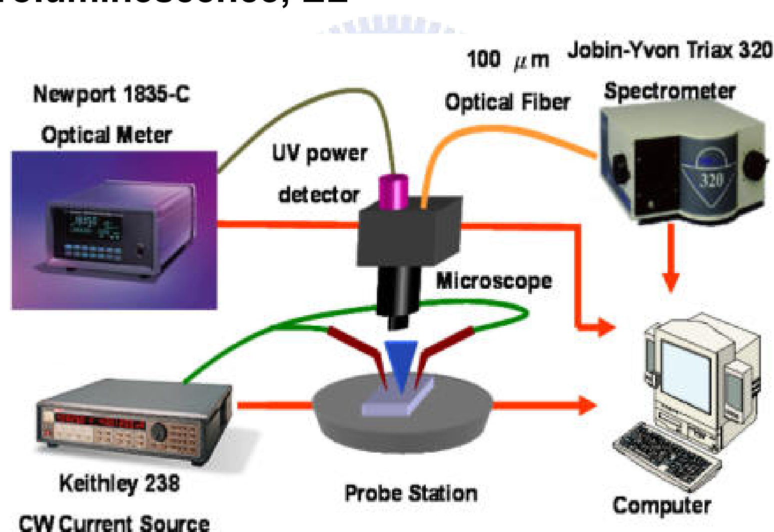

Fig. 2-12 EL system includes all components.

The discovery of electroluminescence (EL) made it possible to convert electric energy directly into light energy. It is the result of recombination of carriers generated by injecting electrons. The quality of EL relies on crystal quality, the selection of the doping agent and the level of dopant concentration.

In order to precisely device performance of LEDs, such as LIV curve, EL

spectrum, or near field pattern, the EL setup is built for our sample test on wafer level or packaged level. Probe station is a basic instrument to match our needs and illustrated in Fig. 2-12, which include probe station, current source, and power-meter module. Keithley 238 can provide precisely continuous current with laser diode and measure relative voltage in parallel. Newport power meter module (model 1835C) with photodiode and power meter can detect the light output power of our samples. An integration sphere was used to collect emitting power from our samples and to improve the accuracy of power measurement. The samples were placed on a platform of the probe station and injected bias current with microprobe. Threshold condition, slope efficiency, turn-on voltage and differential resistance can be obtained from L-I-V information by adjusting bias current. At the same time, near-field pattern was obtained by specific CCD. Emission spectrum of the device was measured by optical spectrum analyzer (OSA, Advantest 8381). A multi-mode fiber probe was placed close to the emission aperture to take optical spectra. The OSA had spectrum resolution of 0.1nm which was adequate to measure LEDs spectra.

2-7 Furnace

Fig. 2-13 shows the picture and schematic of the furnace with two-zone temperature controllers. And there are two kinds of gases provision. One is Nitrogen and the other is Oxygen. Attached to the end of the tube is a mechanical pump, which can exert itself to exhaust the air inside the quartz tube to the extent of 0.01 Torr. In my experiments, we use this furnace to anneal our samples and carry out some experiments related to quality improvement study.

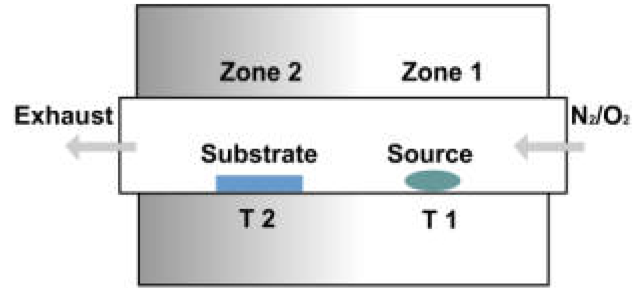

Fig. 2-13 Two-zone furnace picture and schematic figure.

Reference

[1] S. Nakamura, M. Senoh, N. Iwasa, S. Nagahama, Jpn. J. Appl. Phys. 34, L797 (1995).

[2] S. Nakamura, M. Senoh, S. Nagahama, N. Iwasa, T. Yamada, T. Matsushita, H. Kiyoku, Y. Sugimoto, Appl. Phys. Lett., 68, 2105 (1996).

[3] S. Nakamura and G. Fasol, "The Blue Laser Diode", 1997 (Berlin: Springer).

[4] S. J. Bass, J. Crystal Growth, 44, 29 (1978).

[5] H. Manasevit, Appl. Phys. Lett., 12, 156 (1968).

[6] http://www.veeco.com/

[7] http://www.aixtron.com/index.php?id=1&L=1

[8] O. Ambacher, J. Smart, J. R. Shealy, N. G. Weimann, K. Chu, M. Murphy, W. J. Schaff, L. F. Eastman, R., Dimitrov, L. Wittmer, M. Stutzmann, W. Rieger, and J. Hilsenbeck, J. Appl. Phys., 85, 3222 (1999).

[9] L. De Broglie, Nature, 112, 540 (1923).

[10] H. Seiler, J. Appl. Phys., 54, R1 (1983).

[11] G. Binnig, H. Rohrer, Ch. Gerber, E. Weibel, Phys. Rev. Lett., 49, 57 (1982)

[12] G. Binnig, C. F. Quate, Ch. Gerber, Phys. Rev. Lett., 56, 930 (1986).

[13] A. W. Hull, J. Am. Chem. Soc, 41, 1168, (1919).

Chapter 3 Development and optimization of a-plane GaN growth on r-plane sapphire

GaN-based semiconductors and their heterostructures have recently attracted considerable interest due to their potential for visible or ultraviolet LEDs [1], LDs [2] and high–power transistors [3] grown on either c-plane (0001) sapphire, SiC, or free standing GaN substrates. Unfortunately, epitaxy toward the [0001] orientation leads to undesirable spontaneous and piezoelectric polarization effects, which would result in inclined bands and significantly reduce the carrier recombination rate in quantum wells grown on such polar substrates. [4, 5] To eliminate such polarization effects, growth along non-polar orientations has been explored for $(1\bar{1}00)$ *m*-plane GaN on *m*-plane SiC and (100) $LiAlO_2$ substrates, and $(11\bar{2}0)$ *a*-plane GaN on $(1\bar{1}02)$ *r*-plane sapphire [6~8]. In this chapter, we will report the optimum growth of a-plane GaN grown on r-plane sapphire and investigate the influence of important growth parameters on crystal quality and surface morphology of a-plane GaN.

3-1 Difficulties to grown nonpolar GaN

Growth of non-polar group-III nitride hexagonal heterostructures could overcome the presence of large built-in electrostatic fields to further improve the quantum efficiency of light emitting diodes. However, the surface morphology of the GaN grown on r-plane sapphire was usually quite rough, making device fabrication more difficult. As a result, most groups avoided using r-plane sapphire substrates to grow GaN devices. In order to overcome the influence of defects generated due to the lattice mismatch, Chitnis *et al.* grown *a*-plane LED structure on r-plane sapphire by using a GaN layer with a

thickness of more than 30 μm [9]. Haskell *et al.* employed ELOG [10]. Although ELOG method could yield *a*-plane GaN films over *r*-plane sapphire with significantly improved surface morphologies and with reduced dislocation densities, this approach was complicated and consumed much of time.

In this study, the optimal growth condition of the *a*-plane GaN layers with pits-free and smooth surface were investigated by modifying growth temperatures, pressures, and V/III ratio. Furthermore, the influences of different thickness of AlN as nucleation layers were also considered. Eventually, we obtained a high quality *a*-plane GaN bulk with a smooth surface capable of fabricating device structures, such as multiple quantum wells and LEDs directly on top of it.

3-2 Experimental procedure

The experiments were carried out in the low-pressure MOCVD system. We used low-temperature AlN as nucleation layers instead of traditional GaN layers. The nucleation layer growth temperature and thickness were 600 ^{o}C and 30 nm, respectively. The V/III ratio for the nucleation layer is 13800. In order to obtain suitable growth conditions for *a*-plane GaN films, influence of different pressures (100, 200, and 300 torr) and temperatures (1020, 1070 and 1120 ^{o}C) on growth of 2 μm thick GaN bulks was studied. TMGa, TMAl and ammonia were used as Ga, Al and N sources, respectively. Then, we fixed the growth pressure and temperature, for which would result in the smoothest surface morphology, and changed different thickness of AlN nucleation layers from 30 nm to 15 and 45 nm. In addition, the V/III ratio for growth of the GaN bulk was adjusted from 900 to 600 and 1200, subsequently. The surface morphologies of all samples were characterized by optical microscopy (OM)

with x magnification, SEM and AFM. Surface step profiles were evaluated using the surface profiler (Veeco Dektak 6M). The crystalline quality was analyzed by high-resolution reciprocal space mapping (RSM) by using XRD around the (11$\underline{2}$0) reflection.

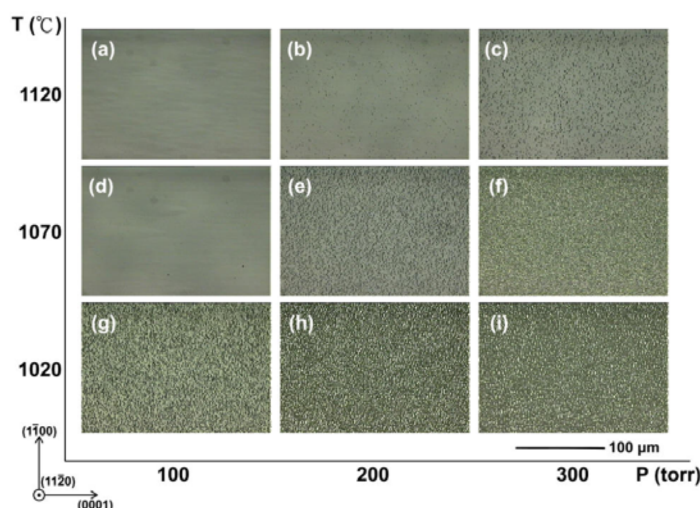

Fig. 3-1 OM images of a-plane GaN surfaces for growth temperatures of 1020~1120 ^{o}C and pressures of 100~300 torr.

3-3 Effects of different growth temperatures and pressures

First, the optimal growth parameters in growth pressure and temperature to obtain a good surface morphology of an *a*-plane GaN bulk were studied. The thickness of the AlN nucleation layer and the V/III ratio for growing *a*-plane GaN bulk were fixed as 30 nm and 900, respectively. In order to make all analysis easy to understand, our results and growth parameters were set into a three by three square chart. Fig. 3-1 shows the typical OM images of *a*-plane GaN with different growth conditions. We found the nucleation island did not coalesce fully causing the surface rugged and rough when the growth pressures were high and temperatures were low, such as shown in Fig. 3-1 (f),

(h) and (i). Once the growth temperature was elevated and the pressure was decreased, the nucleation islands gradually coalesced with each other and remained pits distributed on the sample surface as shown in Fig. 3-1 (b)~ (e) and (g). Fig. 3-1(a) manifested smoothest surface morphology without any observable pits when the growth temperature and pressure were set as 1120 ^{o}C and 100 torr, respectively.

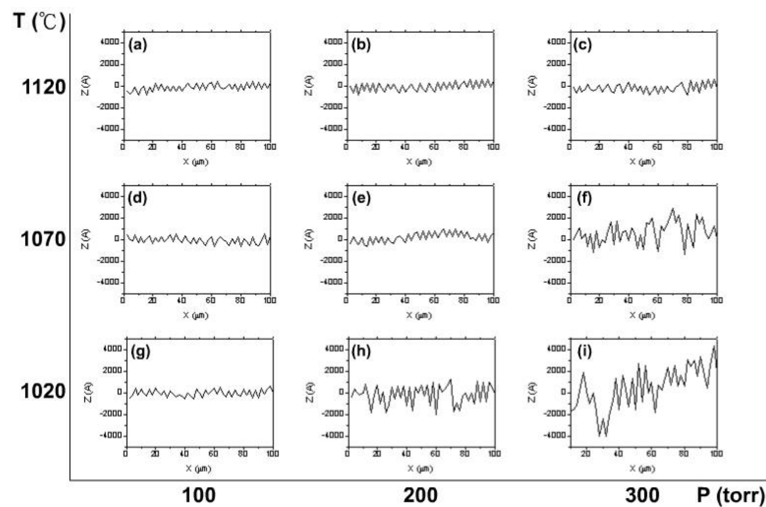

Fig. 3-2 Surface profiles of *a*-plane GaN epi-layers for growth temperatures of 1020~1120 ^{o}C and pressures of 100~300 torr. X is the scan direction along $[1\underline{1}00]$, and Z is the height direction along $[11\underline{2}0]$.

The surface profiles of *a*-plane GaN were roughly estimated for different growth conditions by the surface profiler. These results of line profiles along the direction perpendicular to [0001] were shown in Fig. 3-2. Fig. 3-2 (a)~(e) and (g) revealed that the rough surfaces of these sample with peak to valley (PV) values of around 70 nm, whereas Fig. 3-2 (f), (g) and (h) showed worse PV values from 200 to 600 nm. These results can be compared with other study by Kusakabe *et al.*, who grew *a*-plane GaN in regular growth conditions and obtained a high PV value around 0.8 μm [11], indicating that the surface

profiles were successfully improved an order of magnitude by elevating the growth temperature and diminishing the growth pressure.

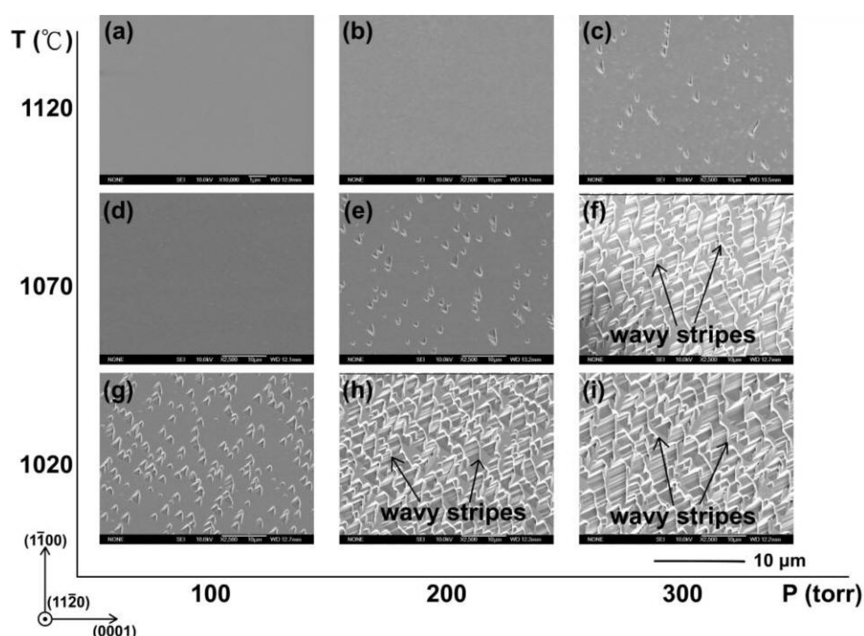

Fig. 3-3 SEM images of a-plane GaN surfaces for growth temperatures of 1020~1120 ^{o}C and pressures of 100~300 torr.

The surface morphology images investigated by SEM were enlarged as shown in Fig. 3-3. The growth condition of high temperature and low pressure resulted in the best surface morphology in terms of flatness as shown in Fig. 3-3 (a). However, not only large number of pits existed but also wavy stripes formed along *c*-axis could be clearly observed in Fig. 3-3 (f), (h) and (i). The possible reason of strip formed was due to the faster growth rate along *c*-direction than *m*-direction. On the other hand, the irregular strips could not be observed in Fig. 3-3 (b)~(e) and (g) except for triangle pits on the surface. In general, the common feature of V defects is characteristically observed when the *c*-plane GaN grown in the kinetically limited condition [12]. The V defect for a *c*-plane GaN is an inverted pyramid bound by the pyramidal {10$\underline{1}$1}

facets. Since the V defect only appears it's half side in an *a*-plane GaN under the non-polar growth scheme, such kind of pits was named a triangle pit originating from upon the island growth and coalescing at the initial growth of the high temperature GaN bulk [13].

As a result, we could suggest that the growth mechanism of *a*-plane GaN at the beginning stage followed a Volmer-Weber (VW) mode which would lead to the three dimension (3D) growth. Each GaN column was probably grown from a GaN island formed on top of AlN nucleation layer. After most of the islands merged to each other, a Frank-van der Merwe (F-vdM) mode occurred and dominated the subsequent growth process, leading to two dimensional (2D) growth. Since a stable [0001] sublayer would be preferred in contrast to the $[1\underline{1}00]$ one due to the different atomic bonding process between Ga and N atoms in two directions [14], the overall growth rate in the [0001] direction should be higher than that in the $[1\underline{1}00]$ direction, resulting in a growth front with wavy strips. The 2D growth condition is necessary for thick *a*-plane GaN since the difference of growth rate could occur between *c*-axis and *m*-axis. Otherwise, the 3D growth would result in the appearances of triangle pit and wavy strips.

3-4 Roles of V/ III ratio and nucleation layer

In addition to the effect of epitaxial temperature and pressure, the thickness of the nucleation layer and the V/III ratio for growth of the *a*-plane GaN bulk were also considered. The growth pressure and temperature were fixed to the same values as those resulting in the best surface morphology. Then, the thickness of the nucleation layer and the V/III ratio were modified. The thickness of nucleation layer was adjusted from 30 nm to 15 and 45 nm.

And the V/III ratio was adjusted from 900 to 600 and 1200. The surface morphologies of all samples were observed by AFM and the results were shown in Fig. 3-4. The center 3D AFM image is the result of the sample grown at 1120 ^{o}C and at 100 torr, which shown submicro pits and additional stripe features along the [0001] direction. Meanwhile, the sample showed very smooth surface with a root mean square (RMS) roughness of only 10.5 Å. Such roughness was far less than the previous report by Ni *et al.*, whose sample was grown at lower growth temperature on a thicker nucleation layer [15]. However, when we used AlN nucleation layers with thickness thinner and thicker than 30 nm, the surface morphologies would get worse along with many pits with size around 100 nm. Owing to the fact that each GaN column could be grown from GaN nucleus formed on top of each columnar AlN region, the columns of AlN should have optimal disordered orientations for GaN growth. Once the thickness of AlN nucleation layer has been changed, it could cause the variation of disordered orientations and degrade the surface morphology. On the other hand, the surface morphology got worse when the V/III ratio was increased or decreased from 900. The high V/III ratio leaded to high NH_3 flow and further produced more amounts of Hydrogen during the growth process. Some pits distributed on the surface under the high V/III ratio could be due to the excess Hydrogen facilitating the surface dissociation rate and damaging the surface morphology [16]. Although the low V/III ratio condition benefits the 2D growth, some Ga atoms would not react with insufficient N atoms causing a wavy surface. To sum up above discussions, we suggested both the thickness of nucleation layer and the V/III ratio have optimal values to grow an *a*-plane GaN bulk.

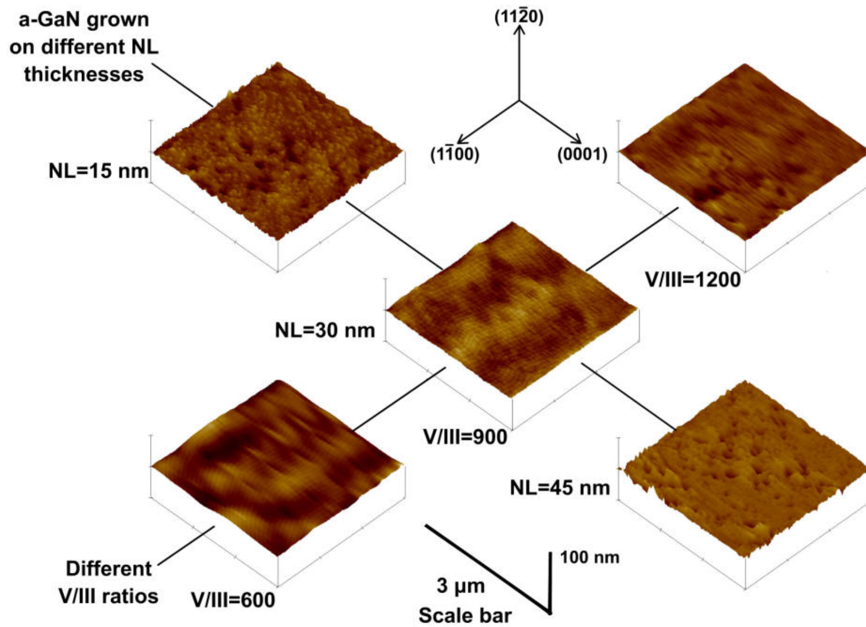

Fig. 3-4 AFM images of a-plane GaN surfaces for growth of V/III ratio of 600~1200 and on different thickness of nucleation layer.

X-ray RSMs were recorded around the (11$\underline{2}$0) reflection in a coplanar geometry, as shown in Fig. 5. The unit of "r.l.u." refers to dimensionless reciprocal lattice units. The vertical axis in Fig. 3-5 (a) corresponds to the ω-scan around the symmetry (11$\underline{2}$0) reflection, and the full width of height maximum (FWHM) was about 875 arcsec after conversion of the coordinate, demonstrating that the sample grown at high temperature and low pressure could prompt a good quality GaN film. It is worth noticing that the narrow FWHM of 665 arcsec in ω-scan of Fig. 3-5 (e) under the lower temperature and higher pressure conditions was obtained, although the sample grown by this condition showed several pits in OM and SEM images. This indicates that a more coherent growth condition resulting in a narrower FWHM ofω-scan did not promise a good surface morphology, which could be due to the different in-plane strains and growth rates along *c* and *m*-directions. On the other hand, the larger contoured areas shown in Fig. 3-5 (f), (h) and (i) indicated the

inferior crystal quality due to disordered GaN columns during the growth. As a result, the surface morphology and the crystal quality should be carefully compromised in the growth of *a*-plane GaN films.

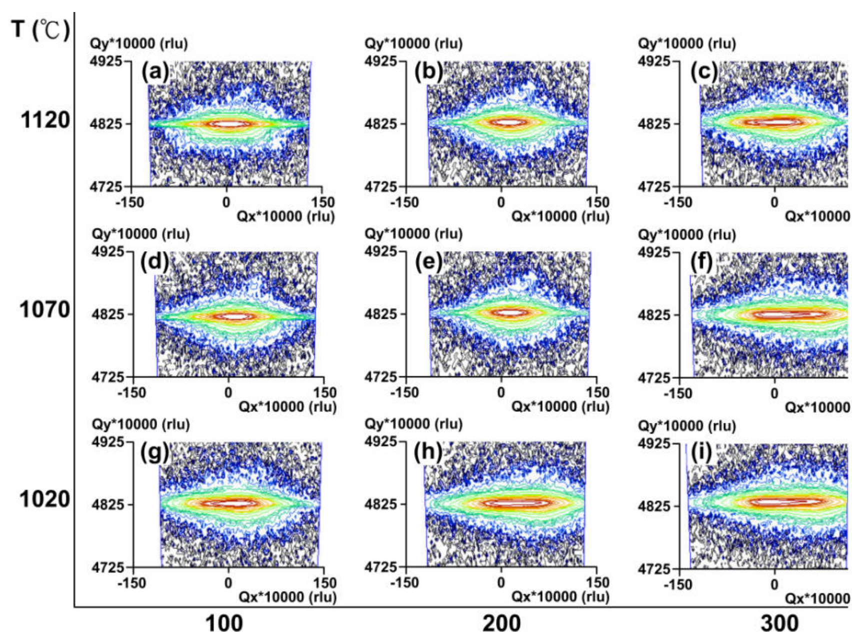

Fig. 3-5 Reciprocal space mapping of *a*-plane GaN for growth temperatures of 1020~1120 ^{o}C and pressures of 100~300 torr.

3-5 Observation of threading dislocation in nonpolar GaN

In order to realize the extended defects in the GaN epilayer, cross-sectional transmission electron microscopy was employed. Fig. 3-6 shows cross-sectional TEM image along [1$\bar{1}$00] zone axis of the GaN epilayer grown under optimal condition, and two beam diffraction contrast bright and dark field images with g vector [11$\bar{2}$0] (as shown in Fig. 3-6 (a-b)). According g*b dark field analysis, most of threading dislocations in the GaN films in contrast in both of g = [11$\bar{2}$0] and [0002] dark field images and hence should be mixed a+c type dislocations. In our TEM observation, we could calculated the dislocation density to be around 1.85×10^{10} /cm^{2}. Remarkably, although the

high dislocation density in the GaN can be observed in our case, the surface of the GaN epilayer was still very smooth. Thus, the threading dislocation might not be directly responsible to rough or pit surface of a-plane GaN grown under other non-optimal condition.

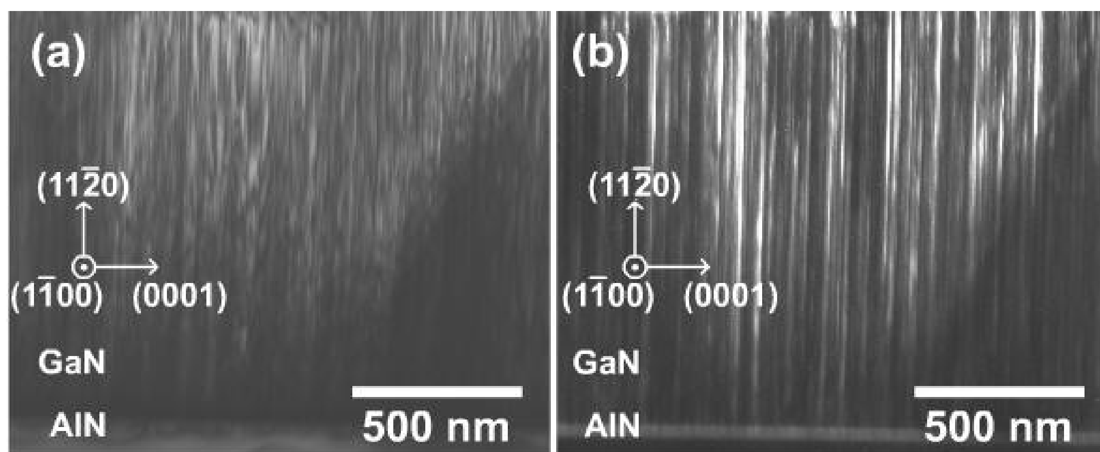

Fig. 3-6 Bright field (a) and dark field (b) cross-section TEM images of GaN epilayer grown under optimal condition with g vector [11$\underline{2}$0].

3-6 Summary

In conclusion, we grew *a*-plane GaN with a series of growth conditions included different growth temperatures and the chamber pressures by MOCVD. High quality and smooth surface *a*-plane GaN could be obtained at the high temperature and low pressure growth condition. The best mean roughness of the surface morphology was 10.5 Å. Moreover, the thickness of the nucleation layer and V/III ratio for the GaN bulk growth existed optimal values for obtaining high quality *a*-plane GaN. In our TEM observation, we could calculate the dislocation density to be around 1.85×10^{10} /cm^2. The result of smooth surface confirmed the feasibility of fabricating non-polar devices on a-plane GaN grown in such growth condition. Finally, the smooth surface of the *a*-plane GaN film obtained in this study demonstrated the feasibility and

convenience of fabricating non-polar devices.

Reference

[1] S. J. Pearton, J. C. Zolper, R. J. Shul, F. Ren, J. Appl. Phys., 86, 1 (1999).

[2] S. Nakamura and G. Fasol, in *The Blue Laser Diodes* (Springer, Heidelberg, 1997).

[3] T. Palacios, L. Shen, S. Keller, A. Chakraborty, S. Heikman, S. P. DenBaars, U. K. Mishra, J. Liberis, O. Kiprijanovic, A. Matulionis, Appl. Phys. Lett., 89, 073508 (2006).

[4] T. Deguchi, K. Sekiguchi, A. Nakamura, T. Sota, R. Matsuo, S. Chichibu, S. Nakamura, J. Acoust. Soc. Jpn. (E), 38, L914 (1999).

[5] S. Ghosh, P. Waltereit, O. Brandt, H. T. Grahn, K. H. Ploog, Phys. Rev. B 65, 075202 (2002).

[6] K. Domen, K. Horino, A. Kuramata, T. Tanahashi, Appl. Phys. Lett. 71, 1996 (1997).

[7] P. Waltereit, O. Brandt, A. Trampert, H. T. Grahn, J. Menniger, M. Ramsteiner, M. Reiche, K. H. Ploog, Nature, 406, 865 (2002).

[8] A. Chitnis, C. Chen, V. Adivarahan, M. Shatalov, E. Kuokstic, V. Mandavilli, J. Yang, M. A. Khan, Appl. Phys. Lett., 84,3663 (2004).

[9] A. Chitnis, C. Chen, V. Adivarahan, M. Shatalov, E. Kuokstis, V. Mandavilli, J. Yang, M. A. Khan, Appl. Phys. Lett., 84, 3663 (2004).

[10] B. A. Haskell, T. J. Baker, M. B. McLaurin, F. Wu, P. T. Fini, S. P. DenBaars, J. S. Speck, S. Nakamura, Appl. Phys. Lett., 86, 11917 (2005).

[11] Kazuhide Kusakabe, Kazuhiro Ohkawa, Jpn. J. Appl. Phys. 44, No11, 7931 (2005).

[12] X. Wu, C. Elsass, A. Abare, M. Mack, S. Keller, P. Petroff, S. DenBaars, J. Speck, S. Rosner, Appl. Phys. Lett., 72, 692 (1998).

[13] F. Wu, M. D. Craven, S. H. Lim, J. S. Speck, J. Appl. Phys., 94, 942

(2003).

[14] H. Wang, C. Chen, Z. Gong, J. Zhang, M. Gaevski, M. Su, J. Yang, M. A. Khan, Appl. Phys. Lett., 84, 499 (2004).

[15] X. Ni, Y. Fu, Y. T. Moon, N.Biyikli, H. Morkoç, J. Cryst. Growth, 290, 166 (2006).

[16] T. H. Myers, B. L. VanMil, J. J. Holbert, C. Y. Peng, C. D. Stinespring, J. Alam, J. A. Freitas Jr., V. A. Dmitriev, A. Pechnikov, Y. Shapovalova, V. Ivantsov, J. Cryst. Growth, 246, 244 (2002).

Chapter 4 Understanding nonpolar GaN growth

Since the demonstration of the two-step growth with low-temperature buffer layers [1, 2], organometallic vapor phase epitaxy (OMVPE) of *c*-plane Ga-face GaN has quickly matured to commercial success. GaN growth on nonpolar or semipolar planes, though intensely pursued worldwide along a similar course, has not advanced as far in addressing issues of island nucleation [3-5], morphological imperfections (surface striation [3-7] and pits [7-10]), and microstructural defects (basal plane stacking faults, or BSFs) [5, 11, 12]. There is clearly a need to understand the heteroepitaxy process of nonpolar GaN at a mesoscopic scale beyond semi-empirical methodology if the challenges described above will ever be overcome.

4-1 Wulff-plot and motivation

The presence of specific facets during growth of crystalline materials under equilibrium conditions is a manifestation of the principle of minimization of total surface energy. The shape of a growing crystal can be derived from a polar plot of surface energy (the Wulff plot, or γ-plot) [13, 14]. The same procedure has been extended to non-equilibrium growth conditions with the *kinetic* Wulff plot, or *v*-plot (in which surface energy is replaced by growth velocity) [15-17]. The kinetic Wulff plot can be considered an intrinsic and concise fingerprint of surface kinetics that manifests itself over the micrometer through nanometer length scales in thin-film morphology [18-20], shape evolution of selective area growth (SAG) mesas [21-27], nucleation dynamics in heteroepitaxy [3-5], and the shape of nanostructures and quantum dots [28, 29]. We believe that an accurate and comprehensive knowledge of kinetic

Wulff plots may initiate a crucial step toward a model-based approach to nucleation, growth evolution, and island coalescence of nonpolar GaN. In this paper we report the mapping of growth velocity as a function of crystallographic orientation (i.e., polar *v*-plot, or kinetic Wulff plot) from GaN mesas grown on nonpolar surfaces under various OMVPE conditions. Equipped with a detailed knowledge of the orientational dependence of growth kinetics based on the *v*-plots, we provide an analysis on some complex phenomena encountered in nonpolar GaN growth, such as island nucleation, morphological striation, and pit formation, and to demonstrate a broad validity of incorporating the *v*-plots into mesoscopic growth dynamics.

4-2 Experimental procedure

A-plane GaN (*a*-GaN) and *m*-plane GaN (*m*-GaN) epilayers were grown in a horizontal OMVPE reactor using high-temperature AlN buffer layers on *r*-plane sapphire (*r*-Al_2O_3) and *m*-plane 4H SiC (*m*-SiC) substrates, respectively. Details of the individual growth conditions have been reported elsewhere [3]. After the deposition of 0.1 μm SiO_2 on as-grown nonpolar GaN templates, standard photolithography and F-based reactive ion etch was used to define circular openings (fill factor ~0.3). Initial SAG was done for a period of 20 minutes to form GaN mesas, followed by the first set of imaging analysis. Then the samples were reloaded into the reactor for a regrowth and subsequent measurements to obtain the differential advances of individual facets. Three different OMVPE conditions [A: 1070 ^oC, 100 mbar, 1 slm (slm denotes standard liters per minute) NH_3; B: 1070 ^oC, 100 mbar, 4 slm NH_3; and C: 1030 ^oC, 300 mbar, 1 slm NH_3] were used for the regrowths on SAG mesas. The SAG mesas before and after regrowths were examined by SEM (FEI

XL30 field-emission microscope).

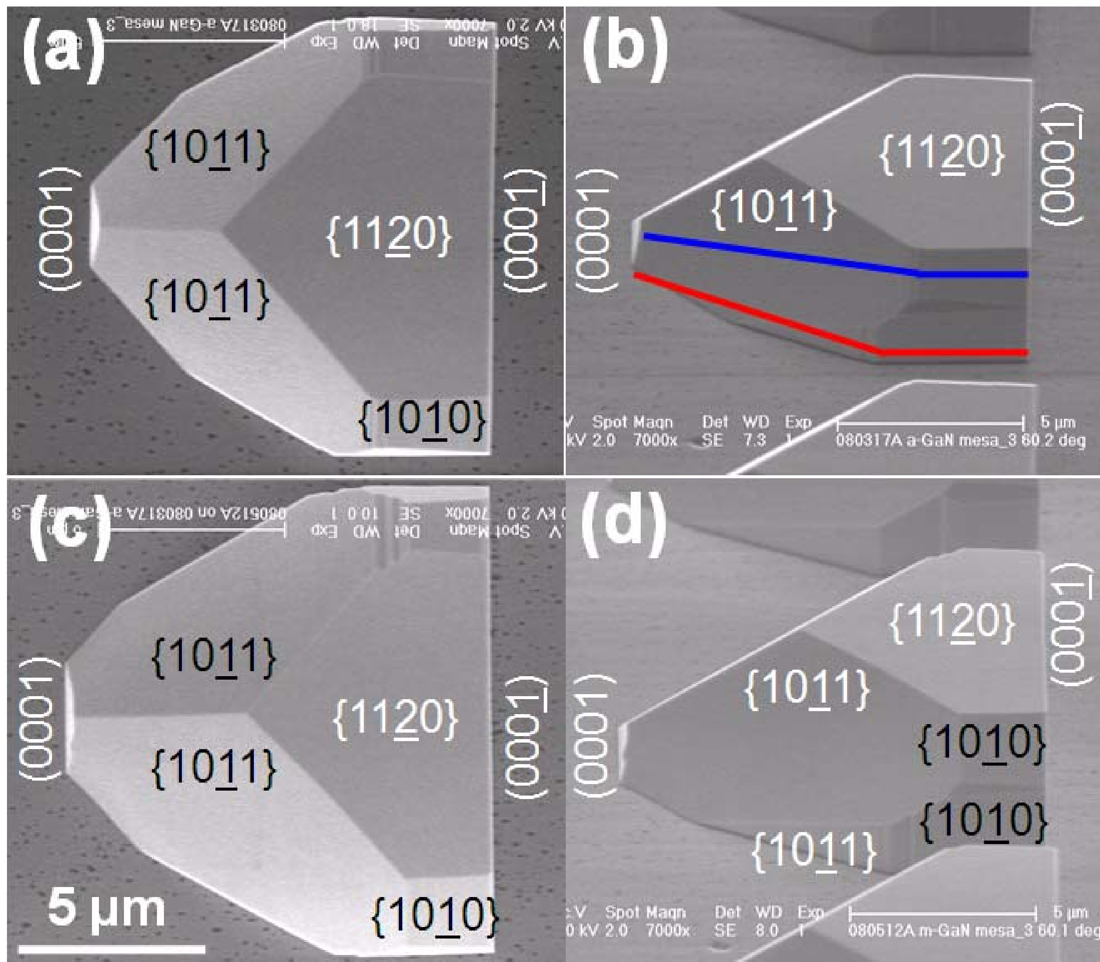

Fig. 4-1 [(a) and (c)] SEM top views and [(b) and (d)] perspective views (60° inclined from *a*-axis to the in-plane *m*-axis) of the same *a*-GaN SAG mesa [(a) and (b)] before and [(c) and (d)] after a 10-min regrowth under condition A. The 5 μm scale bar applies to all the figures.

Fig. 4-1 shows two sets of SEM images of an *a*-GaN SAG mesa before [Fig. 1(a) and 1(b)] and after [Fig. 4-1 (c) and 1(d)] a 10-min regrowth. The individual SAG mesa was imaged from both the top and two orthogonal axes 60º inclined from the top so that the details of every facet were revealed. Coordinate marking was employed during SEM observation to ensure that exactly the same SAG mesa was imaged before and after the regrowth. The

pits on the SiO_2 mask also provide convenient positional reference; the advance of individual facets could be determined to an accuracy within 0.01 μm. Comparing Fig. 1(a) and 1(c), we note that $(000\bar{1})$ N-face barely advances while a significant lateral growth of (0001) Ga-face was observed. The regrowth also caused a decrease of the top $\{11\bar{2}0\}$ area [Figs. 1(a) and 1(c)] and an increase of the $\{10\bar{1}1\}$ area as the mesa became taller [Fig. 1(b) and 1(d)]. Growth velocity was thus defined by the *differential advance* normal to a facet during the regrowth. The differential method helps to bypass complications in inhomogeneous nucleation and imperfection in lithography [30], minimize the ambiguity in extracting growth velocity (from mask edge versus centroid, and the influence of the opening contour) [31, 32], and facilitate the capture of transient fast-growing planes. The measured growth velocities of the observed low-index planes are summarized in kinetic Wulff plots as cusp points [14, 17]. Appropriate trigonometric interpolations are used to connect the cusps [17].

4-3 Forming facet of nonpolar GaN island

An example of a two-dimensional (2D) Wulff plot of prism planes mapped onto the basal plane is shown in Fig. 4-2 (a). An advantage of the kinetic Wulff plot representation is the rendering of the relative incorporation kinetics over a wide angular range. An unexpected feature immediately coming to view is that the growth velocities of equivalent planes do not exhibit 6-fold symmetry. The *a*- and *m*-planes adjacent to the SiO_2 mask have much reduced velocities compared with their own equivalent planes that are farther away from the mask surface, which was also observed in other group's SAG study [27]. Planes that intersect the SiO_2 mask at steeper angles have in general slower

growth rates; so the lateral expansion (along the in-plane *m*-axis) of the SAG mesa is suppressed, a phenomenon analogous to non-wetting or beading in surface science. The presence of a heterogeneous surface (e.g., SiO_2 mask) around SAG mesas has an unexpected effect of “deforming” the Wulff plot. The interaction of the overgrown wings with the underlying mask can be seen through the well-known wing tilt in the SAG or epitaxial lateral overgrowth (ELO) of Si, GaN, and GaAs [33-36].

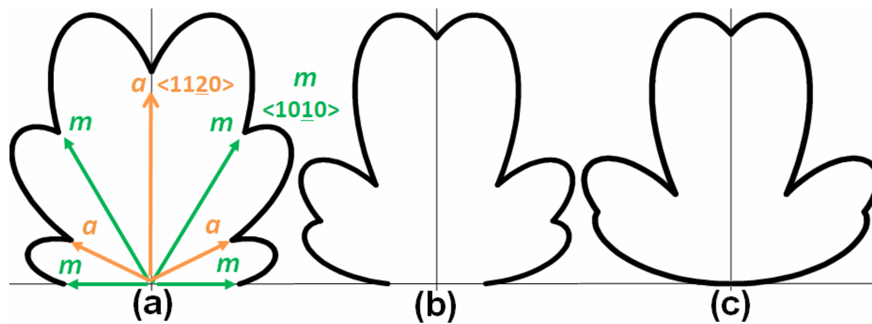

Fig. 4-2 Kinetic Wulff plots of prism planes mapped onto the basal plane for growth conditions (a) A, (b) B, and (c) C. The region below the horizontal axis corresponds to the SiO_2 mask.

The lateral expansion of *a*-GaN mesas is suppressed by the heterogeneous surface (e.g., SiO_2 mask) not only along the *m*-axis but also other directions, such as $\langle 10\bar{1}1\rangle$ and $[000\bar{1}]$. Fig. 4-3 are the kinetic Wulff plots mapped onto *a*-planes, constructed with four cusps corresponding to (0001) Ga-face, $\{10\bar{1}1\}$ pyramidal plane, $\{10\bar{1}0\}$ *m*-plane, and $(000\bar{1})$ N-face. The two colored traces of Wulff plots correspond to two sets of facets; the first set are in contact with the mask surface (inner red trace) and the second comprise the equivalent facets 60º rotated around *c*-axis (outer blue trace), as labeled in Fig. 4-1 (b). The inner red trace, with growth velocities reduced by at least a factor of two, can be considered as characteristic of heteroepitaxial nucleation

applicable to nonpolar island formation on foreign substrates (*r*-Al_2O_3 and *a*-/*m*-SiC, even with AlN buffers). The outer blue trace is more representative of the growth under homoepitaxy. We note that a very similar trend was also observed in the kinetic Wulff plots for *m*-GaN SAG mesas (not shown).

4-4 Wulff-plot of nonpolar GaN under different growth conditions

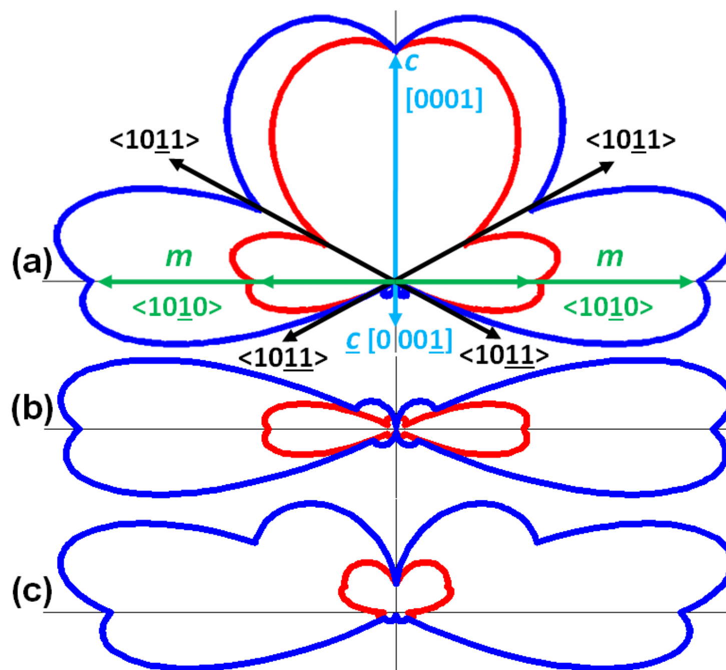

Fig. 4-3 Kinetic Wulff plots of the orientations mapped onto *a*-planes for growth conditions (a) A, (b) B, and (c) C. The inner red trace represents the facets that are in contact with the mask and the outer blue trace the equivalent facets that are 60º rotated around *c*-axis (the two sets of facets are marked by blue and red lines in Fig. 1(b)). The traces below the horizontal axes, especially the position of the {1011} cusps, are hypothetical.

A salient feature in Fig. 4-3 (for all the three conditions A, B and C) is the near-zero growth velocity of N-face (0001) and its dominant presence,

suggesting a very low surface energy. We note that such a stagnant advance of N-face only occurs in nonplanar growth in the presence of neighboring facets (e.g., *m*- and *a*-planes); however, planar growths of N-face GaN with mass-transport-limited growth rates (0.7~3 μm/hr) under similar conditions are routinely observed [37]. The very slow lateral growth of N-face promotes islanding in the initial growth stage of nonpolar GaN and has been linked to the generation of BSFs [5]. Since the planar growth of N-face GaN is essentially free of BSFs [37], the BSFs observed in the SAG N-face wings of nonpolar GaN patterned with stripes normal to *c*-axis are likely induced by the interaction of N-face sidewalls with the mask. During nonpolar GaN heteroepitaxy on foreign substrates [11], the formation of BSFs at the heterogeneous interface can conceivably contribute to strain relaxation in the lateral growth of N-face sidewalls [38]. A procedure for the reduction of BSFs based on this model will be reported elsewhere [39].

As a result of the suppressed lateral growth toward various directions (including the in-plane $<10\bar{1}0>$, $<10\bar{1}1>$, and $[000\bar{1}]$), the *a*-GaN mesas surrounded by the mask tend to grow vertically. In the heteroepitaxy case of nonpolar GaN planar growth, the surface of foreign substrates (sapphire and SiC, even with AlN buffer) appear heterogeneous to GaN, promoting the formation of 3-dimensional (3D) nucleation islands [3, 4], and affects the incorporation of Ga adatoms into various facets. From growth condition A to B and C [V/III ratio increases, temperature (*T*) decreases, and reactor pressure (*P*) increases], the growth velocity *a*/*m* ratio significantly increases [Fig. 4-2 (b) and 4-2 (c)], and the Wulff plots mapped onto *a*-planes become very anisotropic [Fig. 4-3 (b) and 4-3 (c)], giving elongated slate-like islands. The formation and development of *a*-GaN islands on *a*-AlN/*r*-Al_2O_3 normally lead to

a very rough surface, as monitored by the quick decay of the *in situ* optical reflectance during the *a*-GaN initial growth (Fig. 4-4).

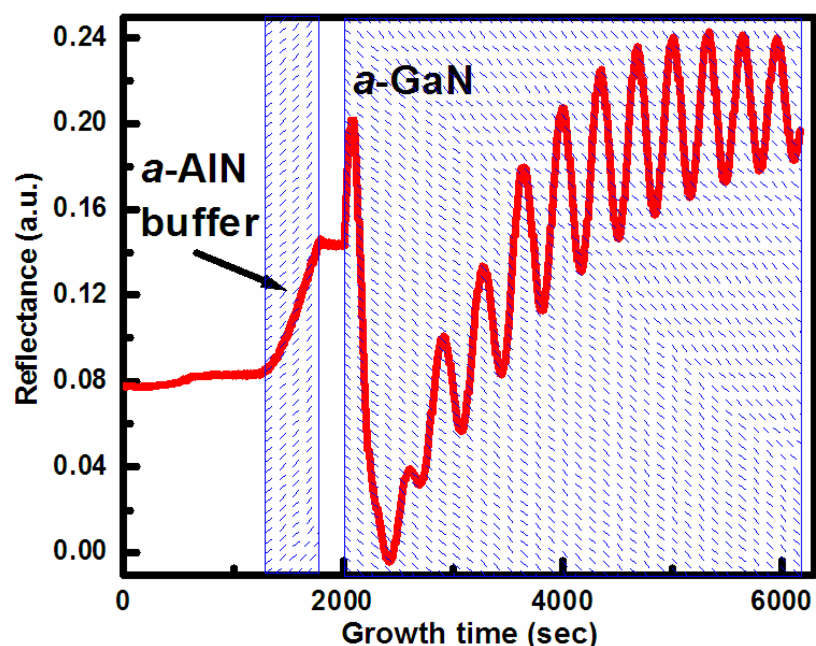

Fig. 4-4 *In situ* optical reflectance of *a*-GaN growth on *r*-Al_2O_3 with a HT-AlN buffer. The growths of *a*-AlN buffer and *a*-GaN are marked out by shaded blue area.

Knowledge from the kinetic Wulff plots can also help understand the morphology of nonpolar GaN epilayers. Our previous study has recognized that the coalescence of *m*-GaN islands along *c*-axis [a vertical *concave* growth process created by the vertical (000$\underline{1}$) of one island and the {10$\underline{1}$1} of its neighbor [3], as shown in Fig. 4-5 (a)] greatly contributes to surface striation along the *a*-axis [Fig. 4-5 (b)], especially when the coalescing islands have different height. A high density of surface striation is observed on *m*-GaN/SiC grown under a V/III ratio, a high *P* and a low *T* [40]. Such growth conditions produce *m*-GaN islands with a high aspect ratio (elongated along the in-plane *a*-axis) according to the very anisotropic Wulff plots generated from *m*-GaN

SAG study [not shown, but similar to Figs. 4-3 (b) and 4-3 (c)]. The coalescence of such slate-like *m*-GaN islands along the *c*-axis results in a very pronounced striated morphology. The same argument can be extended to *m*-GaN/$LiAlO_2$ (100) with striation along the *a*-axis [6]. A notable exception to our current model is *a*-GaN/*r*-Al_2O_3 with striation along the *c*-axis [4, 7]. The huge anisotropy in in-plane strains due to the anisotropic lattice mismatch (16% and 1.3% for *m*- and *c*-axes, respectively) may induce a substantial modification to surface incorporation kinetics and the shape of kinetic Wulff plots for *a*-GaN growth on *r*-Al_2O_3, resulting in striation along the *c*-axis.

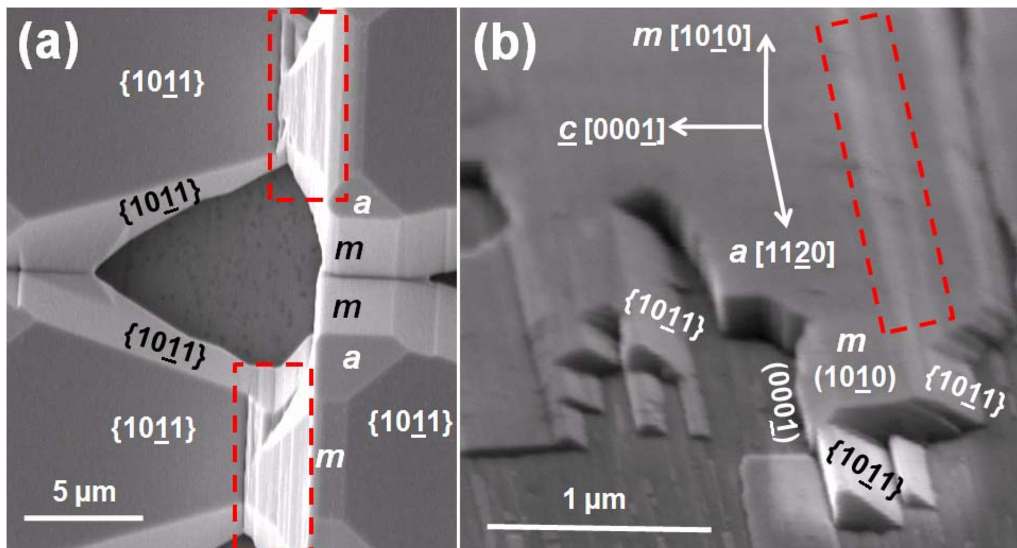

Fig. 4-5 SEM (a) top view of *m*-GaN SAG mesas coalescing along *c*-axis; (b) perspective view of *m*-GaN nucleation islands on AlN/*m*-SiC. The coalescence between inclined $\{10\underline{1}1\}$ and vertical $(000\underline{1})$ (marked by red dash lines) greatly contributes to the striation along *a*-axis.

4-5 Reasons for pit generation in nonpolar GaN

Surface pits are another class of morphological defects frequently encountered in *a*-GaN/*r*-Al_2O_3 growth [Fig. 4-6 (c)] [7-10]. Faceted pits are in general due to incomplete island coalescence where the fill-up process is

characterized by *concave* growth. Mask openings with an annular-ring pattern were employed to elucidate the coalescence dynamics with a *concave* surface contour. Interestingly, the pentagon-like center void [Fig. 4-6 (a)] resulting from an inward lateral growth from the annular-ring opening strongly resembles the shape of *a*-GaN surface pits [Fig. 4-6 (c)], including a nearly identical angle (~135°) of the arrowheads formed by the intersection lines of $\{10\underline{12}\}$ with *a*-plane. Contrary to the previous designation that the *a*-GaN pits are bound by $\{10\underline{1}1\}$ and $(000\underline{1})$ facets [10], our detailed SEM imaging analysis indicates that the main defining planes for the pits are $\{10\underline{12}\}$, $\{20\underline{2}1\}$ and $\{11\underline{2}2\}$ [Fig. 4-6 (a) and 4-6 (b)] which are also observed from the coalescence of adjacent *a*-GaN SAG mesas (not shown). Our indexing is consistent with the principle of *concave* growth, i.e., *fast-growing planes* (in this case $\{10\underline{12}\}$, $\{20\underline{2}1\}$ and $\{11\underline{2}2\}$) should appear and slow-growing planes [$(000\underline{1})$ and $\{10\underline{1}1\}$] become extinct [7, 23]. The pentagon-like void along <0001> reflects a different nature of $\{10\underline{12}\}$ and $\{11\underline{2}2\}$ planes. $\{10\underline{12}\}$ planes possess components of *m*-plane and *N-face* while $\{11\underline{2}2\}$ represent a hybrid of *a*-plane and *Ga-face*. A systematic investigation is underway to correlate the atomic configuration with the incorporation kinetics. As the concave growth proceeds, the pentagon-like pits can gradually evolve into triangular ones. The evolution (appearance or diminishment) of the surface pits depends on the relative growth velocities among $\{10\underline{12}\}$, $\{20\underline{2}1\}$, $\{11\underline{2}2\}$ and the top $(11\underline{2}0)$. Here the growth velocity of the inclined $\{10\underline{1}1\}$ is used to benchmark the lower bounds of those fast-growing planes [17]. The ratio of growth velocities between $\{10\underline{1}1\}$ and $(11\underline{2}0)$ varies as 0.42, 0.066 and 0.24 for conditions A, B and C, respectively (from Fig. 4-2 and 4-3). Conditions like A (high *T*, low *P*, and low V/III) would therefore facilitate the “fill-up” of surface pits, in very good agreement with the

reported results [7-9]. From the view of growth evolution, the high density of surface pits formed during the *a*-GaN island coalescence can be gradually filled up under a optimum condition, and the *in situ* reflectance slowly recovers to a higher average with good oscillations (Fig. 4-4). In contrast, very little recovery is observed in the decayed reflectance under conditions such as B or C.

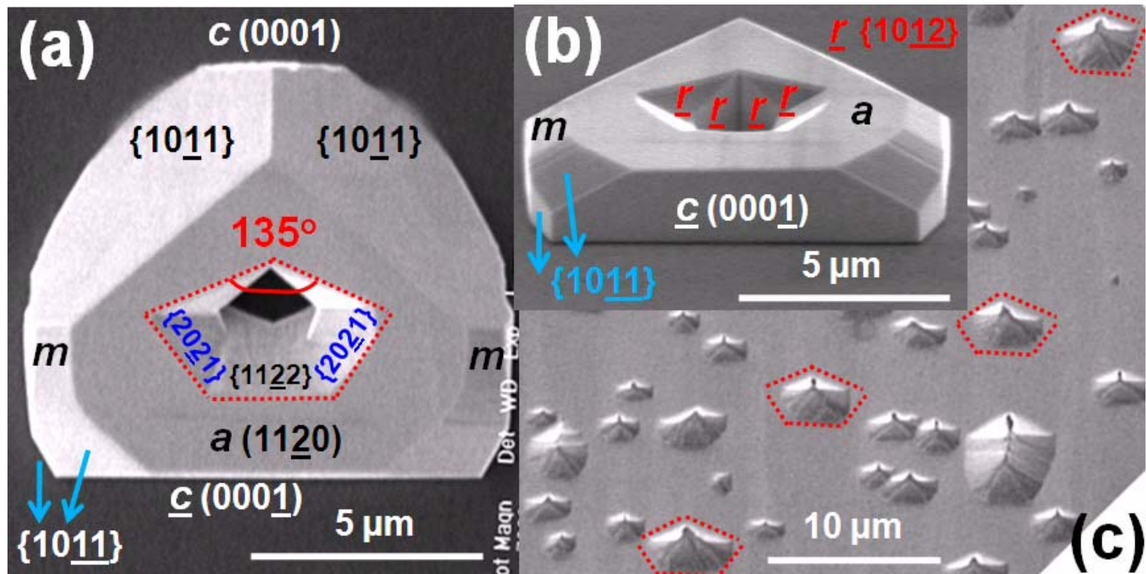

Fig. 4-6 SEM (a) top view and (b) perspective view (60° inclined from *a*-axis to [0001]) of the same *a*-GaN SAG mesa; (c) SEM top view of planar *a*-GaN/*r*-Al_2O_3 surface with many pits resembling the concave void in the SAG mesa, marked out by the red dot lines.

Finally, it is worth mentioning that pits are rarely observed on *m*-GaN surface [3, 6], because the difference in growth velocity between *m*-plane and those fast-growing planes is much smaller than that between *a*-plane and those fast-growing planes. Figure 4-7 shows an *a*-GaN and an *m*-GaN SAG concave mesa grown out of the same annular openings in the same run under condition C. The *m*-GaN mesa is a lot shorter than the *a*-GaN mesa because *m*-axis growth velocity is much smaller than *a*-axis [Fig. 4-3 (c)]. The concave

void in the *m*-GaN mesa [Fig. 4-7 (b)] almost grows out extinction, while the void in the *a*-GaN mesa [Fig. 4-7 (a)] remains much larger and more pronounced. A series of regrowths on *a*-GaN concave mesas are needed to capture the transients of those high-index, fast-growing planes and to further refine the 3D kinetic Wulff plots with more *saddle* points [17].

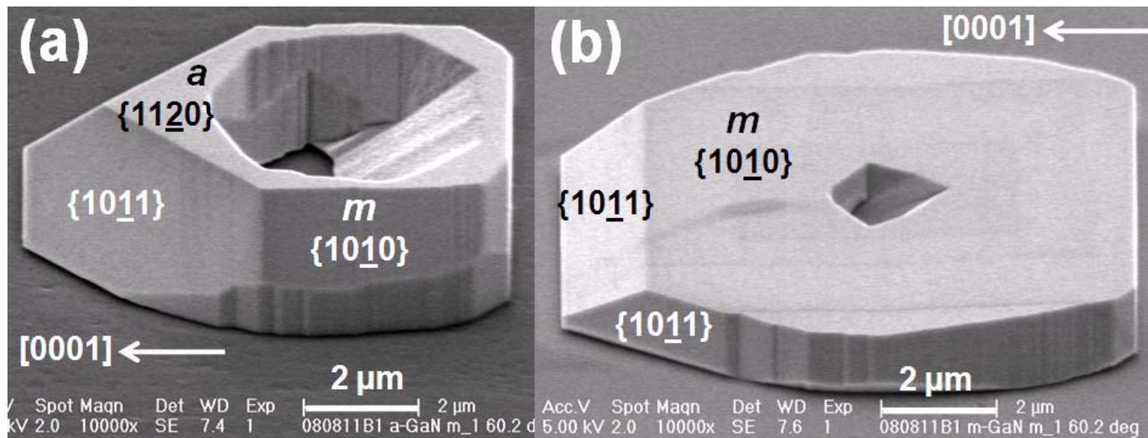

Fig. 4-7 SEM perspective views of (a) a-GaN and (b) m-GaN SAG concave mesas grown out of the same annular openings in one OMVPE run under condition C. The both images are 60° inclined from the growth axis to the in-plane nonpolar axis.

4-6 Summary

In conclusion, we present a quantitative mapping of the kinetic Wulff plots toward the understanding of GaN growth on nonpolar and possibly semi-polar planes. We believe that a precise knowledge and a detailed understanding of kinetic Wulff plots will enable model-based growth of device-quality GaN in a predictive way. Insights from the kinetic Wulff plots were used to explain some complex phenomena in nonpolar GaN growth, including island formation, striation, and surface pits.

Reference

[1] H. Amano, N. Sawaki, I. Akasaki, and Y. Toyoda, Appl. Phys. Lett. 48, 353(1986).

[2] S. Nakamura, Jpn. J. Appl. Phys. 30, L1705 (1991).

[3] Q. Sun, S.-Y. Kwon, Z. Ren, J. Han, T. Onuma, S. F. Chichibu, and S. Wang, Appl. Phys. Lett. 92, 051112 (2008).

[4] T. Aschenbrenner, K. Goepel, C. Kruse, S. Figge, and D. Hommel, Phys. Stat. Sol. (c) 5, 1836 (2008).

[5] M. D. Craven, F. Wu, A. Chakraborty, B. Imer, U. K. Mishra, S. P. DenBaars, and J. S. Speck, Appl. Phys. Lett. 84, 1281 (2004).

[6] O. Brandt, Y. J. Sun, L. Däweritz, and K. H. Ploog, Phys. Rev. B 69, 165326 (2004).

[7] X. Ni, Y. Fu, Y. T. Moon, N. Biyikli, and H. Morkoç, J. Cryst. Growth 290, 166 (2006).

[8] M. Araki, N. Mochimizo, K. Hoshino, and K. Tadatomo, Jpn. J. Appl. Phys., Part 1 46, 555 (2007).

[9] T. S. Ko, T. C. Wang, R. C. Gao, H. G. Chen, G. S. Huang, T. C. Lu, H. C. Kuo, and S. C. Wang, J. Cryst. Growth 300, 308 (2007).

[10] F. Wu, M. D. Craven, S. -H. Lim, and J. S. Speck, J. Appl. Phys. 94, 942 (2003).

[11] B. A. Haskell, F. Wu, M. D. Craven, s. Matsuda, P. T. Fini, T. Fujii, K. Fujito, S. P. DenBaars, J. S. Speck, and S. Nakamura, Appl. Phys. Lett. 83, 644 (2003); B. A. Haskell, T. J. Baker, M. B. McLaurin, F. Wu, P. T. Fini, S. P. DenBaars, J. S. Speck, and S. Nakamura, *ibid* 86, 111917 (2005).

[12] T. Kawashima, T. Nagai, D. Iida, A. Miura, Y. Okadome, Y. Tsuchiya, M.

Iwaya, S. Kamiyama, H. Amano, and I. Akasaki, Phys. Stat. Sol. (b) 244, 1848 (2007).

[13] G. Wulff, Z. Krystallogr. Min. 34, 449 (1901).

[14] C. Herring, Phys. Rev. 82, 87 (1951).

[15] F. C. Frank, *Growth and Perfection of Crystals* (Wiley, New York, 1958).

[16] S. Osher and B. Merriman, Asian J. Math. 1, 560 (1997).

[17] D. Du, D. J. Srolovitz, M. E. Coltrin, and C. C. Mitchell, Phys. Rev. Lett. 95, 155503 (2005).

[18] J. Nishizawa, J. Cryst. Growth 56, 273 (1982).

[19] J. Nishizawa and M. Kimura, J. Cryst. Growth 74, 331 (1986).

[20] T. Shibata, K. Asai, Y. Nakamura, M. Tanaka, K. Kaigawa, J. Shibata, and H. Sakai, J. Cryst. Growth 229, 63 (2001).

[21] J. Nishizawa and M. Shimbo, J. Cryst. Growth 24-25, 215 (1974).

[22] H. Asai, J. Cryst. Growth 80, 425 (1987).

[23] S. H. Jones, L. K. Seidel, K. M. Lau, and M. Harold, J. Crystal Growth 108, 73 (1991).

[24] E. Gil-Lafon, J. Napierala, D. Castelluci, A. Pimpinelli, R. Cadoret, and B. Gerard, J. Cryst. Growth 222, 482 (2001).

[25] K. Hiramatsu, K. Nishiyama, A. Motogaito, H. Miyake, Y. Iyechika and T. Maeda, Phys. Stat. Sol. (a) 176, 535 (1999).

[26] K. Hiramatsu, K. Nishiyama, M. Onishi, H. Mizutani, M. Narukawa, A. Motogaito, H. Miyake, Y. Iyechika, and T. Maeda, J. Cryst. Growth 221, 316 (2000).

[27] B. Imer, F. Wu, M. D. Craven, J. S. Speck, and S. P. DenBaars, Jpn. J. Appl. Phys., Part 1 45, 8644 (2006).

[28] V. Jindal, N. Tripathi, M. Tungare, O. Paschos, P. Haldar, and F.

Shahedipour-Sandvik, Phys. Stat. Sol. (c) 5, 1709 (2008).

[29] S. Founta, C. Bougerol, H. Mariette, B. Daudin, and P. Vennegues, J. Appl. Phys. 102, 074304 (2007).

[30] M. Jetter, V. Perez-Solorzano, A. Groening, M. Ubl, H. Graebeldinger, and H. Schweizer, J. Crystal Growth 272, 204 (2004).

[31] B. Beaumont, S. Haffouz, and P. Gibart, Appl. Phys. Lett., 72, 921 (1998).

[32] T. M. Katona, J. S. Speck, and S. P. DenBaars, Appl. Phys. Lett. 81, 3558 (2002).

[33] H. Raidt, R. Kohler, F. Banhart, B. Jenichen, A. Gutjahr, M. Konuma, I. Silier, and E. Bauser, J. Appl. Phys. 80, 4101 (1996).

[34] P. Fini, H. Marchand, J. P. Ibbetson, S. P. DenBaars, U. K. Mishra, and J. S. Speck, J. Cryst. Growth 209, 581 (2000).

[35] Z. R. Zytkiewicz, Thin Solid Films 412, 64 (2002).

[36] J. Z. Domagala, A. Czyzak, and Z. R. Zytkiewicz, Appl. Phys. Lett. 90, 241904 (2007).

[37] Q. Sun, Y. S. Cho, I.-H. Lee, J. Han, B. H. Kong, and H. K. Cho, Appl. Phys. Lett. 93, 131912 (2008).

[38] D. M. Hwang, S. A. Schwarz, T. S. Ravi, R. Bhat, and C. Y. Chen, Phys. Rev. Lett. 66, 739 (1991).

[39] Y. S. Cho, Q. Sun, I.-H. Lee, T.-S. Ko, C. D. Yerino, J. Han, B. H. Kong, H. K. Cho, and S. Wang, Appl. Phys. Lett. 93, 111904 (2008).

[40] Q. Sun, C. D. Yerino, Y. S. Cho, T.-S. Ko, I.-H. Lee, and J. Han, Appl. Phys. Lett. 93, 111904 (2008).

Chapter 5 Improvement of crystal quality in nonpolar GaN

Nonpolar *a*-plane GaN base material grown on *r*-plane sapphire substrates which always accompany with a wavy, stripe-like growth feature possess a large density of TDs and SFs [1, 2]. These unavoidable defects not only form undesirable nonradiative centers but also bring difficulty and challenge to grow high quality a-plane GaN. The different crystal orientation between c- and m- axis leads to the asymmetrical degree of lattice mismatch which also cause in-plane biaxial strain [3]. Therefore, to improve crystal quality of a-plane GaN is pretty urgent and important for further nonpolar developments either material growth or device fabrication. In this chapter, we will also propose several more useful and convenient methods and demonstrate their capability and possibility. These approaches were expected to be contributable for current developments in nonpolar III-nitride field. The methods we present including TELOG and the use of InGaN/GaN SLs. These two methods are effective to reduce much defects density generated in a-plane GaN structure grown on r-plane sapphire.

5-1 Methods to reduce defects of nonpolar GaN

Recently, successful ELOG of a-plane GaN on r-plane sapphire has been reported [4]. ELOG not only improves significantly the material quality by reducing the density of TDs but also alleviates the strain-related surface roughening and faceting. Despite the ELOG assisted morphology and quality improvements in a-plane GaN over r-plane sapphire, the study of the epilayer quality and dislocations distribution in the ELOG epilayer is quite not lucid.

Despite the ELOG assisted morphology and quality improvements in a-plane GaN over r-plane sapphire, the coalescence thickness, usually more than 20 μm, is quiet thick and difficult to control the uniformity. Herein, we improve a-plane GaN quality by using epitaxial lateral overgrowth on trenched a-plane GaN buffer layers. The TELOG allowed us to obtain a-plane GaN with low dislocation density, simple fabrication process, lower cost, and thinner coalescence thickness in comparisons to the previous reports.

In addition to use TELOG technique, another possible method for reducing TD density is the insertion of strain-layer SLs into the epitaxial layer. The stain due to different lattice constants in the SLs, can deflect the TDs into the interfacial plane, had been analyzed by Matthews and Blakeslee theoretically [5]. The dislocation line runs parallel to the growth direction is bowed as a result of the coherent strain present in the SLs. Subsequently, the dislocations move laterally and eliminate with another dislocation of the opposite Burgers vector, combine with the dislocation of different Burgers vector to form a third one, or even run to the edge of the wafer. Ultimately, the dislocation density reduction is achieved by the insertion of SLs. The detail experiments and results will be discussed and described in following sections.

5-2 Experimental procedure

5-2-1 Trench epitaxial lateral overgrowth technique (TELOG)

Fig. 5-1 shows the flow chart to grow the TELOG a-plane GaN. First, the a-plane GaN templates with 1.5 μm thickness were grown by low pressure MOCVD on r-plane sapphire substrates using conventional two-step growth technique. Then, a 2 μm-seed / 18 μm-trench TELOG stripe pattern was applied parallel to the direction to realize vertical c-plane sidewalls followed by

etching of SiO_2 using inductively coupled plasma etching through the windows to the GaN epitaxial film. GaN stripes were etched through the mask openings, down to the r-plane sapphire substrate by reactive ion etching. To simplify the growth process, the SiO_2 mask was removed by hydrofluoric acid followed by depositing a-plane GaN TELOG film using a single-step growth process. In this study, the growth temperature, pressure, and V/III ratio were 1190 ^{o}C, 100-150 mbar and 700-800, respectively.

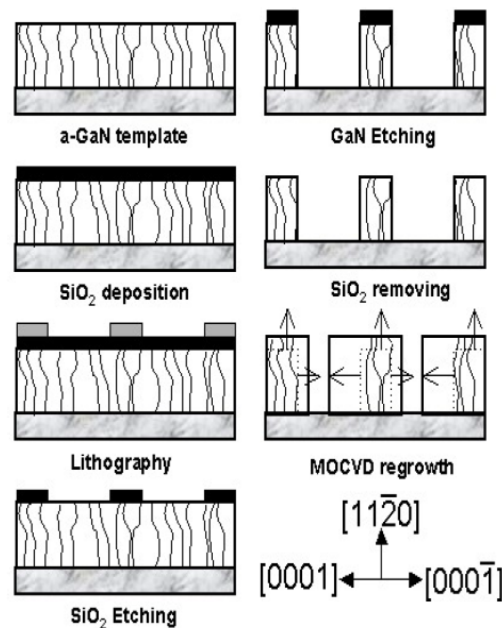

Fig. 5-1 Flow chart of a-plane GaN TELOG process.

5-2-2 The use of InGaN/GaN superlattices

First, a low temperature GaN nucleation layer was grown by low pressure MOCVD on r-plane sapphire substrates, followed by the growth of 0.5-μm-thick high temperature GaN. Then, a SL comprising 20 pairs of 5-nm-thick $In_{0.2}Ga_{0.8}N$ and 5-nm-thick GaN were inserted in a-plane GaN layer. A 10 pairs MQWs consisted of 6-nm-thick wells and 15-nm-thick barriers were grown at temperature of 827 ^{o}C. The as-grown samples of using both

techniques were investigated by TEM for the microstructure of a-plane GaN thin film. Temperature-dependent μ-PL measurements were carried out using the 325 nm line of a CW He–Cd laser with a spot size of 10 μm over the temperature range 90-300 K.

5-3 Growth behavior of nonpolar GaN using TELOG

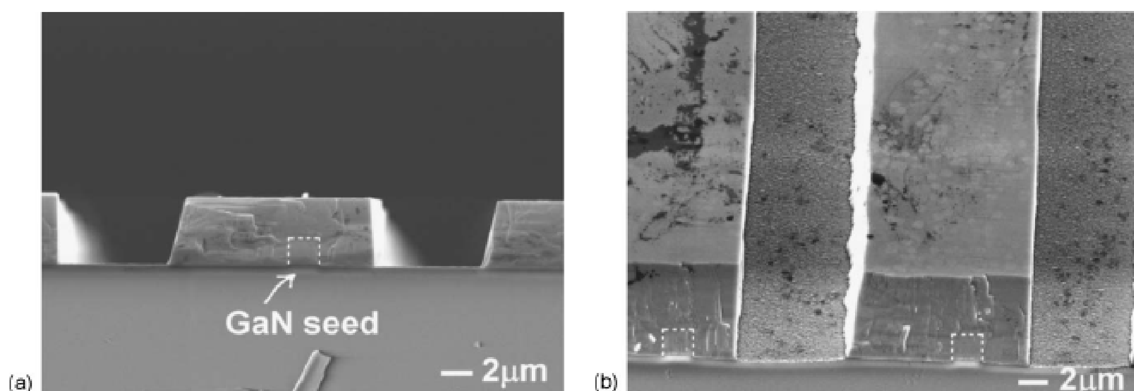

Fig. 5-2 Cross-sectional SEM of the un-coalesced TELOG a-plane GaN film with 2 μm seed /18 μm trench pattern.

To observe the growth mechanism for TELOG method, we stopped the process before the coalescence of the GaN films. The SEM images of cross-sectional and birds-view TELOG GaN by MOCVD were shown in Fig. 5-2 (a). The growth rate of the Ga-face wing was twice faster than the N-face wing. However, the ratio of growth rate in Ga-face wing to N-face wing was not as high as an order of magnitude reported by Imer *et al.* [6]. A thin GaN layer about 0.2 μm grown on the bottom of the trenches, as shown in Fig. 5-2 (b), could be the reason to hinder the lateral growth rate in the Ga-face wing and hence affect the epitaxial quality.

The distributions and types of dislocations were investigated by cross-sectional TEM shown in Fig. 5-3 (a) and (b). According to the g = (0002)

and g = (11$\underline{2}$0) two beam bright field images, most of the TDs are obvious in both of the g = (11$\underline{2}$0) and (0002) two beam conditions, indicating that these dislocations are mixed a + c type dislocations. The TDD of stripped GaN seed in region 2 was more than 1×10^{10} cm^{-2}. TDD of Ga-face GaN wing in region 4 was about 9×10^{9} cm^{-2} and TDD of N-face GaN wing in region 1 was about 3×10^{7} cm^{-2}, three orders of magnitude lower than planar films. Because the lateral growth mode could be affected when the laterally grown layers encounters the underlying GaN layers, we suggest that the crystal quality of Ga-face GaN with a higher growth rate could be easily affected by the thin a-GaN layer grown on the bottom of the un-coalesced windows. Due to the relatively low growth rate of the thin a-GaN layer on the bottom of the trench, the crystal quality of the Ga-face GaN wing at the beginning of the lateral growth was good while the thin a-GaN layer was not formed, resulting in a low dislocation and high PL intensity area of region 3.

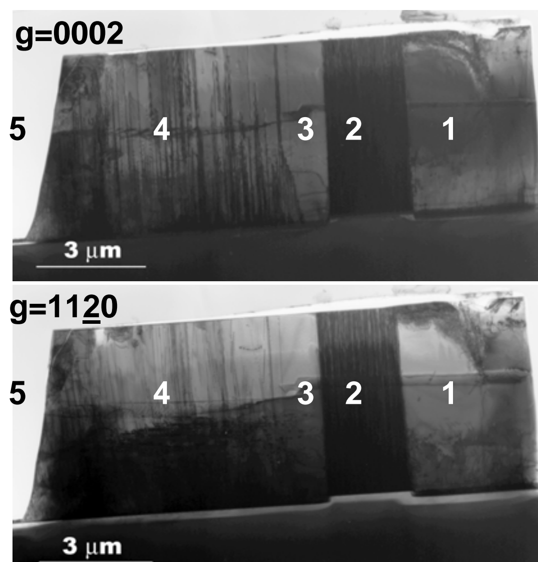

Fig. 5-3 Cross-sectional TEM g=(0002) and g=(11$\underline{2}$0) two beam bright field images.

According to the results of SEM image, the rough GaN layer grown on the window of TELOG without smooth nucleation layer is difficult to grow more than 0.2 μm. As a result, to obtain a better crystal quality a-plane TELOG GaN for the most of the area, the trench depth shall be down to at least 0.2 μm deeper than the sapphire surface to prevent the coalescing between the TELOG layer and thin GaN layer.

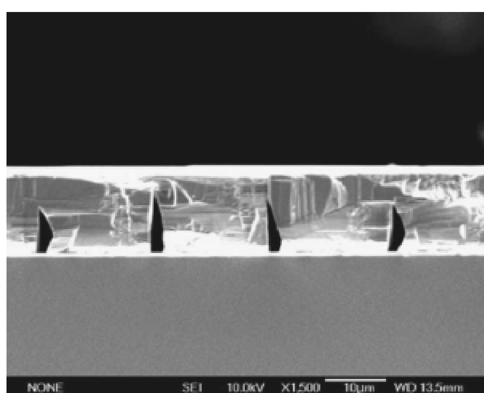

Fig. 5-4 Cross-sectional SEM of fully coalesced TELOG a-plane GaN film with 2 μm seed /18 μm trench pattern.

We then continue to perform the TELOG process with a 2-μm-seed / 18-μm-trench stripe pattern to obtain a fully coalesced a-plane GaN film, as shown in the SEM image of Fig. 5-4. The coalescence process can fully be completed for the thickness around 10 μm, it is a useful technique to overcome the thickness problem that the previous ELOG always needs more than 30 μm to fully coalesce [6].

5-4 Defects reduction of using InGaN/GaN superlattices

To demonstrate dislocation reduction of the a-plane GaN with the insertion of InGaN/GaN SLs, TEM was performed to investigate the comparative microstructure of a-plane GaN between with and without using

SLs. The cross sectional TEM image of the sample with SLs is shown in Fig. 5-5. From the TEM image, that TDs could not penetrate SLs layer was observed at the n-GaN/ SLs interface. Thus it was apparent that the insertion of InGaN/GaN SLs can reduce the dislocation density effectively. The estimated TDD was reduced from 3×10^{10} cm^{-2} down to ~9×10^{9} cm^{-2}. In order to confirm the performance improvement of a-plane GaN using InGaN/GaN SLs, Arrhenius plots of the normalized integrated PL intensity for the a-plane GaN without and with InGaN/GaN SLs over the temperature range 90–300 K was used. Sample.1 and Sample.2 are the a-plane LEDs without and with InGaN/GaN SLs, respectively.

Fig. 5-5 Cross sectional TEM image of a-plane GaN with SLs.

Fig. 5-6 (a) and (b) shows the normalized integrated PL as a function of 1000/T for Sample.1 and Sample.2, respectively, wherein the thermal activation energies of 83.7 meV and 105.3 meV were estimated from the Arrhenius plots. Furthermore, the integrated PL intensity ratio obtained at 90 K and 300 K [I_{PL}(300 K) / I_{PL}(90 K)] for Sample.2, which is approximately 17.8%, is larger than that of Sample.1 (nearly 10.27%). In general, the temperature-induced quenching of luminescence could involve the thermal

emission of charge carriers out of confined quantum-well states into barrier states [7, 8], thermal dissociation of excitons into free-electron–hole pairs [9], and thermal activation of excitons to non-radiative defect states [10]. Therefore, the thermal activation energy is a quantity to measure the exciton binding energy or the energy difference between the energy of the quantum-well confined state and the barrier continuum state or defect state. As a result, the carrier confinement of a-plane MQWs was indeed enhanced by InGaN/GaN SLs in terms of activity energy estimation.

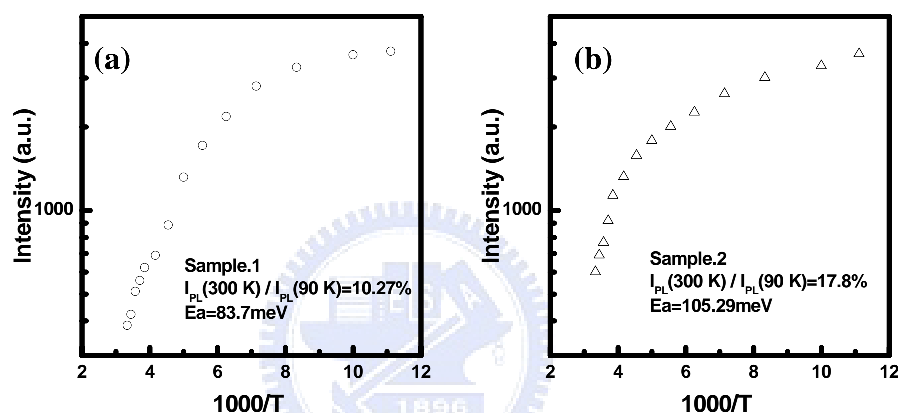

Fig. 5-6 Arrhenius plots of the normalized integrated PL intensity over the temperature range 90–300 K for (a) Sample.1 and (b) Sample.2

5-5 Summary

In this chapter, we proposed several approaches to improve crystal quality and surface morphology of nonpolar a-plane GaN grown on r-plane sapphire, including TELOG and using InGaN/GaN SLs .

In first part, we have grown high quality and fully coalesced a-plane GaN films at the thickness of 10 μm by using TELOG with a 2-μm-seed / 18-μm-trench stripe pattern. The TDD can be reduced largely from 1×10^{10} cm^{-2} to 3×10^{7} cm^{-2} for the N-face GaN wing. The Ga-face GaN could be much easily influenced by the thin GaN layer grown on the bottom of trench,

indicating that a narrower stripped GaN seeds and deeper trench etched into the surface of sapphire can derive a better quality a-plane TELOG GaN film for the most of the area.

In second part, we have demonstrated that the performance enhancement on a-plane LEDs was achieved by the insertion of InGaN/GaN SLs. The TD density was reduced from 3×10^{10} cm^{-2} down to ~9×10^{9} cm^{-2}. From the Arrhenius plots, the thermal activation energy of the sample with InGaN/GaN SLs which was estimated to be 105.3 meV, was larger than 83.7 meV of the sample without InGaN/GaN SLs.

Reference

[1] M. D. Craven, S. H. Lim. F. Wu, J. S. Speck, S. P. DenBaars, Appl. Phys. Lett., 81, 469, 2002.

[2] D. N. Zakharov, Z. L. Weber, Phys. Rev. B 71, 235334 (2005).

[3] H. Wang, C. Chen, Z. Gong, J. Zhang, M. Gaevski, M. Su, J. Yang, and M. A. Khan, Appl. Phys. Lett. 84. 499 (2004).

[4] M. D. Craven, S. H. Lim, F. Wu, J. S. Speck, and S. P. DenBaars, Appl. Phys. Lett. 81, 1201 (2002).

[5] J.W. Matthews and A.E. Blakeslee, J. Cryst. Growth 27, 118 (1976); 32, 265 (1976).

[6] B. M. Imer, F. Wu, S. P. DenBaars, and J. S. Speck, Appl. Phys. Lett. 88, 061908 (2006).

[7] H. M. Ng, Appl. Phys. Lett. 80, 4369 (2002).

[8] A. Chakraborty, B. A. Haskell, S. Keller, J. S. Speck, S. P. DenBaars, S. Nakamura, and U. K. Mishra: Appl. Phys. Lett. 85, 5143 (2004).

[9] A. Chakraborty, Stacia Keller, Cedrik Meier, Shuji Nakamura, James S. Speck, and Umesh K. Mishraa, Appl. Phys. Lett. 86, 031901 (2005).

[10] B. Rau, P. Waltereit, O. Brandt, M. Ramsteiner, K. H. Ploog, J. Puls, and F. Henneberger: Appl. Phys. Lett. 77, 3343 (2000).

Chapter 6 Optical properties of nonpolar InGaN/GaN multiple quantum wells

The optical characteristics of *c*-plane InGaN/GaN MQWs have been studied extensively [1, 2]. Chakraborty *et al.* has investigated the effect of defect density on optical properties of a-plane InGaN/GaN grown on laterally epitaxially over grown a-plane GaN [3]. However, the optical properties of *a*-plane InGaN/GaN MQWs are not fully understood, including the effects of the lack of the internal field and possible different growth parameters. In this chapter, the effect of a-plane InGaN/GaN MQWs with different well widths on localization phenomenon will be examined by a series of optical measurements. We also propose a rotational model and state a detail explanation of this localization.

6-1 Motivation

In general, the defect amounts of c-plane GaN, threading dislocation density is about 10^7 ~ 10^8 cm^{-2} which is less than that of both a- and m-plane GaN [4]. Typically, there is around the threading dislocation density of 10^9 ~10^{10} cm^{-2} for both a- and m-plane GaN structures [5~7]. Unlike most stacking faults are essentially generated and close to the nucleation layer for c-plane GaN [8], on the contrary, the different type of the stacking faults which distributed the whole a-plane GaN structure. Therefore, since the interface roughness and treading dislocations in *a*-plane heterostructures are more complicated than those in *c*-plane heterostructures [5], the luminescence mechanism requires further clarification of the dependence of the optical characteristics on the different InGaN/GaN quantum well width. Though

Craven *et al.* has investigated optical characteristics of a-plane GaN/AlGaN MQWs with difference well width [9], however, the issues related to well width dependence of *a*-plane InGaN/GaN MQWs including luminescence efficiency and time-resolved analysis of carriers have not yet been confirmed.

In this paper, we will report on optical characteristics of non-polar *a*-plane InGaN/GaN MQWs with different well widths grown by MOCVD on r-plane sapphire substrates. The PL experiments showed different optical properties between samples of different widths. Our CL images and scanning micro-PL images show the surface of the thinner well width had the more localized emission map of the samples, which revealsrevealing the relation between well width and surface emission of *a*-plane InGaN/GaN MQWs. Furthermore, the results of temperature dependent PL revealed the localization features clearly, and low temperature TRPL technique measurements further identified the localization effects in these samples.

6-2 Sample preparation and optical measurements

All epitaxial films were grown on r-plane sapphire by MOCVD. TMGa, TMIn, and ammonia were the precursors used for sources of Ga, In and N in whole epitaxyial process. At first, the r-plane sapphire substrate was treated by thermal annealing at 1090 ^{o}C. Subsequently, a 30 nm nm-thickness AlN nucleation layer was deposited at 600 ^{o}C. The growth temperature was ramped up to 1120 ^{o}C to grow an *a*-planeand 2 μm-thick bulk GaN of 2 μm thickness with a flat surface were deposited. The detailed growth parameters were reported elsewhere. Four samples with different well width were grown for investigation. The MQWs structure was then grown at 700 ^{o}C, which consisted of 10 pairs of ~12 nm-thick GaN barriers and $In_xGa_{1-x}N$ wells.

ranging in width from 3~12 nm. The ω/2θ scans of X-ray diffraction at [11$\bar{2}$0] were applied for four samples. The results were modeled by using the software built in the XRD equipment and the simulation showed that the In composition of the quantum well was around 23%, the GaN barrier was around 12 nm thick and the approximate well width for different samples were from 3, 6, 9, and to 12 nm, respectively. Finally, the 50 nm capping layer of GaN was deposited. The width and composition of the quantum well were confirmed by the X-ray measurement results.

The spatially resolved CL imaging data were obtained by the SEM over variousthe samples with the same viewing scale. We also used a scanning optical microscopy to obtain μ-PL mappings pumped by a He-Cd laser operating on 325 nm with 25 mW at room temperature with spatial and spectral resolutions of 1 μm and 1 nm, respectively, pumped by a He-Cd laser operating on 325 nm with 25 mW at room temperature. The ω-scan measurements of high resolution XRD made with a Philips MRD X'pert PRO diffractometer using Cu*K*α1 radiation confirmed the quantum well dimensions and barrier composition.

Room temperature PL measurements were performed using the CW 325 nm of a CW He-Cd laser operating at an excitation level of 25 mW. Meanwhile, power-dependent PL measurement was carried out by using of excited power density arranging from 2 ~ 200 mW/cm^2 was also achieved. After above experiments, the samples were placed in a vacuum chamber of 1.3 Pa attached to a closed-cycle Helium cryogenic chamber for further temperature dependent PL experiments between 20~300 K. In addition, time-resolved PL measurements were also performed using the method of time-correlated single-photon counting and using a pulsed GaN diode laser operating at a

wavelength of 396 nm as the excitation source between 9~300 K. According to the report by Jordan *et al.* [10], the carrier density n_0 could be given by $n_0 = 0.68A(1-R)P/(\hbar\omega S\gamma)$, where $\hbar\omega$ is the photon energy, S is the excited area, and γ is the laser repetition rate. In our case, the average laser pumping power was 0.2 mW with a laser pulse width of 56 ps operated at 10 MHz. The diameter of spot size was around 200 μm. Taking into account the reflection coefficients R = 23% and the absorption A in the order of 10^5 cm^{-1}, we can calculated the initial carriers density in our excitation condition was around 1.3×10^{10} cm^{-2}. The pumped effective carrier density of 1.3×10^{10} cm^{-2} was in the low excitation condition to prevent the strong carrier-carrier scattering. The collected luminescence was directly dispersed by a grating spectrometer and was detected by a high-speed PMT. The PL signal is fed into a Time Harp counting card, which was triggered with a signal from the diode laser. The instrument response time of this time-correlated single-photon counting system is about 300 ps.

6-3 PL characteristics and spatial emission distribution of a-plane InGaN/GaN MQWs

The CW PL spectra of these four samples measured at room temperature are shown in Fig. 6-1 (a). The PL peak emission energy of the MQWs increased from 2.47 eV to 2.79 eV with the decreasing well width, which could be attributed to the quantum confinement effect [11, 12]. These peak positions for different well width were also confirmed by the quantized energy levels obtained by the theoretical calculation when taking into account the In composition, barrier width and the flat band well. The similarity of peak energies for the 9 and 12 nm samples wereas similar due to the weak quantum

confinement of effect for larger sizewell widths. The iInsertion of Fig. 6-2 (b) shows that the integrated PL peak emission a-plane InGaN/GaN MQW intensity, the decreased optimal a-plane InGaN/GaN MQW emission intensity was associated with 6 nm InGaNwith the increasinge of InGaN well width. As the well width was increased beyond 6 nm, the PL intensity dropped more quickly.

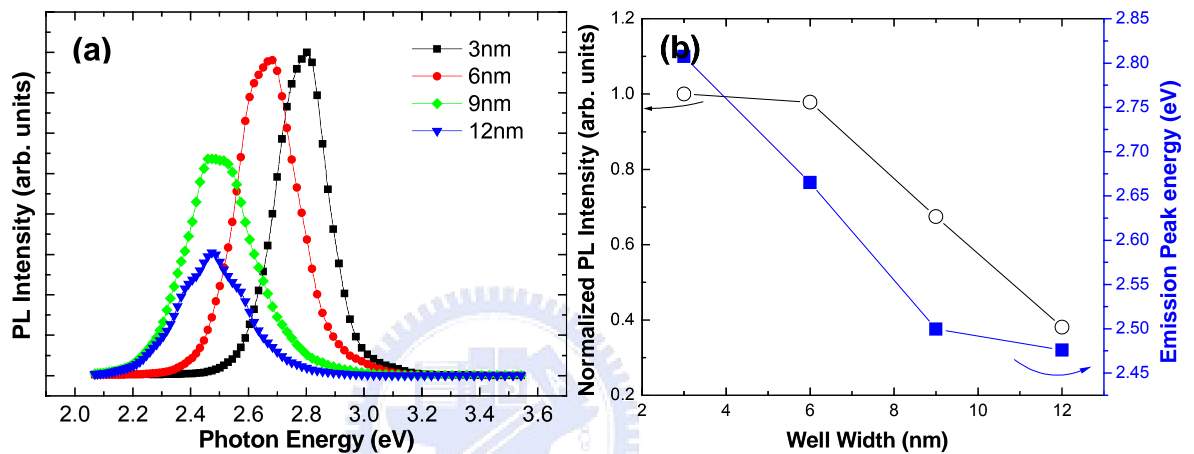

Fig. 6-1 (a) Room temperature PL spectra of *a*-plane InGaN/GaN MQWs with well width ranging from 3~12 nm. (b)Normalized PL intensity and energy peak plotted as a function of quantum well width.

We then analyzed different power dependences $I \sim P^{\alpha}$ for the samples of different well widths over a wide range of excitation power, where I is the PL intensity, P is the pumping power intensity, and α is the power index. In Fig. 6-3, the relationship between PL integrated intensity and excitation power density is observed. The respective inset figure reveals a full PL spectrum for all samples at room temperature. We have obtained un-shifted PL peaks with increasing pumping power density, which is well known for *a*-plane hexagonal MQWs with the characteristic non-polar flat band structure [13]. Fig. 6-3 (b)The power indexes around 1 for our all samples both indicated that the radiative

recombination dominated the optical transition [14] and gave additional evidence that no built-in electric field was present within any of our *a*-plane InGaN/GaN MQWs. However, such *a*-plane MQWs without the built-in electric field sshould not exhibit a large PL intensity dependence on the well width [15]. Other factors such as interface fluctuation, material quality and carrier localization in the MQWs could play important roles in the PL emission intensity.

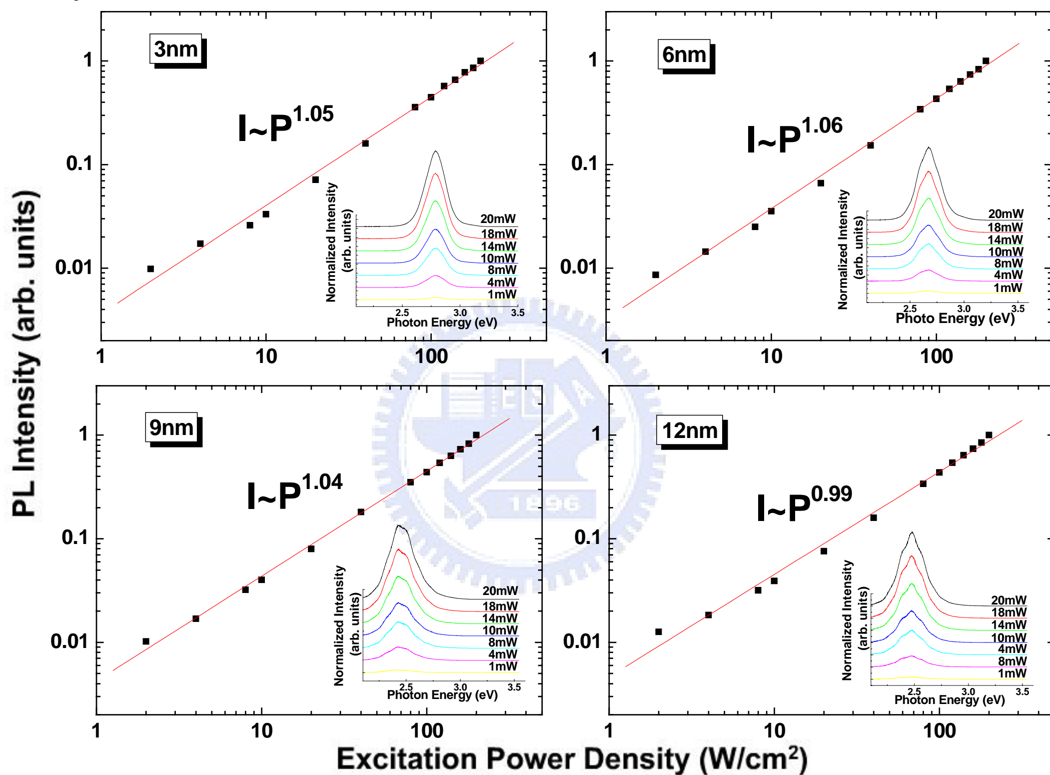

Fig. 6-2 The relation between PL intensity and excitation power density for a-plane InGaN/GaN MQWs with different well widths. Insert images illustrate PL spectra as functions of the excitation power for the four a-plane InGaN/GaN MQWs with different well width.

Fig. 6-3 shows the CL and μ-PL emission images offor the four samples surface of using optical filters at relativethe peak emission wavelength corresponding to each sample. The samples with thinner wells exhibited many,

We could find the relatively larger and uniform luminescence patterns, indicating a higher crystal quality of their InGaN/GaN MQWs region In contrast, the sample with 12 nm-thick wells showed fewer and smaller luminescence patterns, demonstrating a high degree of inhomogeneity and reduced MQW crystal quality.

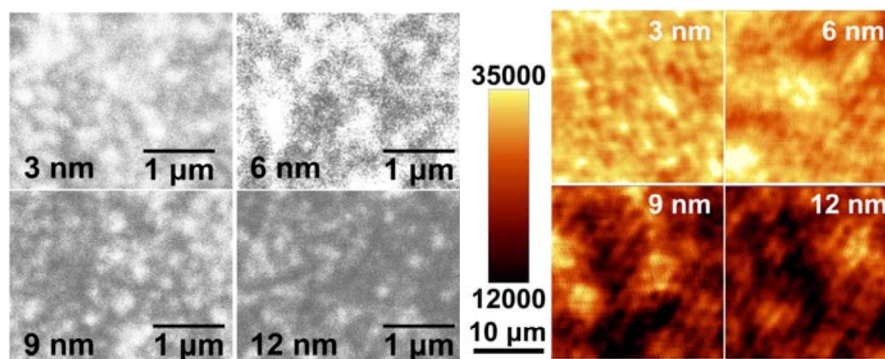

Fig. 6-3 (a) Monochromatic top view CL images on samples of different well widths using optical filters at the corresponding peak emission wavelengths. (b) Top viewμ-PL image of the same samples using optical filters at the corresponding peak emissions wavelengths. The detected emission energies were 2.81, 2.67, 2.49 and 2.47 eV for the samples with 3, 6, 9 and 12 nm well widths, respectively.

These images revealed that the intensity of emission gradually decreases with increasing well width, which was consistent with the PL results. Such results were also similar to the results of μ-PL mapping shown in Fig. 6-3 (b). In addition, atomic force microscopy (AFM) was applied for further identification of crystal quality. The results of plan-view AFM images indicated that the root means square roughness gradually increased with increasing well width. The AFM result could give us additional proof that the crystal quality of MQWs improves when the well width was thinner. Accordingly, the CL images and μ-PL mapping with thinner well due to less degree of In separation, which

also would give a evidenceevidence ofthat increasing well width increases more localized states and produces poor luminescence efficiency. Therefore, CL images apply a reliable proof to support.

6-4 Localization features in a-plane InGaN/GaN MQWs

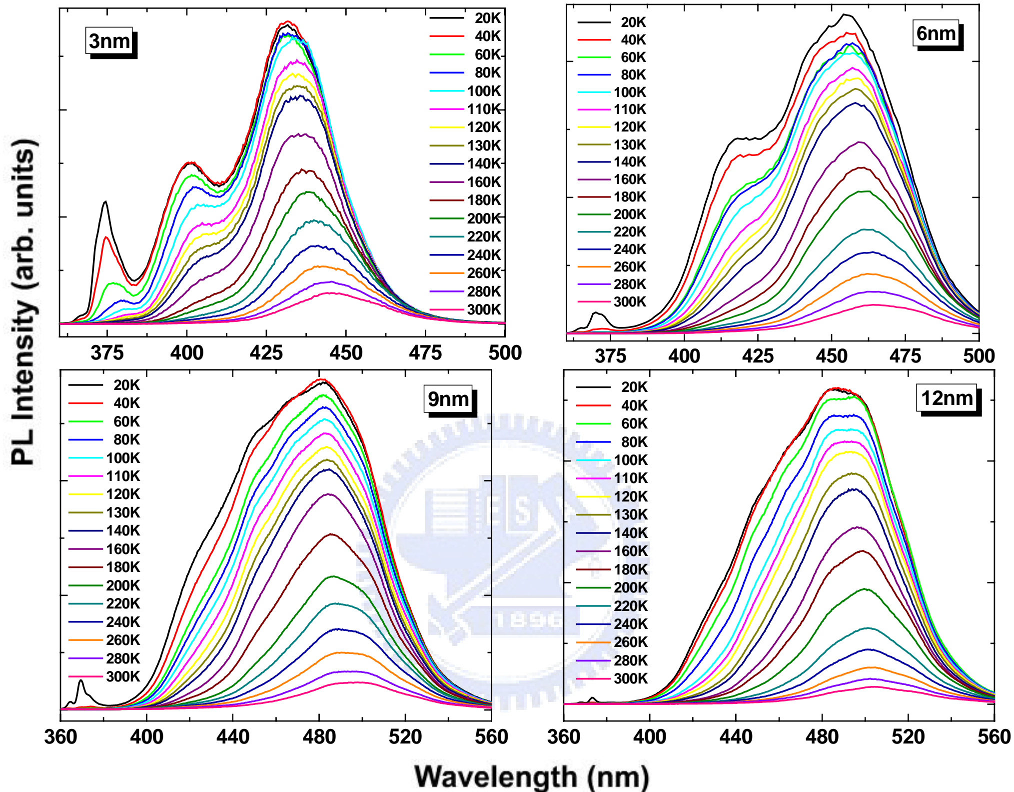

Fig. 6-4 PL spectra as a function of temperature from 20 K to 300 K for a-plane InGaN/GaN MQWs with different well width.

Fig. 6-4 shows the evolution of the a-plane InGaN/GaN MQWs PL spectra as a function of temperature from 20K to 300K for each well width. The decrease of PL intensity with increasing temperature was observed. This thermal quenching PL intensity is a common phenomenon in III-V semiconductor, which results from carriers' thermalization from either the radiative recombination centers or the localized states (or both) to the nonradiative recombination centers. In addition, three separated peaks

appeared in the PL spectrum. The high-energy peak of 3.35 eV in all samples is attributed to the signal of bulk GaN. The middle energy peak of 2.8 eV was clearly present in the samples of 3 nm and 6 nm well width, whereas this peak broadened and merged with the lowest-energy signal in the samples of 9 nm and 12 nm well width. This energy peak could be attributed to the signal coming from shallow localized states. The lowest energy signal came from the optical transition in deep localized states. Obviously, the PL emission from excitons in deep localized states dominates the luminescence from 20 K to room temperature, and the other two higher energy emissions suffer an apparent, rapid thermal quenching when the temperature increases. Since the exciton dynamics at shallow localized states is very sensitive to the lattice temperature, it is hard for excitons to remain stable in shallow localized states when the temperature increases [16]. Therefore, the excitons in the shallower localized states have higher probabilities of transferring to the non-radiative recombination centers or relaxing into the lower localized states, both of which would quench the emission from high energy states [17]. Because the emission from shallow localized states decreased with increasing temperature, and then the efficient radiative recombination of excitons could occur mainly at deep localized states. For both samples with thinner well widths of 3 and 6 nm, the emission of excitons from one or several shallow localized states with one dominant energy level was apparent. In comparison, the emission from shallow localized states in the samples with well widths of 9 nm and 12 nm seemed to be broadened at all temperature regions, indicating that there could be many shallow localized states with different energy levels in the thicker QWs. The reasons for this phenomenon could be attributed to two factors. One is that the In composition is not uniform especially in the thicker QWs, and thus

more localization energy depths occur. The other factor is probably due to rough interfaces between well and barrier layers in MQWs structure. The exciton energy can be defined as a function of x and L in the MQWs, which can be written as:

$$E\ (x,\ L) = E_g(x) + E_c(L) + E_b \tag{6-1}$$

where x is In composition and L is well thickness. The symbols, $E_g(x)$, $E_c(L)$ and E_b are the energy gap of InGaN well, confinement energy and binding energy of the exciton in InGaN well, respectively. The well width L in Eq. 6-1 is a function of confinement energy of exciton. Different well width L can influence the whole exciton energy E (x, L). Therefore, the interface roughness in InGaN/GaN MQWs causes well width fluctuation, which leads to different confinement energy of exciton [18]**.** Note that the impact of interface roughness on $E_c(L)$ is more severe when the quantum well is thinner. Even one mono-layer difference in the quantum well thickness will result in a large energy difference. On the other hand, when the quantum well thickness is thicker, the interface roughness will result in many small energy variations of $E_c(L)$, which could explain why broaded shallow localized states with different energy levels exist in the thicker QWs. Narukawa *et al.* also pointed out the correlation between the interface roughness and alloy disorder in InGaN/GaN MQWs [19], attributing the broad PL spectra to not only In phase separation but also well width fluctuation.

In order to further check the degree of alloy and interface fluctuations in these four samples, we analyzed the peak shift of the InGaN MQW emission over the investigation temperature range as shown in Fig. 6-5 (a)~(d). For the samples with 3 nm and 6 nm well widths, the emission energy decreased monotonically with increasing temperature. However, for the samples with 9

nm and 12 nm well widths, the emission energy decreased at temperatures below 70 K, then increased with increasing temperature from 70 K to around 140 K and finally decreased with further increase of temperature up to the room temperature.

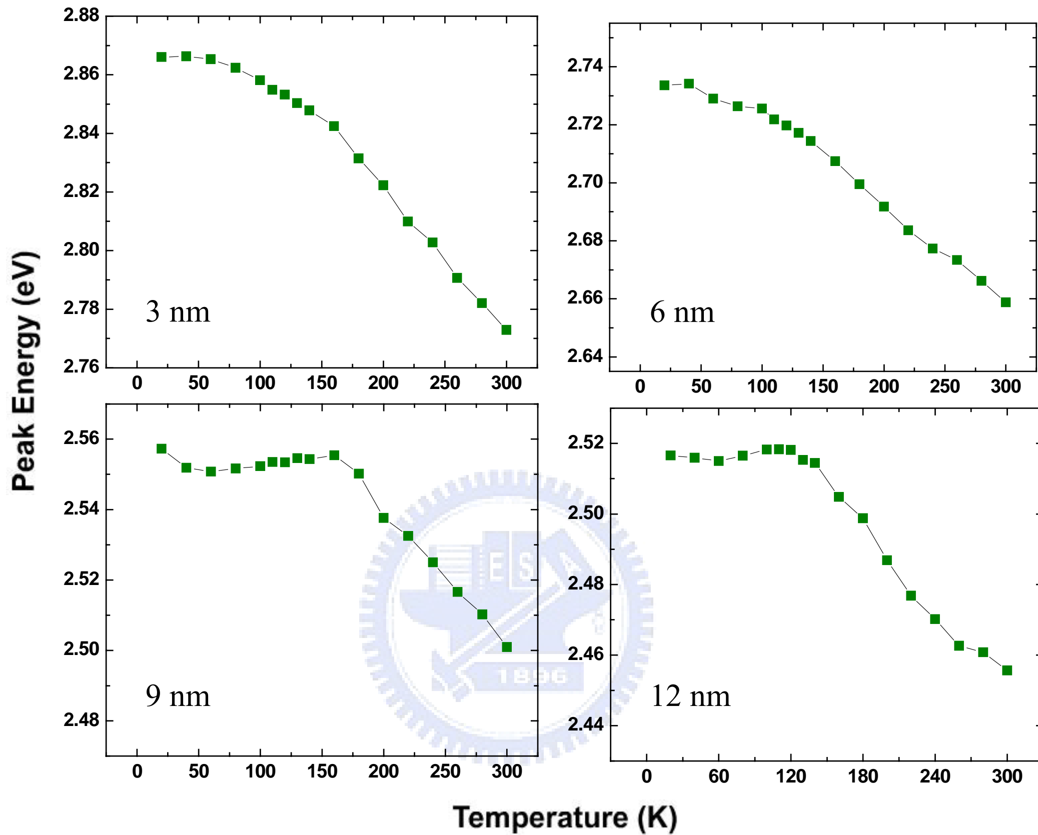

Fig. 6-5 PL peak energy position as a function of temperature for a-plane InGaN/GaN MQWs with different well width.

This red-blue-red shift of peak energy with increasing temperature is a famous characteristic of the exciton localization effect [16, 20]. From 20 K to 70 K, the observed dynamical redshift of the PL spectrum is considered to be caused by migration of excitons from higher states into lower localized states. At elevated temperature from 70 K to 140 K, nonradiative recombination processes become more pronounced, and some carriers recombine before reaching deeper band-tail states, resulting in a blueshift in the PL peak position.

At higher temperatures up to 300K, another redshift occurs mainly due to the temperature-dependent dilation of the lattice and electron–lattice interaction [21, 22]. The total redshifts of the four samples over the temperature ranges used are: 100 meV, 75 meV, 55 meV and 62 meV for 3 nm, 6 nm, 9 nm and 12 nm QW widths, respectively. The absence of S-curve characteristics for emission peak energies of 3 and 6nm well widths could be due to a deeper localization depth for thinner wells, confining carriers tightly. Thus distinctively visible S-shaped temperature dependent behavior would not appear [23]. This is also consistent with our above inference that probably due to In phase separation and interface roughness.

6-5 Analysis of localization depth

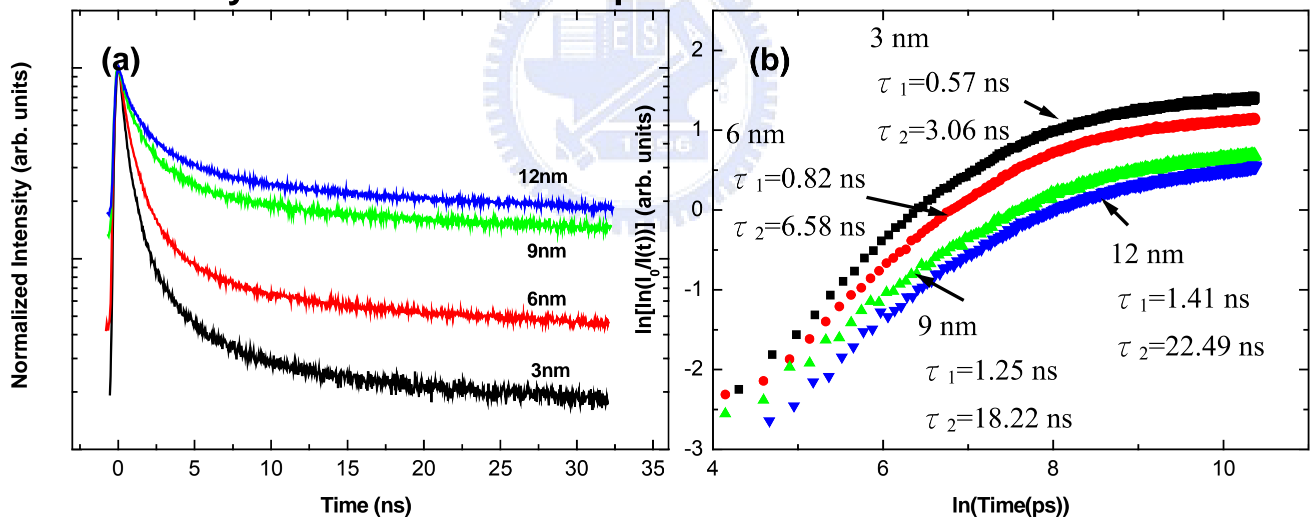

Fig. 6-6 (a) TRPL signals of emission peaks in the *a*-plane InGaN/GaN MQWs with different well width. (b) Relation between In[In{I(0)/I(t)}] and In(t) for the signal in (a).

Fig. 6-6 (a) shows the low temperature time-resolved PL spectrumdecay for samples with different well widths. Since the measurement was carried out at 9 K, the influence of the non-radiative recombination process could be

excluded [24]. The aAll experiment data was fitted by a combined exponential and stretched exponential line shape $I(t) = I_1(0) \exp(-t / \tau_1)+I_2 (0)\exp[-(t /\tau_2)^{\beta}]$, which has been used to analyze the emission characteristics of non-polar InGaN/GaN MQWs [24, 25]. The parameter I(t) is the PL intensity at time t ; β is the dimensionality parameter that is related to the dimensionality of the localizing centers; τ_1 and τ_2 are the initial lifetimes of carriers. The fast decay time τ_1 (τ_1 = 0.57-1.41 ns) represents the radiative recombination of free excitons in the extended states or localized statesand radiative recombination of free excitons. The slow decay time τ_2 (τ_2 = 3.06-22.49 ns) accounts for communication or relaxation of excitons between localized states. Figure 6(b) shows the relation between ln{ln[I(0) / I(t)]} and ln(t) for the data in Fig. 6-6 (a). We have obtained fast free exciton decay times τ_1 of 0.57 ns and the communication time τ_2 of 3.06 ns for the *a*-plane MQWs with 3-nm well width in comparison to the values of > 6 ns reported for *c*-plane MQWs. However, Bboth of the PL decay times τ_1 and τ_2 detectably increased with the QW width as shown in Fig. 6-6. Fig. 6-3 (b) shows the relation between ln{ln[I(0) / I(t)]} and ln(t) for the data in Fig. 6-1 (a). The well-width dependent radiative exciton lifetime could describe different optical transition path of carriers. In general, growing a thick well would spend using a long growth more time which wcould easily cause fluctuation of the In diffusion length and form worse interfaces ofbetween wells/ and barriers. Increasing the degree of In separation wcould result in more localized states in the MQWs. Therefore, the more localized states in the thicker well width wcould trap parts of carriers transitioning from higher levels to lower levels and further delay the both lifetimes, τ_1 and τ_2,. The longer exciton lifetime would decrease the PL emission intensity, which also explained the PL results of peak emission

intensity as shown in Fig. 6-1(b).

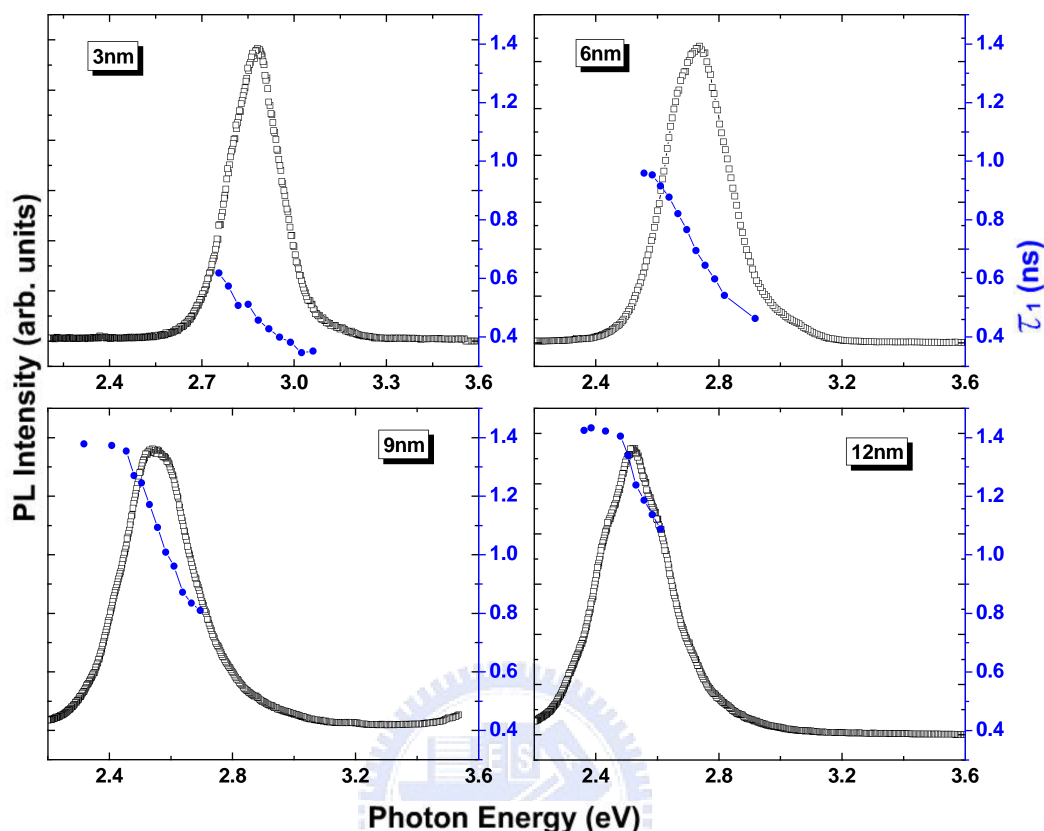

Fig. 6-7 PL decay time as a function of monitored photon energy at 9 K (black) and the fitting data for the *a*-plane InGaN/GaN MQWs with different well width (blue).

We also analyze the decay time corresponding to different energies of the PL spectra at 9 K, which provides further evidence of the inhomogeneously broadened localization effect in these four samples. Fig. 6-7 shows the PL decay time as a function of monitored photon energy at 9K for the four samples. We attribute the circumstance to the existance of tail states [26, 27]. The density of the tail states could be described as exp $(-E/E_0)$, where E_0 represents the average of the depth difference between respective shallow localized centers and deep localized centers in the tail states. The PL decay time increases with decreasing monitored photon energy, which is

characteristic of localized excitons in an exponential-tail density of states. The experimental results can be fitted by the equation [28]:

$$\tau_{PL}(E) = \tau_r / \{1+\exp[(E-E_{me})/E_0]\} \qquad (6\text{-}2)$$

where E_{me} is the energy of the absorption edge and τ_r is the effective lifetime. The resulting fitting parameters of the localization depth E_0 are 175 meV, 71 meV, 49 meV, and 25 meV for 3 nm, 6 nm, 9 nm, and 12 nm samples, respectively. The results show a deeper localization depth in thinner samples. Since the thermal energy is 26 meV at room temperature, excitons in the samples with thicker well widths could escape from an initial localized center with lower energy level to a higher one, creating a broader PL spectra of such samples at room temperature. This result agrees well with the temperature-dependent PL experiment.

6-6 Three-level localized exciton model

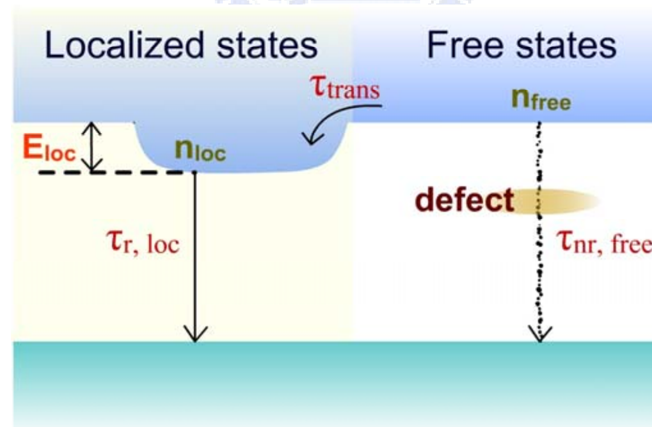

Fig. 6-8 Schematic diagram of the localized exciton system. Excitons are transferred from free/extended states to the localized states.

Chichibu *et al.* have given an explanation of the carrier transition mechanism for InGaN/GaN system as a simplified three-level schematic diagram of a localized exciton system shown in Fig. 6-8 [29]. In this model,

excitons are transferred from the free/extended states to the localized states. The localization lifetime (τ_{loc}) is defined as the superposition of both the relaxation lifetimes of QW excitons transferring from free/extended states to localization centers and the radiative lifetime of localized excitons. τ_{loc} is a physical parameter which increases with temperature T and with the occupancy of the localization states, while it decreases with increasing in localization depth E_{loc}. We analyzed the radiative and nonradiative processes as a function of temperature for the four samples with different quantum well width. Values of the localization lifetime τ_{loc} and nonradiative lifetime in the free/extended states ($\tau_{nr,free}$) are deduced from τ_{PL} and η_{int} (internal quantum efficiency) as a function of temperature using the relation:

$$\eta_{int} = 1/(1+\tau_{loc}/\tau_{nr,free})$$

$$1/\tau_{PL}=1/\tau_{loc}+1/\tau_{nr,free}. \qquad (6\text{-}3)$$

It is reasonable to assume that τ_{loc}, introduced in the three-level localized exciton model, combines with the superposition of τ_1 and τ_2 obtained in Figure 5. Here we used the fast decay factor τ_1 to represent τ_{PL} because it dominated the PL intensity [30]. Internal quantum efficiency η_{int} can be estimated by using the ratio of temperature dependent integrated PL intensity between a given temperature T and the low temperature of 20 K [31]. The calculation results of $\tau_{nr,free}$ and τ_{loc} are plotted in Fig. 6-9 by using Eq. 6-3. The τ_{loc} for all samples at low temperatures less than 100 K were around 1 ns, shorter than that of c-plane QWs, demonstrating the flat band feature of non-polar QWs. The τ_{loc} increased and the $\tau_{nr,free}$ decreased with increasing temperature, indicating that the efficiencies of the defect trapped excitons gradually strengthened as temperature rose.

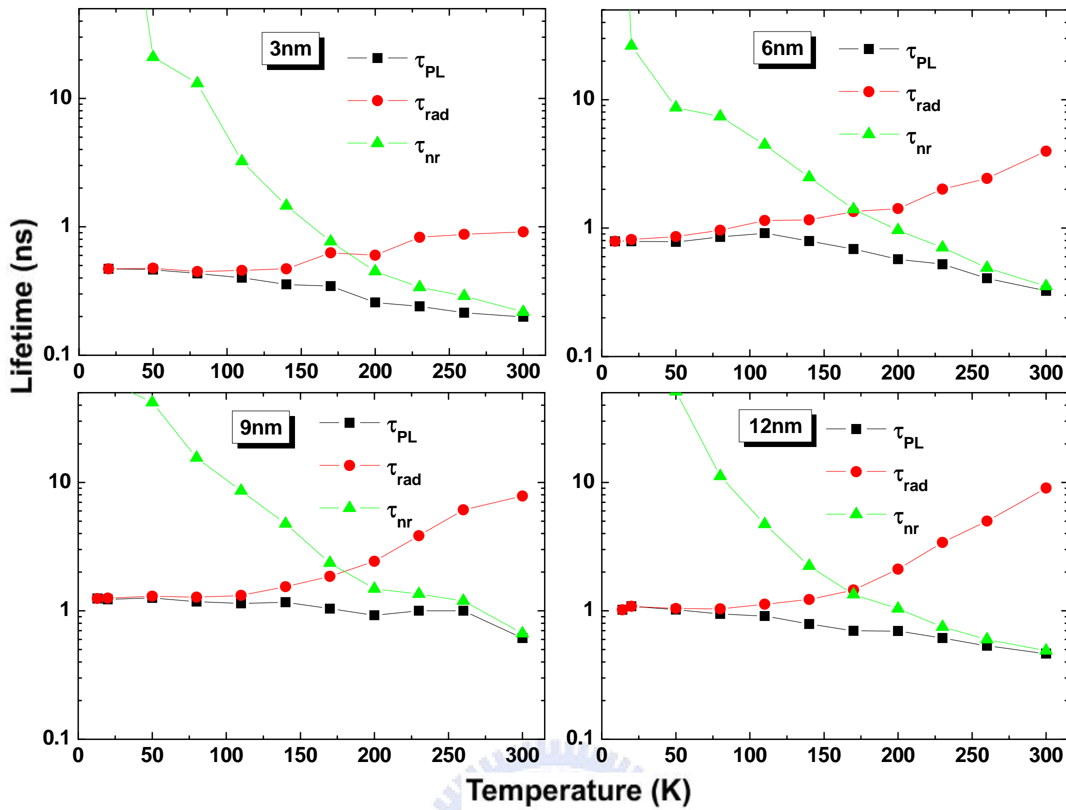

Fig. 6-9 PL lifetime τ_{PL} of a-plane InGaN/GaN MQWs with different well widths as a function of temperature. The localization lifetime τ_{loc} and the nonradiative lifetime at the free/extended states $\tau_{nr,free}$, estimated from the temperature dependent TRPL signal and PL intensity are also plotted. The τ_{PL}, τ_{loc}, and $\tau_{nr,free}$ correspond to the definitions in the three-level localized exciton model shown in Fig. 6-8.

Therefore, once the temperature increased beyond 200K, τ_{PL} was dominated by $\tau_{nr,free}$ in the four samples. On the other hand, τ_{loc} of the sample with the thinnest 3 nm well width at 300 K(~1 ns) was 9 times shorter than that of the thickest 12 nm well width (~9 ns), which could be probably attributed to the difference in integrated intensity between the two samples. The $d\tau_{loc}/dT$ values indicate the abilities that localized centers trap and thermal activity for most excitons. At temperatures beyond 170K, the $d\tau_{loc}/dT$ values were

estimated as 3×10^{-3}, 2.5×10^{-2}, 5.6×10^{-2}, and 6.9×10^{-2} for the samples with well width of 3 nm, 6 nm, 9 nm, and 12 nm, respectively. Samples with thinner well width had smaller $d\tau_{loc}/dT$ values, thus excitons were strongly localized and the thermal escape to two-dimensional spaces was suppressed [23, 30]. As a result, shorter τ_{loc} and smaller $d\tau_{loc}/dT$ have indicated that effective capturing of excitons due to larger E_{loc} and/or shorter radiative lifetime of localized excitons was more prominent in thinner well width samples than thicker ones [32].

6-7 Summary

In this study conclusion, we used MOCVD to grow 10 pairs of *a*-plane InGaN/GaN MQWs of well width ranging from 3 ~ 12 nm grown by MOCVD on r-plane sapphire were investigated. The experimental results show both a stronger PL intensity and a wider emission CL and μ-PL area for samples with thinner well widths. The temperature dependent PL reveals that more uniform localization states, and all of the states have similar depth with similar depths for the samples with thinner well widths. In addition, more effective capturing of excitons due to larger localization energy E_{loc} and shorter radiative lifetime of localized excitons are observed in thinner well width samples by using temperature dependent TRPL. These phenomena are due to the better confinement of uniform and deep localized centers for excitons existing in the samples with thinner well widths, whereas more pronounced indium fluctuations or rougher interfaces in the MQWs exist in the samples with thicker well widths. These results should provide useful guidance supply the reference for the fabrication of light emitting devices by using *a*-plane InGaN/GaN MQWs structures.

Reference

[1] C. K. Sun, S. Keller, G. Gang, M. S. Minsky, J. E. Bowers, S. P. DenBaars, Appl. Phys. Lett., 69, 1936, (1996).

[2] C. K. Sun, S. Keller, T. L. Chiu, G. Wang, M. S. Minsky, J. E. Bowers, S. P. DenBaars, IEEE J. Quantum Electronics, 3, 731, (1997).

[3] A. Chakraborty, S. Keller, C. Meier, B. A. Haskell, S. Keller, P. Waltereit, S. P. DenBaars, S. Nakamura, J. S. Speck, U. K. Mishra, Appl. Phys. Lett., 86, 031901, (2005).

[4] S. C. Jain, M. Willander, J. Narayan, and R. Van Overstraeten, J. Appl. Phys. 87, 695, (2000).

[5] M. D. Craven, S. H. Lim, F. Wu, J. S. Speck, S. P. DenBaars, Appl. Phys. Lett., 81, 469, (2002).

[6] D. N. Zakharov, L. W. Zuzanna, B. Wagner, Z. J. Reitmeier, E. A. Preble, R. F. Davis, Phys. Rev. B 71, 235334 (2005).

[7] T. Nagai, T. Kawashima, M. Imura, M. Iwaya, S. Kamiyama, H. Amano, I. Akasaki, J. Crys. Grow. 298, 288 (2007).

[8] X. H. Wu, L. M. Brown, D. Kapolnek, S. Keller, B. Keller, S. P. DenBaars, and J. S. Speck, J. Appl. Phys. 80, 15 (1996).

[9] M. D. Craven, P. Waltereit, J. S. Speck, S. P. DenBaars, Appl. Phys. Lett. 84, 496, (2004).

[10] C. Jordan, J. F. Donegan, J. Hegarty, B. J. Roycroft, S. Taniguchi, T. Hino, E. Kato, N. Noguchi, and A. Ishibashi, Appl. Phys. Lett. 74, 3359 (1999).

[11] H. Teisseyre, C. Skierbiszewski, B. Łucznik, G. Kamler, A. Feduniewicz, M. Siekacz, T. Suski, P. Perlin, I. Grzegory, and S. Porowski, Appl. Phys. Lett. 86, 162112 (2005).

[12] N. Akopian, G. Bahir, D. Gershoni, M. D. Craven, J. S. Speck, and S. P.

DenBaars, Appl. Phys. Lett. 86, 202104 (2005).

[13] P. Walterelt, O. Brandt, A. Trampert, H. T. Grahn, J. Mennlger, M. Ramsteler, M. Relche, K. H. Ploog, Nature, 406, 865, (2000).

[14] E. Kuokstis, C. Q. Chen, M. E. Gaevski, W. H. Sun, J. W. Yang, G. Simin, M. A. Khan, Appl. Phys. Lett., 81, 4130, (2002).

[15] C. Monier, A. Freundlich, M. F. Vilela, J. Appl. Phys., 85, 2713, (1999).

[16] Y. H. Cho, G. H. Gainer, A. J. Fischer, J. J. Song, S. Keller, U. K. Mishra, S. P. DenBaars, Appl. Phys. Lett. 73**,** 1370 (1998).

[17] Y. Kanemitsu, K. Tomita, D. Hirano, H. Inouye, Appl. Phys. Lett. 88, 121113 (2006).

[18] K. C. Zeng, M. Smith, J. Y. Lin, and H. X. Jiang, Appl. Phys. Lett. 73, 1724 (1998).

[19] Y. Narukawa, Y. Kawakami, M. Funato, S. Fujita, and S. Nakamura, Appl. Phys. Lett. 70, 981 (1997).

[20] A. Bell, S. Srinivasan, C. Plumlee, H. Omiya, F. A. Ponce, J. Christen, S. Tanaka, A. Fujioka, Y. Nakagawa, J. Appl. Phys. 95, 4670 (2004).

[21] R. Moglich, R. Rompe, Z. Phys. 119, 492 (1942).

[22] J. Bardeen, W. Shockley, Phys. Rev. 80, 72 (1950).

[23] Y. T. Moon, D. J. Kim, J. S. Park, J. T. Oh, J. M. Lee, Y. W. Ok, H. Kim, and S. J. Park, Appl. Phys. Lett. 79, 599 (2001).

[24] T. Onuma, A. Chakraborty, B. A.Haskell, S. Keller, S. P. DenBaars, J. S. Speck, S. Nakamura, U. K. Mishra, Appl. Phys. Lett., 86,151918, (2005).

[25] Y. J. Sun, O. Brandt, S. Cronenberg, S. Dhar, H. T. Grahn, K. H. Ploog, P. Waltereit, J. S. Speck, Phys. Rev., B 67, 041306, (2003).

[26] F. Yang, M. Wilkinson, E. Austin, K. O'Donnell, Phys. Rev. Lett. 70, 323 (1993).

[27] S. F. Chichibu, Takashi Azuhata, Hajime Okumura, Atsushi Tackeuchi, Takayuki Sota, Takashi Mukai, Applied Surface Science 190, 330-338 (2002).

[28] Y. Narukawa, S. Saijou, Y. Kawakami, S. Fujita, T. Mukai, S. Nakamura, Appl. Phys. Lett. 74, 558 (1999).

[29] S. F. Chichibu, T. Onuma, T. Aoyama, K. Nakajima, P. Ahmet, T. Chikyow, T. Sota, S. P. DenBaars, S. Nakamura, T. Kitamura, Y. Ishida and H. Okumura : J. Vac. Sci. & Technol. B 21, 1856 (2003).

[30] T. Onuma, A. Chakraborty, B. A. Haskell, S. Keller, S. P. DenBaars, J. S. Speck, S. Nakamura, and U. K. Mishra, Appl. Phys. Lett. 86, 151918 (2005).

[31] T. Koyama, T. Onuma, H. Masui, A. Chakraborty, B. A. Haskell, S. Keller, U. K. Mishra, J. S. Speck, S. Nakamura, and S. P. DenBaars, Appl. Phys. Lett. 89, 091906 (2006).

[32] T. Onuma, Y. Uchinuma, E. K. Suh, H. J. Lee, T. Sota, and S. F. Chichibu, Jpn. J. Appl. Phys. 42, L1369 (2003).

Chapter 7 Nonpolar optoelectronic devices

The thorough understanding of the specific properties of nonpolar nitrides material is of critical importance toward their full potential. Even though high-quality nitride materials with nonpolar is investigated by many groups over the world, at present time, several issues remain to be clarified, many research indicates that many questions related to nonpolar materials will be answered and the material quality will be better controlled in future. In addition, the optoelectronic devices based on nonpolar is essential to be developed. In this chapter, we successfully fabricated LEDs by utilizing two approaches which have been introduced in Chapter 5, TELOG and InGaN/GaN SLs, to improve crystal quality of nonpolar GaN. The detailed description will be revealed in following sections.

7-1 Motivation

In general, there is a TD density of ~3×10^{10} cm^{-2} and a basal SF density of ~3.5×10^{5} cm^{-1} exist in a-plane GaN grown on r-plane sapphire structure [1]. The TDs in GaN act as nonradiative recombination centers to restrict internal quantum efficiency. Therefore, reducing TDs is essential to improve device performance. Lateral epitaxial overgrowth (LEO) techniques have been employed in the past for achieving defect reduction in nonpolar GaN [2-6]. However, all of these LEO techniques involving ex-situ processing steps and the thick regrowth thickness over than 20 μm for coalescence, are quiet difficult to control the uniformity. Therefore, we have proposed an approach to improve $[11\bar{2}0]$ a-plane GaN quality by using epitaxial lateral overgrowth on trenched a-plane GaN buffer layers [7]. The TELOG allowed us to obtain

a-plane GaN with low dislocation density, simple fabrication process, lower cost, and thinner coalescence thickness in comparison to the previous reports [8, 9], the relevant description has been introduced in Chapter 5. Another possible method for reducing TDD is the insertion of strain-layer SLs into the epitaxial layer which is also reported in Chapter 5. The strain due to different lattice constants in the SLs, can deflect the TD into the interfacial plane, had been analyzed by Matthews theoretically [10]. Herein, we divided this chapter into two major contents. In first part, we report on the fabrication and characteristics of ultraviolet nonpolar InGaN/GaN LEDs using reduced-defect TELOG a-plane GaN template. As for second part, we utilize the strain mechanism to realize defect reduction in a-plane LEDs and demonstrate the performance improvement of a-plane LEDs using InGaN/GaN SLs. Unlike these traditional LEO techniques, this dislocation reduction method is highly advantageous due to the simplicity and low cost. The detailed electrical properties were measured including L-I-V curve, EL and polarization measurements, which will be investigated in further sections.

7-2 Sample process and experiments

In using TELOG technique part, a-plane GaN films with 1.5 μm thickness were grown by low pressure metal-organic chemical vapor deposition (MOCVD) on r-plane sapphire substrates using conventional two-step growth technique. Then, a 2 μm seed / 7 μm trench TELOG stripe pattern was applied parallel to the $[1\underline{1}00]$ direction to realize vertical c-plane sidewalls followed by etching of SiO_2 using inductively coupled plasma etching through the windows to the GaN epitaxial film. GaN stripes were etched by reactive ion etching through the mask openings, down to the r-plane sapphire substrate. The SiO_2

mask was removed by hydrofluoric acid to simplify the growth process. We then continue to perform the regrowth process on 2 μm seed / 7 μm trench stripe patterns to obtain a fully coalesced a-plane GaN template. Afterward the LED structure was regrown by MOCVD on a-plane TELOG GaN template.

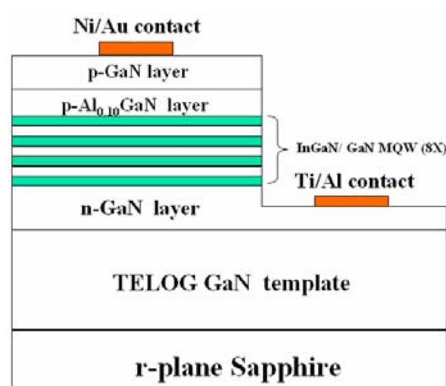

Fig. 7-1 Structure of the ultraviolet nonpolar TELOG LED.

Fig. 7-1 shows the structure of the ultraviolet nonpolar TELOG light-emitting diode. It consisted of 12 μm thick TELOG GaN template, a 1.5 μm thick Si-doped n-GaN with an electron concentration of 3×10^{18} cm^{-3}, a 0.1 μm thick n-GaN with an electron concentration of 1×10^{18} cm^{-3}, followed by the active region, which consisted of 8 pairs MQWs with 15 nm thick GaN barriers and 5 nm thick InGaN wells. A 30 nm thick p-type $Al_{0.1}Ga_{0.9}N$ electron blocking layer separated the active region from the 0.16 μm thick p-type GaN with a hole concentration of 6×10^{17} cm^{-3}. After MOCVD growth, the LED wafer was partially etched by reactive ion etching from the surface of the p-type GaN until the n-type GaN was exposed. A Ni/Au contacting metal layer was evaporated onto the p-type GaN contact layer, and a titanium/aluminum (Ti/Al) contact was evaporated onto the n-type GaN layer, respectively.

In second part of using InGaN/GaN SLs layer, the initial sample structure is the same with the report in Chapter 5 and subsequently a 1.5-μm-thick

Si-doped n-GaN with an electron concentration of 3×10^{18} cm^{-3} was grown. Afterward, a 10 pairs MQWs consisted of 6-nm-thick wells and 15-nm-thick barriers were grown at temperature of 827 ^{o}C and were capped by a 0.15 μm-thick p-GaN layer with a hole concentration of 6×10^{17} cm^{-3}. The structure of a-plane LED is shown in Fig. 7-2. Then, 300×300 μm^2 diode mesas were defined by chlorine-based reactive ion etching. Ti/Au (100/200 nm) and Ti/Al/Pt/Au (30/180/40/150 nm) were used as p-GaN and n-GaN contacts, respectively.

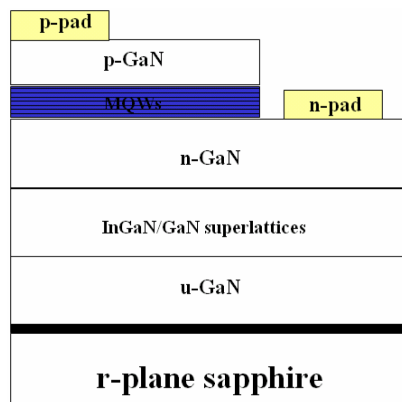

Fig. 7-2 Structure of a-plane LED with the insertion of InGaN/GaN SLs.

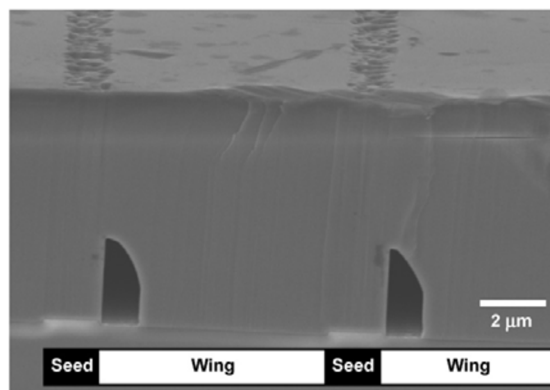

Fig. 7-3 Cross-sectional SEM image of TELOG a-plane LED with 2 μm seed / 7 μm trench patterns.

The as-grown samples of using both techniques were investigated by

TEM for the microstructure of a-plane LEDs. The comparison of surface morphologies and defect distributions over various areas were obtained by using SEM and spatially resolved CL). The LED spectrum and degree of polarization were measured by EL.

7-3 Effect of TELOG structure on electronic properties

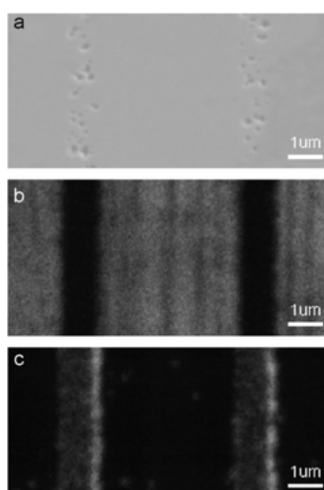

Fig.7-4 (a) Plan-view SEM image, including seed regions and wing regions (b) monochromatic CL image at 373 nm and (c) monochromatic CL image at 443 nm.

Fig. 7-3 shows the cross-sectional SEM image of the a-plane UV LED grown on TELOG substrate. Most TDs were located on the GaN seed stripes: they originated from the GaN seed and penetrated through the MQWs to the p-type GaN surface where they were visible as surface pits. The TDD of the GaN wing region was much lower than that of the seed region. Fig. 7-4 (a) shows a plan-view SEM image of a wing with seed regions. Fig. 7-4 (b) and (c) are the monochromatic CL images of Fig. 7-4 (a) at 373 nm and 443 nm, respectively. The bright regions showed that the emission of 373 nm mainly came from the low-defect density wings. In comparison, the emission of 443

nm came from the high-defect density GaN seeds. Similar behavior was observed in the lateral epitaxially overgrown window and wing region by Chakraborty *et al* [11]. They assumed that the presence of defects led to the increased indium incorporation in the poor quality region. We thus suggested that more indium atoms could incorporate in the MQWs of seed regions with higher dislocation density, resulting in longer emission wavelength from those areas.

7-4 Performance of nonpolar TELOG LEDs

Fig. 7-5 (a) shows the L-I-V characteristic of nonpolar TELOG LEDs. The I-V curve of the diode exhibited that the series resistance was about 50Ω and the forward voltage was below 2 volts. This indicated there could be some leakage current pathways. According to the Kozodoy's report [12], we suggest leakage current pathways could be due to lots of TDs in the seed regions. Besides, the output power increased appreciably when the injection current was increased over 40 mA and finally reached 0.2 mW at 140 mA. Fig. 7-5 (b) is the normalized EL spectra at drive currents ranging from 25 mA to 60 mA. When the injection current was below 25mA, the spectrum was dominated by the blue emission of 443 nm wavelength. Once the current was increased over 30 mA, UV emission of 373 nm appeared in addition to the 443nm emission. The intensity of the 373 nm UV peak increased much faster than that of 443 nm from 30 mA to 60 mA, and finally the UV peak became the dominant peak. Meanwhile, the 373 nm peak exhibited red-shift to 382 nm when the current was increased from 30 mA to 60 mA. This could be attributed to bandgap shrinkagedue to the thermal effect. We assume that the 373 nm ultraviolet emission comes from the GaN wing regions as shown in Fig. 7-4 (b). On the

other hand, the longer 443 nm wavelength EL emission (bright bands in Fig. 3(c)) comes from the TELOG seed regions. There are two reasons which could account for the special double peaks feature in EL spectra. First, since many TDs in the seed regions would form leakage current pathways, injection current tend to bypass wing regions and flow through these leakage channels in the seed regions at early stage (when the injection current was below 30 mA). The other reason is that the difference of band gap between seed and wing regions due to different Indium incorporation caused different turn-on voltages. Obviously, the turn-on voltage in wing regions was higher than that in seed regions. Therefore, the injection current preferred to pass through seed regions until the injection current is high enough to spread into wing regions. As a result, the emission peak of 443 nm was the dominate peak at early stage and subsequently the 373nm peak quickly increased in intensity once the injection current spread into the wing regions.

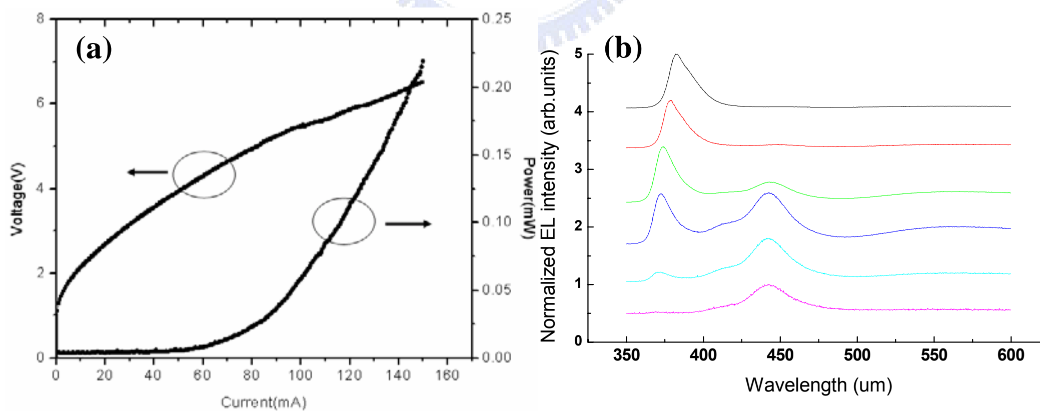

Fig. 7-5 (a) L-I-V characteristics of the ultraviolet nonpolar LED, (b) Normalized CW electroluminescence spectra.

Nonpolar GaN films have been shown to exhibit optically polarized spontaneous emission, which is explained by the crystal field oriented along the c-axis of wurtzite GaN and its effect on the valence band splitting induced

by large compressive strain within the wells [13]. Since that the a-plane (In,Ga)N films suffer from the anisotropic in-plane compressive strain in the x–y plane (x is oriented along <1$\underline{1}$00>, y is oriented along <11$\underline{2}$0>,and z is oriented along <0001>) of the wurtzite crystal and renders the original $|X \pm iY\rangle$ -like valence-band states of unstrained wurtzite GaN into $|X\rangle$ -like and $|Y\rangle$ -like states. The $|X\rangle$ -like state is raised in energy by the strain, while the $|Y\rangle$ -like state is pushed down below the $|Z\rangle$ -like state. The interband transition lowest in energy is thus that involving the $|X\rangle$ -like valence band which, according to its symmetry, is expected to be predominantly x-polarized ($E \perp c$). The transition involving the $|Z\rangle$ -like valence bands occurs at higher energy and is expected to be z-polarized ($E \parallel c$). Therefore, electronic transitions occur predominantly from the bottom of the conduction band to the topmost $|X\rangle$ -like state and the resulting light emission will have a strong x-polarized character. In order to analyze the linear polarization of the EL of our devices, we rotated a polarizer between a polarization angle of 0° (referred to as parallel to the c-axis) and 360°. The linear polarization of the EL of our devices at room temperature was analyzed by rotating a polarizer between a polarization angle of 0° (referred to as parallel to the c-axis) and 360°. The polarization ratio is defined as $\boldsymbol{\rho} = (I_{max} - I_{min})/(I_{max} + I_{min})$, where Imax is the intensity of light with polarization perpendicular to the *c* axis and Imin is the intensity of light with polarization parallel to the *c* axis. Fig. 7-6 shows the EL intensity of UV spectral range at different polarization angles at room temperature as the operation current is 80 mA. The degree of polarization is estimated to be about 28.7 %. This polarization ratio is lower than that reported at 10 K for the m-plane InGaN/GaN quantum wells grown by molecular beam epitaxy [14]. This could be explained by an increase in device temperature with

current injection and the higher-energy valence band minimum with polarization parallel to the c axis filled with holes, or by populating up the higher-energy valence band minimum as hole density increases with forward bias [15].

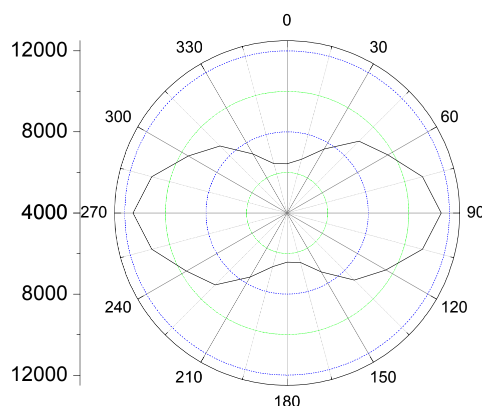

Fig. 7-6 Polarization degree of UV spectral range at the operation current of 80 mA.

7-5 Performance of nonpolar blue LEDs using superlattices

Room-temperature EL spectra under 20 mA injection current is shown in Fig. 7-7 (a). The same emission peaks located at 449nm for both samples. The EL FWHM of Sample.2 was measured as 28.7 nm, which was narrower than that of Sample.1 (FWHM =35.8 nm). The L-I-V curves were measured to further demonstrate the performance enhancement of a-plane LEDs using InGaN/GaN SLs as shown in Fig. 7-7 (b). These two I-V curves exhibited similar shapes, indicating that absence of degradation of electrical characteristics with the insertion of SLs. The forward voltages of Sample.1 and Sample.2 were both 4.25 volts at 20 mA operating current. The series resistances of Sample.1 and Sample.2 were estimated to be ~34 Ω. The output power of Sample.2 had a 3.42 times and 2.86 times increase compared to that of Sample.1 at 20mA and 100 mA injection current, respectively. Such apparent enhancement was attributed to the dislocation reduction and the

improvement of MQWs quality after using InGaN/GaN SLs.

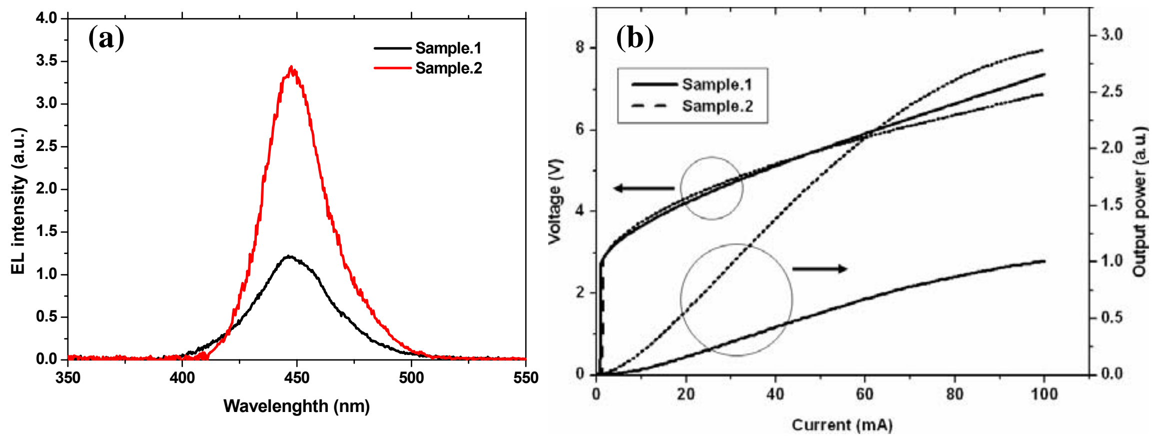

Fig. 7-7 (a) Room-temperature EL spectra and (b) L-I-V curves for Sample.1 and Sample.2.

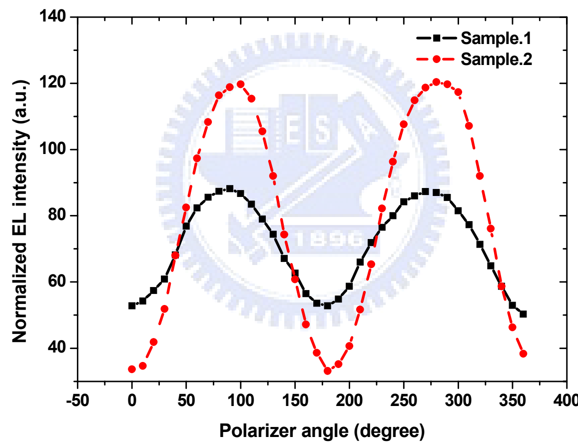

Fig. 7-8 EL intensity of Sample.1 and Sample.2 at different polarization angles at 20 mA injection current.

Fig. 7-8 shows the EL intensity of Sample.1 and Sample.2 at different polarization angles at room temperature. The degree of polarization of Sample.2, which was estimated to be approximately 56.3 %, was larger than that of Sample.1 (nearly 27.4%). There are two possible reasons that account for this phenomenon. First, the TDs in GaN act as nonradiative recombination centers and could restrict the carrier transitions from the bottom of the

conduction band to the topmost $|X\rangle$-like state. Since the SLs can reduce the dislocation density, the severely interruption for selective carrier transition was eliminated. The other reason is that the SLs may amplify the anisotropic in-plane compressive strain experienced by the MQWs and consequently arise higher transition energy difference between the $|X\rangle$-like state and $|Z\rangle$-like state. As a result, the polarized character of a-plane LEDs with SLs was enhanced.

7-6 Summary

In conclusion, we have grown nonpolar InGaN/GaN UV LEDs using the TELOG technique. Our CL results revealed that the low-defect density wings emitted 373 nm peak and the TELOG coalesced seed regions emitted 443 nm due to different incorporation of indium, which was apparently related with the distribution of TDs. The L-I-V diagram revealed that the series resistance was about 50Ω and there are leakage current pathways due to lots of TDs in seed regions. EL spectra showed that the peak of 443 nm appeared at first and then the peak of 373 nm was emitted with increasing current. We proposed that the reasons for this phenomenon were the different crystal quality and bandgap between the seed regions and the wing regions. The polarization measurements shown such LEDs possess 28.7% polarization degree.

On the other hand, we have also demonstrated that the performance enhancement on a-plane LEDs was achieved by the insertion of InGaN/GaN SLs. The EL intensity of the sample with InGaN/GaN SLs exhibited improvement by a factor of 3 times in comparison to that of the conventional sample without InGaN/GaN SLs, which could be attribute to the TD reduction and the improvement of LED quality. Furthermore, we observed that the

polarization degree of a-plane light emitting diodes with SLs (56.3%) was much higher than that of a-plane light emitting diodes without SLs (27.4%).

Reference

[1] M. D. Craven, S. H. Lim, F. Wu, J. S. Speck, and S. P. DenBaars, Appl.Phys. Lett. 81, 469 (2002).

[2] M. D. Craven, S. H. Lim, F. Wu, J. S. Speck, and S. P. DenBaars, Appl.Phys. Lett. 81, 1201 (2002).

[3] C. Chen, J. Zhang, J. Yang, V. Adivarahan, S. Rai, S. Wu, H. Wang, W. Sun, M. Su, Z. Gong, E. Kuokstis, M. Gaevski, and M. A. Khan, Jpn. J. Appl. Phys., Part 2 42, L818 (2003).

[4] B. Imer, F. Wu, S. P. DenBaars, and J. S. Speck, Appl. Phys. Lett. 88, 061908 (2006).

[5] T. C. Wang, T. C. Lu, T. S. Ko, H. C. Kuo, M. Yu, and S. C. Wang, Appl. Phys. Lett. 89, 251109 (2006).

[6] B. A. Haskell, F. Wu, M. D. Craven, S. Matsuda, P. T. Fini, T. Fujii, K. Fujito, S. P. DenBaars, J. S. Speck, and S. Nakamura, Appl. Phys. Lett. 83, 644 (2003).

[7] T.C Wang, T.C Lu, T.S Ko, H.C Kuo, M Yu, and S.C Wang, Appl. Phys. Lett. 89, 251109 (2006).

[8] B. A. Haskell, F. Wu, M. D. Craven, S. Matsuda, P. T. Fini, T. Fujii, K. Fujito, S. P. DenBaars, J. S. Speck, and Shuji Nakamura, Appl. Phys. Lett Vol. 83, 28 (2003).

[9] A. Chakraborty, K. C. Kim, F. Wu, J. S. Speck, S. P. DenBaars, and U. K. Mishra, Appl. Phys. Lett 83, 041903 (2006).

[10] J.W. Matthews and A.E. Blakeslee, J. Cryst. Growth 27, 118 (1976); 32, 265 (1976).

[11] A. Chakraborty, Stacia Keller, Cedrik Meier, Shuji Nakamura, James S. Speck, and Umesh K. Mishraa, Appl. Phys. Lett. 86, 031901 (2005).

[12] P. Kozodoy, J. P. Ibbetson, H. Marchand, P. T. Fini, S. Keller, J. S. Speck,S. P. DenBaars, and U. K. Mishra, Appl. Phys. Lett. 73, 975 (1998).

[13] B. Rau, P. Waltereit, O. Brandt, M. Ramsteiner, K. H. Ploog, J. Puls, and F. Henneberger, Appl. Phys. Lett. 77, 3343 (2000).

[14] Y. J. Sun, O. Brandt, M. Ramsteiner, H. T. Grahn, and K. H. Ploog, Appl. Phys. Lett. 82, 3850 (2003).

[15] N. F. Gardner, J. C. Kim, J. J. Wierer, Y. C. Shen, and M. R. Krames, Appl. Phys. Lett. 86, 111101 (2005).

Chapter 8 Conclusion and future work

In conclusion, the epitaxial growth of nonpolar a-plane GaN based optoelectronic materials grown using MOCVD have been investigated, which include optimum growth and growth mechanism. High quality and smooth surface *a*-plane GaN could be obtained at the high temperature and low pressure growth condition. Moreover, the thickness of the nucleation layer and V/III ratio for the GaN bulk growth existed optimal values for obtaining high quality *a*-plane GaN. We also tried to figure out the mechanism of nonpolar GaN by using Wulff plot and selective area growth to analyze the growth behavior of a-plane GaN grown on r-plane sapphire, we believe that a precise knowledge and a detailed understanding of kinetic Wulff plots will enable model-based growth of device-quality GaN in a predictive way.

In this chapter, we proposed several approaches to improve crystal quality and surface morphology of nonpolar a-plane GaN grown on r-plane sapphire, including TELOG and using InGaN/ GaN SLs. In first part, we have grown high quality and fully coalesced a-plane GaN films at the thickness of 10 μm by using TELOG with a 2-μm-seed / 18-μm-trench stripe pattern. The TDD can be reduced largely from 1×10^{10} cm^{-2} to 3×10^{7} cm^{-2} for the N-face GaN wing. In second part, we have demonstrated that the performance enhancement on a-plane LEDs was achieved by the insertion of InGaN/GaN SLs. The TD density was reduced from 3×10^{10} cm^{-2} down to $\sim9\times10^{9}$ cm^{-2}.

For active layer structural design, *a*-plane InGaN/GaN MQWs of different width ranging from 3 nm to 12 nm grown on r-plane sapphire by metal organic chemical vapor deposition were investigated. More effective capturing of excitons due to larger localization energy E_{loc} and shorter radiative lifetime of

localized excitons are observed in thinner well width samples in the temperature dependent TRPL. These phenomena are due to the better confinement of uniform and deep localized centers for excitons existing in the samples with thinner well widths, whereas more pronounced indium fluctuations or rougher interfaces in the MQWs exist in the samples with thicker well widths.

In development of nonpolar LEDs, we successfully fabricated nonpolar LEDs structure by using TELOG GaN substrate and inserting InGaN/GaN SLs layer. The growth conditions and structural design are based on previous discussion mentioned in Chapter 3~6. For TELOG sample, the L-I-V diagram revealed that the series resistance was about 50Ω and there are leakage current pathways due to lots of TDs in seed regions. EL spectra showed that the peak of 443 nm appeared at first and then the peak of 373 nm was emitted with increasing current. We also demonstrated the EL intensity of the sample with InGaN/GaN SLs was enhanced by a factor of 3.42 times to that of the conventional sample without InGaN/GaN SLs.

In this dissertation, we have achieved the studies on the growth of nonpolar GaN and the fabrication of devices. We expect this series of experiments to provide a useful information and contribution for development of nonpolar optoelectronic devices in future.

Future work

Recently, most of groups in worldwide start to engage in nonpolar nitrides growth on free standing GaN substrates which could avoid to the presence of plenty defects including TDs and SFs. Therefore, in addition initial methods we proposed to improve crystal quality of a-plane GaN, using GaN template as

substrate for growth of nonpolar GaN is essential in near future. The effects of high quality nonpolar GaN on either optical or electronic properties will be much different from the nonpolar GaN directly grown on r-plane sapphire or r-$LiAlO_2$.

In addition, the internal quantum efficiency should be almost the same when the wavelength is adjusted from UV to green due to no electric field exists in nonpolar nitride structure, whereas the efficiency of conventional c-plane LEDs often drops apparently when much indium is incorporated for green emission application. Therefore, the development of nonpolar green LEDs is a attractive and worthwhile to be tried. On the other hand, the fabrication of non-polar UVLED is bound to be an important topic. The realization of optoelectronic devices in UV region gains more and more interest in different kinds of fields, in particular, in the field of environment protection and medical devices. Moreover, UVLED can also be utilized to fabricate white LEDs by pumping high efficient phosphors. Therefore, it would have more challenges and difficulties to fabricate non-polar UVLEDs because the more complicated growth mechanisms and the more threading dislocations exist in growth of non-polar materials, which would be worthy of a lot of investigation. For sure, the use of nonpolar free-standing GaN substrates will be applied to above several developments.

柯宗憲 (Tsung-Shine Ko, T. S. Ko)

Publication List

A. Journal paper

1. ***Tsung-Shine Ko***, Li-Fu Zhuo, Wei-Lin Wang, Mei-Hui Liang, Tien-Chang Lu, Li Chang, Hao-Chung Kuo, Shing-Chung Wang, "Random lasing behavior in a-plane ZnMgO/ZnO multiple quantum wells", **Applied Physics Letters**, to be submitted (2009). **IF=4.308**
2. ***T. S. Ko***, L. F. Zhuo, W. L. Wang, M. H. Liang, T. C. Lu, Li Chang, H. C. Kuo, S. C. Wang, "Optical characteristics of a-plane $Zn_{0.8}Mg_{0.2}O$/ZnO multiple quantum wells grown by pulsed laser deposition", **Journal of Crystal Growth**, to be submitted (2009). **IF= 1.950**
3. ***T. S. Ko***, J. R. Chen, H. M. Huang, C. M. Chang, T. C. Lu, H. C. Kuo, S. C. Wang, "Quality improvement and optical enhancement of a-plane GaN using thermal annealing process", **Journal of Applied Physics**, submitted (2009).
4. ***T. S. Ko***, T. C. Lu, T. C. Wang, J. R. Chen, R. C. Gao, M. H. Lo, H. C. Kuo, S. C. Wang and J. L. Shen, "Optical study of a-plane InGaN/GaN multiple quantum wells with different well widths grown by metal-organic chemical vapor deposition", **Journal of Applied Physics**, 104, 093106-093113 (2008) and was selected in **Virtual Journal of Ultrafast Science**, Volume 7, Issue 12 (2008). **IF= 2.171**
5. ***T. S. Ko***, T. C. Wang, H. M. Huang, J. R. Chen, H. G. Chen, C. P. Chu, T. C. Lu, H. C. Kuo, and S. C. Wang, "Characteristics of a-plane GaN with SiN_x insertion layer grown by metal-organic chemical vapor deposition", **Journal of Crystal Growth**, 310, 4972-4975 (2008), **IF= 1.950**
6. ***Tsung-Shine Ko***, Tien-Chang Lu, Chia-Pu Chu, Hao-Chung Kuo, and Shing-Chung Wang, "Thermally evaporated In_2O_3 nanoloquats with tunable broad-band emissions", **Journal of Nanoscience and Nanotechnology**, 8, 4395-4398, (2008). **IF=2.194**
7. ***Tsung-Shine Ko***, Chia-Pu Chu, Jun-Rong Chen, Tien-Chang Lu, Hao-Chung Kuo, and Shing-Chung Wang, "Tunable light emissions from thermally evaporated In_2O_3 nanostructures grown at different growth temperatures", **Journal of Crystal Growth**, 310, 2264-2267 (2008). **IF= 1.950**
8. ***T. S. Ko***, J. Shieh, M. C. Yang, T. C. Lu, H. C. Kuo, S. C. Wang, "Phase transformation and optical characteristics of porous germanium thin film", **Thin Solid Film**, 516, 2934-2938 (2008). **IF=1.693**

9. ***T. S. Ko***, C. P. Chu, J. R. Chen, Y. A. Chang, T. C. Lu, H. C. Kuo, S. C. Wang, "Synthesis of In_2O_3 nanocrystal chains and annealing effect on their optical properties", **Journal of Vacuum Science & Technology A**, 25(4), 1038-1041, (2007) and was selected in **Virtual Journal of Nanoscale Science & Technology**, Volume 16, Issue 3, (2007). **IF=1.557**
10. ***T. S. Ko***, T. C. Wang, H. G. Chen, R. C. Gao, G. S. Huang, T. C. Lu, H. C. Kuo, S. C. Wang, "Observations on surface morphologies and dislocations of a-plane GaN grown by metal organic chemical vapor deposition", **physica status solidi (c)**, V4, No. 7, 2510-2514, (2007). **IF=1.221**
11. ***T. S. Ko***, T. C. Lu, T. C. Wang, M. H. Lo, J. R. Chen, R. C. Gao, H. C. Kuo, S. C. Wang and S. L. Shen, "Optical characteristics of a-plane InGaN/GaN multiple quantum wells with different well widths", **Applied Physics Letters**, 90, 181122-181124 (2007) and was selected in **Virtual Journal of Ultrafast Science**, Volume 6, Issue 6 (2007). **IF=4.308**
12. ***T. S. Ko***, T. C. Wang, R. C. Gao, H. G. Chen, G. S. Huang, T. C. Lu, H. C. Kuo, S. C. Wang, "Study on optimal growth condition of a-plane GaN grown on r-plane sapphire by metal-organic chemical vapor deposition", **Journal of Crystal Growth**, 300, 308-313 (2007). **IF= 1.950**
13. ***T. S. Ko***, T. C. Wang, H. G.. Chen, R. C. Gao, Y. J. Lee, T. C. Lu, H. C. Kuo, S. C. Wang, "InGaN/GaN nanostripe grown on pattern sapphire by metal organic chemical vapor deposition", **Applied Physics Letters**, 90, 013110-013112 (2007). **IF=4.308**
14. ***T. S. Ko***, S. Yang, H. C. Hsu, C. P. Chu, H. F. Lin, S. C. Liao, T. C. Lu, H. C. Kuo, W. F. Hsieh, S. C. Wang, "ZnO nanopowders fabricated by dc thermal plasma synthesis", **Materials Science and Engineering B**, 134, 54-58 (2006). **IF=1.331**
15. ***T. S. Ko***, C. P. Chu, H. G. Chen, T. C. Lu, H. C. Kuo, S. C. Wang, "Observation of Strong Red Photoluminescence with Broad Band in Indium Oxy-nitride Nanoparticles", **Journal of Vacuum Science & Technology A**, 24 (4), 1332-1335 (2006) and was selected in **Virtual Journal of Nanoscale Science & Technology**, Volume 14, Issue 1 (2006). **IF=1.557**
16. Qian Sun, ***Tsung-Shine Ko***, Christopher D. Yerino, In-Hwan Lee, Jung Han, Tien-Chang Lu, Hao-Chung Kuo and Shing-Chung Wang, "Effect of controlled growth dynamics on the microstructure of a-plane GaN revealed by x-ray diffraction", **Japanese Journal of Applied Physics**, submitted, (2009).
17. Shih-Chun Ling, Chu-Li Chao, Jun-Rong Chen, ***Tsung-Shine Ko***, Tien-Chang Lu, Hao-Chung Kuo, Shing-Chung Wang, Shun-Jen Cheng,

Po-Chun Liu, and Jenq-Dar Tsay," Nano-rod epitaxial lateral overgrowth of a-plane GaN with low dislocation density", **Applied physics Letters**, accepted. **IF=4.308**

18. Shih-Chun Ling, Te-Chung Wang, Jun-Rong Chen, Po-Chun Liu, ***Tsung-Shine Ko***, Bao-Yao Chang, Tien-Chang Lu, Hao-Chung Kuo, Shing-Chung Wang, and Jenq-Dar Tsay, "Characteristics of a-plane green light emitting diode grown on r-plane sapphire", **Photonics Technology Letters**, accepted. **IF=2.353**
19. J.-R. Chen, ***T.-S. Ko***, P.-Y. Su, T.-C. Lu, Y.-K. Kuo, H.-C. Kuo, and S.-C. Wang, "Numerical study on optimization of active layer structures for GaN/AlGaN multiple-quantum-well laser diodes", **IEEE Journal of Lightwave Technology**, (2009), accepted. **IF= 2.824**
20. Jun-Rong Chen, ***Tsung-Shine Ko***, Tien-Chang Lu, Yi-An Chang, Hao-Chung Kuo, Yen-Kuang Kuo, Jui-Yen Tsai, Li-Wen Laih, and Shing-Chung Wang, "Fabrication and characterization of temperature insensitive 660-nm resonant-cavity LEDs", **IEEE Journal of Lightwave Technology**, (2009), accepted. **IF=2.824**
21. Qian Sun, Yong Suk Cho, Bo Hyun Kong, Hyung Koun Cho, ***Tsung Shine Ko***, Christopher D. Yerino, In-Hwan Lee, Jung Han, "N-face GaN growth on c-plane sapphire by metalorganic chemical vapor deposition", **Journal of Crystal Growth**, 311, 2948-2952 (2009). **IF= 1.950**
22. Shih-Chun Ling, Tien-Chang Lu, Te-Chung Wang, Jun-Rong Chen, ***Tsung-Shine Ko***, Hao-Chung Kuo, Shing-Chung Wang, Po-Chun Liu, Jenq-Dar Tsay, "Dislocation reduction in a-plane light emitting diodes using InGaN/GaN superlattices", **Japanese Journal of Applied Physics**, 48, 04C136-04C139 (2009). **IF=1.222**
23. J. –R. Chen, S. –C. Ling, H. –M, Hung, P. –Y. Su, ***T. –S. Ko***, T. –C. Lu, H. –C, Kuo, Y. –K. Kuo, S. –C. Wang, "Numerical study of optical properties of InGaN multi-quantum-well laser diodes with polarization-matched AlInGaN barier layers", **Applied Physics B**, 95, 145-153 (2009). **IF=2.280**
24. Jun-Rong Chen, Shih-Chun Ling, Chin-Tsang Hung, ***Tsung-Shine Ko***, Tien-Chang Lu, Hao-Chung Kuo, and Shing-Chung Wang, "High-reflectivity ultraviolet AlN/AlGaN distributed Bragg reflectors grown by metalorganic chemical vapor deposition", **Journal of Crystal Growth**, 310, 4871-4875 (2008). **IF= 1.950**
25. Qian Sun, Christopher D. Yerino, ***Tsung Shine Ko***, Yong Suk Cho, In-Hwan Lee, Jung Han and Michael E. Coltrin, "Understanding non-polar

GaN growth through kinetic Wulff plots", **Journal of Applied Physics**, 104, 093523-093527 (2008). **IF= 2.171**

26. Y. S. Cho, Q. Sun, I.-H. Lee, ***T. -S. Ko***, C. D. Yerino, J. Han, B. H. Kong, H. K. Cho, and S. Wang, "Reduction of stacking fault density in m-plane GaN grown on SiC", **Applied Physics Letters**, 93, 111904-111906 (2008). **IF=4.308**
27. Te-Chung Wang, ***Tsung-Shine Ko***, Tien-Chang Lu, Hao-Chung Kuo, Run-Ci Gao, Jenq-Dar Tsay, and Sing-Chung Wang, "Internal quantum efficiency behavior of a-plane and c-plane InGaN / GaN multiple quantum well with different indium compositions", **physica status solidi (c)**, 5, 2161-2163, (2008). **IF=1.221**
28. S. -L. Wang, B. -C. Yeh, H. -M. Wu, L. -H. Peng, C. -M. Lai, ***T. -S. Ko***, T. -C. Lu, S. -C. Wang, A. -H. Kung, "Optical properties of a-plane GaN strained by photo- chemically grown gallium hydroxide", **physica status solidi (c)**, 5, 1780-1782, (2008). **IF=1.221**
29. Shih-Chun Ling, Te-Chung Wang, ***Tsung-Shine Ko***, Tien-Chang Lu, Hao-Chung Kuo and Shing-Chung Wang, "Characteristics of ultraviolet nonpolar InGaN/GaN light-emitting diodes using trench epitaxial lateral overgrowth technology", **Journal of Crystal Growth**, 310, 2330-2333 (2008). **IF= 1.950**
30. Hou-Guang Chen, ***Tsung-Shine Ko***; Li Chang; Yue-Han Wu; Tien-Chang Lu; Hao-Chung Kuo; Shing-Chung Wang, "Investigation on microstructure in GaN epitaxial growth on the stripe patterned r-plane sapphire substrates", **Journal of Crystal Growth**, 310, 1627-1631 (2008). **IF= 1.950**
31. Jun-Rong Chen, Chung-Hsien Lee, ***Tsung-Shine Ko***, Yi-An Chang, Tien-Chang Lu, Hao-Chung Kuo, Yen-Kuang Kuo, and Shing-Chung Wang, "Effects of built-in polarization and carrier overflow on InGaN quantum-well lasers with electronic blocking layers", **IEEE Journal of Lightwave Technology**, 26, 329-337 (2008). **IF=2.824**
32. Chia-Pu Chu, ***Tsung-Shine Ko***, Yu-Cheng Chang, Tien-Chang Lu, Hao-Chung Kuo, and Shing-Chung Wang, "Thermally evaporated In_2O_3 nanoloquats with oxygen flow dependent optical emissions", **Materials Science and Engineering B**, 147, 276-279 (2008). **IF=1.331**
33. Hou-Guang Chen, ***Tsung-Shine Ko***, Shih-Chun Ling, Tien-Chang Lu, Hao-Chung Kuo, Shing-Chung Wang, Yue-Han Wu, Li Chang, "Dislocation reduction in GaN grown on stripe patterned r-plane sapphire substrates", **Applied Physics Letters**, 91, 021914-021916 (2007). **IF=4.308**
34. Te-Chung Wang, Tien-Chang Lu, ***Tsung-Shine Ko***, Hao-Chung Kuo,

Hou-Guang Chen, Min Yu, Chang-Cheng Chuo, Zheng-Hong Lee, and Sing-Chung Wang, “Material and optical properties of Trenched Epitaxial Lateral Overgrowth of a-plane GaN”, **physica status solidi (c)**, V4, No. 7, 2519-2513 (2007). **IF=1.221**

35. Te-Chung Wang, Tien-Chang Lu, ***Tsung-Shine Ko***, Hao-Chung Kuo, Hou-Guang Chen, Min Yu, Chang-Cheng Chuo, Zheng-Hong Lee, Sing-Chung Wang, “Trenched Epitaxial Lateral Overgrowth of Fast Coalesced a-plane GaN with Low Dislocation Density”, **Applied Physics Letters**, 89, 251109-251111 (2006). **IF=4.308**
36. Yi-An Chang, ***Tsung-Shine Ko***, Jun-Rong Chen, Fang-I Lai, Chun-Lung Yu, I-TsungWu, Hao-Chung Kuo, Yen-Kuang Kuo, Li-Wen Laih, Li-Horng Laih, Tin-Chang Lu, Shing-Chung Wang, “The carrier blocking effect on 850 nm InAlGaAs/AlGaAs vertical-cavity surface-emitting lasers”, **Semiconductor Science and Technology**, 21(10), 1488-1494 (2006). **IF=2.152**
37. H. L. Chen, H. C. Cheng, ***T. S. Ko***, S. Y. Chuang, and T. C. Chu, “Characterizing Optical Properties of Self-assembled Gold Nanoparticles for Surface Plasmon Resonance Device Applications”, **Japanese Journal of Applied Physics**, 45(9A), 6984-6986 (2006). **IF=1.222**
38. C. H. Lin, C. F. Lai, ***T. S. Ko***, H. W. Huang, H. C. Kuo, Y. Y. Hung, K. M. Leung, C. C. Yu, R. J. Tsai, C. K. Lee, T. C. Lu, S. C. Wang, “Enhancement of InGaN–GaN Indium–Tin–Oxide Flip-Chip Light-Emitting Diodes With TiO_2–SiO_2 Multilayer Stack Omnidirectional Reflector”, **IEEE Photonics Technology Letters**, 18(19), 2050-2052 (2006). **IF=2.353**
39. Ming Che Yang, Jiann Shieh, ***Tsung Shine Ko***, Hsuen Li Chen and Tieh Chi Chu, “Fabrication of Silicon and Germanium Nanostructures by Combination of Hydrogen Plasma Dry Etching and VLS Mechanism”, **Japanese Journal of Applied Physics**, 44(7B), 5791-5794 (2005). **IF=1.222**
40. Jiann Shieh, Hsuen Li Chen, ***Tsung Shine Ko***, Hsu Chun Cheng, and Tieh Chi Chu, “Nanoparticle-Assisted Growth of Porous Germanium Thin Film”, **Advanced Materials**, 16(13), 1121-1124 (2004). **IF=8.079**
41. H. L. Chen, H. C. Cheng, ***T. S. Ko***, F. H. Ko, T. C. Chu, “High reflectance of reflective-type attenuated-phase-shifting masks for extreme ultraviolet lithography with high inspection contrast in deep ultraviolet regimes”, **Journal of Vacuum Science Technology B**, 22(6), 3049-3052 (2004). **IF=1.664**
42. Jiann Shieh, ***Tsung Shine Ko***, Hsuen Li Chen, Jia Min Shieh, Bau Tong

Dai, and Tieh Chi Chu, "Low-temperature growth of germanium quantum dots on silicon oxide by inductively coupled plasma chemical vapor deposition", **Chemical Vapor Deposition**, 10(5), 265-269 (2004). **IF=2.209**

43. Hsu Chun Cheng, Hsuen Li Chen, ***Tsung Shine Ko***, Lee Jene Lai, Fu Hsiang Ko, and Tieh Chi Chu, "Enhance Extreme Ultraviolet Lithography Mask Inspection Contrast by using Fabry-Perot type Antireflective Coatings", **Japanese Journal of Applied Physics**, 43(6B), 3703-3706 (2004). **IF=1.222**

B. Domestic paper

1. 柯宗憲，王德忠，盧廷昌，郭浩中，「先進光電材料—非極性氮化鎵磊晶的發展」，光連雙月刊，Vol. 69，頁51-55，(2007)
2. 柯宗憲，王德忠，陳俊榮，郭浩中，盧廷昌，「三五族氮化物半導體有機金屬氣相沉積磊晶技術(MOCVD)之發展與未來」，電子月刊，Vol. 140，頁160-172，(2007)
3. 柯宗憲，楊閔智，謝健，盧廷昌，郭浩中，王興宗，「快速熱退火對多孔鍺薄膜結構與發光性質之影響」，奈米通訊，第十三卷第一期，頁24-28, (2006)
4. 謝健，楊閔智，柯宗憲，「結合氫氣乾式蝕刻及氣-固-液相成長機制製作矽的奈米線及鍺的奈米結構」，奈米通訊，第十一卷第三期，頁6-11，(2004)
5. 陳學禮，柯宗憲，鄭旭君，朱鐵吉，「利用Frabry-Perot型抗反射層結構提升極紫外光微影光罩圖形檢視對比度之技術」，奈米通訊，第十一卷第三期，頁1-5，(2004)
6. 謝健，柯宗憲，陳學禮，鄭旭君，謝嘉民，戴寶通，「以金奈米粒子輔助高密度感應耦合電漿化學氣相沉積高密度鍺量子點於氧化矽基板之研究」，奈米通訊，第十卷第三期，頁9-12, (2003)

C. International conference

1. Jun-Rong Chen, Yung-Chi Wu, ***Tsung-Shine Ko***, Tien-Chang Lu, Yen-Kuang Kuo, Hao-Chung Kuo, and Shing-Chung Wang, June 2008, "Theoretical analysis on lateral mode behavior of high-power 660-nm InGaP-AlGaInP laser diodes," 6th International Conference on Optics Design and Fabrication (ODF'08).
2. Jun-Rong Chen, Chia-Ming Chang, Wei-Rein Liu, Chien-Cheng Kuo, Tien-Chang Lu, ***Tsung-Shine Ko***, Wen-Feng Hsieh, Hao-Chung Kuo, Cheng-Chung Lee, and Shing-Chung Wang, July 2008, "Strong exciton-photon coupling at room temperature in ZnO-based hybrid microcavities," 14th Microoptics Conference (MOC'08), be held in Brussels, Belgium on September 25 - 27, 2008.

3. Jun-Rong Chen, Shih-Chun Ling, Huei-Min huang, ***Tsung-Shine Ko***, Tien-Chang Lu, Hao-Chung Kuo, and Shing-Chung Wang, July 2008, “Ultraviolet distributed Bragg reflectors based on AlGaN/AlN multilayers grown by metalorganic chemical vapor deposition,” 2008 International Conference on Solid State Devices and Materials (SSDM 2008), be held in Ibaraki, Japan on September 23-26, 2008.
4. ***T. S. Ko***, Y. T. Lee, J. R. Chen, S. C. Ling, T. C. Lu, H. C. Kuo, and S. C. Wang, “Effect of Si doping in different positions of a-plane InGaN/GaN multiple quantum wells”, The 2nd International Symposium on Growth of III-Nitrides, Laforet Shuzenji, Izu, Japan, July 6-9, 2008.
5. ***T. S. Ko***, T. C. Wang, J. R. Chen, C. P. Chu, T. C. Lu, H. C. Kuo, and S. C. Wang, “Characteristics of a-plane GaN with SiN_x insertion layer grown by metal-organic chemical vapor deposition”, 14th International Conference on Metal Organic Vapor Phase Epitaxy, Metz, France, June 1-6, 2008.
6. Jun-Rong Chen, Shih-Chun Ling, ***Tsung-Shine Ko***, Tien-Chang Lu, Hao-Chung Kuo, and Shing-Chung Wang, February 2008, “High-reflectivity ultraviolet AlN/AlGaN distributed Bragg reflectors grown by metalorganic chemical vapor deposition,” 14th International Conference on Metal Organic Vapor Phase Epitaxy (ICMOVPE-XIV).
7. Shih-Chun Ling, Te-Chung Wang, Jun-Rong Chen, ***Tsung-Shine Ko***, Tien-Chang Lu, Hao-Chung Kuo,Shing-Chung Wang and Jenq-Dar Tsay, “Dislocation reduction in a-plane light emitting diodes using InGaN/GaN superlattices”, 14th International Conference on Metal Organic Vapor Phase Epitaxy, Metz, France, June 1-6, 2008.
8. J. R. Chen, T. C. Lu, G. S. Huang, ***T. S. Ko*** H. C. Kuo, S. C. Wang, “Infrared reflectance of optical phonon modes in AlGaN epitaxial layers grown on sapphire substrates”, Conference on Gallium Nitride Materials and Devices III, PROCEEDINGS OF THE SOCIETY OF PHOTO-OPTICAL INSTRUMENTATION ENGINEERS (SPIE), Vol. 6894, U8941, be held in San Jose CA, Jan 21-24, 2008.
9. M. H. Lo, Z. Y. Li, Chen, J. R. Chen, ***T. S. Ko***, ; T. C. Lu, H. C. Kuo, S. C. Wang, “AlGaN/GaN multiple quantum wells grown by atomic layer deposition”, Conference on Gallium Nitride Materials and Devices III, PROCEEDINGS OF THE SOCIETY OF PHOTO-OPTICAL INSTRUMENTATION ENGINEERS (SPIE), Vol. 6894, U8941, be held in San Jose CA, Jan 21-24, 2008.
10. Te-Chung Wang, ***Tsung-Shine Ko***, Run-Ci Gao, Tien-Chang Lu, Hao-Chung Kuo, and Sing-Chung Wang, “The internal quantum efficiency

behavior of a-plane and c-plane InGaN/GaN MQWs with Different Indium Compositions", 7th Int'l Conference of Nitride Semiconductors (INCS), be held in Las Vegas, Nevada, September 16-21, 2007.

11. Shih-Chun Ling, Te-Chung Wang, ***Tsung-Shine Ko***, Tien-Chang Lu, Hao-Chung Kuo, and Shing-Chung Wang, " Characteristics of ultraviolet nonpolar InGaN/GaN light-emitting diodes using trench epitaxial lateral overgrowth technology", The 7th Pacific Rim Conference on Lasers and Electro-Optics (CLEO-PR 2007), be held August 26-31, Convention & Exhibition Center, Seoul, Korea, 2007.
12. T.-C. Lu, J.-R. Chen, G.-S. Huang, ***T.-S. Ko***, H.-C. Kuo, S.-C. Wang, "Infrared reflectance of optical phonon modes in AlGaN epitaxial layers grown on sapphire substrates", SPIE Photonics West, be held 19 - 24 January 2008, San Jose Convention Center, San Jose, California, USA.
13. ***T. S. Ko***, T. C. Wang, J. R. Chen, M. H. Lo, C. P. Chu, G. S. Huang, T. C. Lu, H. C. Kuo, S. C. Wang, "Defects reduction and luminescence improvement of a-plane GaN by inserting SiN_x nanomasks", The 15th International Conference on Crystal Growth, be held August 12 - 17, Salt Lake City, 2007.
14. M. H. Lo, G. S. Huang, ***T. S. Ko***, J. R. Chen, H. C. Kuo, T. C. Lu, S. C. Wang," Improvement of quality and efficiency of light emitting diodes by inserting low temperature AlN layers on silicon substrates", The 15th International Conference on Crystal Growth, be held August 12 - 17, Salt Lake City, 2007.
15. ***T. S. Ko***, T. C. Wang, J. R. Chen, M. H. Lo, C. P. Chu, G. S. Huang, T. C. Lu, H. C. Kuo, S. C. Wang, "The effects of H_2/NH_3 gas flow during growth process on the morphology and hole concentration of a-plane p-type GaN", The 4th International Conference on Materials for Advanced Technologies, be held at the Singapore International Convention & Exhibition Centre July 1 – 6, Singapore, 2007.
16. M. H. Lo, G. S. Huang, ***T. S. Ko***, J. R. Chen, H. C. Kuo, T. C. Lu, S. C. Wang, "Improvement in extraction efficiency of ultraviolet light emitting diodes with natural textured surface of p-GaN at various growth temperatures", The 4th International Conference on Materials for Advanced Technologies, be held at the Singapore International Convention & Exhibition Centre July 1 – 6, Singapore, 2007.
17. J. R. Chen, G. S. Huang, Ming Hua Lo, ***Tsung Shine Ko***, T. C. Lu, H. C. Kuo, S. C. Wang, "High-reflectivity ultraviolet AlN/AlGaN distributed Bragg reflectors grown by metalorganic chemical vapor deposition", The 4th

International Conference on Materials for Advanced Technologies, be held at the Singapore International Convention & Exhibition Centre July 1 – 6, Singapore, 2007.

18. ***Tsung-Shine Ko***, Chia-Pu Chu, Tien-Chang Lu, Hao-Chung Kuo, and Shing-Chung Wang, "Characteristics of indium oxide nano-loquats grown by thermal evaporation", E-MRS 2007 Spring Meeting, which will be held at the Congress Center in Strasbourg (France) from May 28 to June 1, 2007.
19. Hung-Lu Chang, ***Tsung-Shine Ko***, Tien-Chang Lu, Hao-Chung Kuo, and Shing-Chung Wang, "Effect of oxygen on characteristics of nickel oxide / indium tin oxide heterojunction diodes", E-MRS 2007 Spring Meeting, which will be held at the Congress Center in Strasbourg (France) from May 28 to June 1, 2007.
20. ***T. S. Ko***, C. P. Chu, H. G. Chen, H. C. Kuo, S. C. Wang, "Synthesis and Optical Properties of Indium Oxide Nanocrystal Chains Grown by Thermal Oxidation Method", AVS 53nd International Symposium, November 12-17, San Francisco, CA, USA, 2006
21. ***Tsung-Shine Ko***, Te-Chung Wang, Run-Ci Gao, Chia-Pu Chu, Tien-Chang Lu, Hao-Chung Kuo, Shing-Chung Wang, "Study on growth condition of (11-20) a-plane GaN on (1-102) r-plane sapphire by MOCVD", International Workshop on Nitride Semiconductors 2006, Oct 22-27, Kyoto, Japan, 2006
22. C. F. Lai, H. C. Kuo, ***T. S. Ko***, C. E. Lin, C. H. Lin, K. M. Leung, T. C. Lu, S. C. Wang, "High power and high reliability In GaN/GaN ITO flip chip light emitting diodes with TiO_2/SiO_2 multilayer stack omnidirectional reflector", International Workshop on Nitride Semiconductors 2006, Oct 22-27, Kyoto, Japan, 2006
23. Te-Chung Wang, ***Tsung-Shine Ko***, Hao-Chung Kuo, Tien-Chang Lu, Min Yu, Chang-Cheng Chuo, Zheng-Hong Lee, "Optical and structural properties of a-plane GaN with epitaxial lateral overgrowth", International Workshop on Nitride Semiconductors 2006, Oct 22-27, Kyoto, Japan, 2006
24. ***T.S. Ko***, C.F. Lay, Y.J. Lee, T.C. Lu, H.C. Kuo, and S.C. Wang, "Characteristics of InGaN multiple quantum wells grown on patterned sapphire substrates", Tu-P.11, 13th International Conference on Metal Organic Vapor Phase Epitaxy, Miyazaki, Japan, May 22-26, 2006
25. Yi-An Chang, Sheng-Horng Yen, ***Tsung-Shine Ko***, Te-Chung Wang, Chun-Yi Lu, Hao-Chung Kuo, Yen-Kuang Kuo, Tien-Chang Lu, Shing-Chung Wang, "Experimental and Theoretical Analysis on Ultraviolet 370-nm AlGaInN Light-Emitting Diodes", CLEO/QELS 2006, to be held

May 21-26, Long Beach, CA, USA, 2006

26. ***T.S. Ko***, C.P. Chu, W.T. Hsu, H.C. Kuo, S.C. Wang, “Observation of Broad Strong Red Photoluminescence Band in Indium Oxy-nitride Nanoparticles”, AVS 52nd International Symposium, to be held October 30 through November 4, Boston, MA, USA, 2005
27. Hsuen Li Chen, Hsu Chun Cheng, ***Tsung Shine Ko***, Fu Hsiang Ko, and Tieh Chi Chu, “High reflectance of reflective type attenuated-phase-shifting-masks for extreme ultraviolet lithography with high inspection-contrast in deep ultraviolet regimes”m, The 48th International Conference on Electron, Ion and Photon Beam Technology & Nanofabrication (EIPBN 2004), San Diego, CA, Jun.1-4, 2004
28. Hsuen Li Chen, ***Tsung Shine Ko***, Hsu Chun Cheng, Fu Hsiang Ko, and Tieh Chi Chu, “Characterizing Optical Properties of Self-assembled Gold Nanoparticles for Optimization of Surface Plasmon Resonance Device Applications”, The 48th International Conference on Electron, Ion and Photon Beam Technology & Nanofabrication (EIPBN 2004), San Diego, CA, Jun.1-4, 2004
29. Hsu Chun Cheng, Hsuen Li Chen, ***Tsung Shine Ko***, Lee Jene Lai, Fu Hsiang Ko, and Tieh Chi Chu, “Enhance Extreme Ultraviolet Lithography Mask Inspection Contrast by using Fabry-Perot type Antireflective Coatings”, International Microprocesses and Nanotechnology Conference 2003 (MNC), Tokyo, Japan, Oct.28-31, 2003

D. Domestic conference

1. L. F. Zhuo, ***T. S. Ko***, W. L. Wang, T. C. Lu, H. C. Kuo, S. C. Wang, L. Chang, “Optical Characteristic of A-plane $Zn_{0.8}Mg_{0.2}O$/ ZnO MQW Grown by Pulsed Laser Deposition”, Optics and Photonics Taiwan, Dec. 2008 **and also was rewarded “Student Thesis Award”**.
2. C. M. Chang, ***T. S. Ko***, T. C. Lu, H. C. Kuo, S. C. Wang, “Growth of Non-polar a-plane ZnO Nanostructures and Films Using a-plane GaN Buffer Layer”, Optics and Photonics Taiwan, Dec. 2007.
3. Y. T. Lee, ***T. S. Ko***, T. C. Wang, R. C. Gao, J. R. Chen, T. C. Lu, H. C. Kuo, S. C. Wang, “Carrier Behaviors and Optical Characteristics of a-plane InGaN/GaN Multiple Quantum Wells with Different Well Widths”, Optics and Photonics Taiwan, Dec. 2007, **and also was rewarded “Student Thesis Award”**.
4. 陳厚光, 張立, 柯宗憲, 盧廷昌, 郭浩中, 王興宗,"氮化鎵在圖案化r晶面氧化鋁基材磊晶成長之研究," 96年度中國材料年會, 新竹, Nov. 2007. **獲中國材**

料年會論文獎佳作。

5. ***T. S. Ko***, T. C. Wang, R. C. Gao, Y. J. Lee, T. C. Lu, H. C. Kuo, and S. C. Wang, "InGaN/GaN Nano-stripe Grown on Pattern Sapphire by Metal Organic Chemical Vapor Deposition", Optics and Photonics Taiwan, Dec. 2006, **and also was nominated "Student Thesis Award"**.
6. R.C. Gao, ***T. S. Ko***, T.C. Lu, T.C. Wang, M.H. Lo, J.R. Chen, H.C. Kuo, S.C. Wang, "The optical characteristics of different well width from nonpolar $In_xGa_{1-x}N$ multiple quantum wells", Optics and Photonics Taiwan, Dec. 2006.
7. C. P. Chu, ***T. S. Ko***, T. C. Lu, H. C. Kuo, S. C. Wang, " Synthesis of In_2O_3 nanocrystal chains and research on annealing effect on their optical properties", Optics and Photonics Taiwan, Dec. 2006.
8. C. P. Chu, ***T. S. Ko,*** W. T. Hsu, T. C. Lu, H. C. Kuo, S. C. Wang, "The Broad Strong Red Photoluminescence Emission of Indium Oxy-nitride Nanoparticles", reflector", Optics and Photonics Taiwan '05, paper PA-FRI-084, Dec. 2005.
9. Jiann Shieh, ***Tsung Shine Ko***, Hsuen Li Chen, Jia Min Shieh, Bau Tong Dai, and Tieh Chi Chu, "Low-temperature growth of germanium quantum dots on silicon oxide by replacing gold nanoparticles", The 11th Symposium on Nano Device Technology (SNDT 2004), Hsinchu, May 12-13, 2004.
10. 謝健，柯宗憲，陳學禮，鄭旭君，謝嘉民，戴寶通，朱鐵吉，「以金奈米粒子輔助成長鍺量子點與多孔鍺薄膜」，第三屆兩岸三地奈米研討會，2004年4月27日至5月1日，東華大學，花蓮。
11. Jiann Shieh, ***Tsung Shine Ko***, Hsuen Li Chen, Jia Min Shieh, Bau Tong Dai, and Tieh Chi Chu, "Low-temperature growth of germanium quantum dots on silicon oxide by inductively coupled plasma chemical vapor deposition", 2003材料年會，2003年11月21日至11月22日，崑山科技大學，台南。
12. Hsuen Li Chen, ***Tsung Shine Ko***, Lee Jene Lai, and Hsu Chun Cheng, "Enhanced Extreme Ultraviolet Lithography Mask Inspecton Contrast by Using Fabry-Perot Type Antireflective Coatings.", NSRRC Annual Users' Meeting and 10th Anniversary of Operation, Hsinchu, Taiwan, Oct. 30-31, 2003.
13. Hsu Chun Cheng, ***Tsung Shine Ko***, Hsuen Li Chen, Fu Hsiang Ko, and Tieh Chi Chu, "Study of Inspection Contrast between Absorber and Reflective Layers in Extreme Ultraviolet Masks", The 10th Symposium on Nano Device Technology (SNDT 2003), Hsinchu, May 14-15, 2003.

E. Patent

1. 柯宗憲，盧廷昌，郭浩中，王興宗，「利用圖案化藍寶石基板提升量子井結構之光萃取效率」，中華民國專利申請中，(2007)
2. 謝健，柯宗憲，陳學禮，謝嘉民，戴寶通，朱鐵吉，「以金奈米粒子輔助成長半導體量子點的製作方法」，中華民國專利證號 I233480，(2006)
3. 謝健，柯宗憲，陳學禮，謝嘉民，戴寶通，朱鐵吉，「奈米多孔性半導體薄膜的製作方法」，中華民國專利證號 I232892，(2006)